THE CHEMISTRY OF GIANT STARS IN THE SAGITTARIUS DWARF SPHEROIDAL

A thesis submitted to the University of Manchester
for the degree of Master of Science
in the Faculty of Engineering and Physical Sciences

October 2014

By
Skandar Taj
School of Physics and Astronomy

Contents

List of Tables

List of Figures

Declaration

No portion of the work referred to in this thesis has been submitted in support of an application for another degree or qualification of this or any other university or other institution of learning.

Copyright

Library, The University Librarys regulations (see http://www.manchester.ac.uk/library/aboutus/regulations) and in The University's policy on presentation of Theses.

Abstract

The detailed chemical abundances and atmospheric parameters of 27 K–type giant stars in the Sagittarius Dwarf Spheroidal galaxy (Sgr dSph) and a control sample of 27 K–type giant stars in the Galactic Bulge have been calculated. The the chemical composition of Sgr dSph stars are different from the Galactic Bulge stars. The Sgr dSph stars are metal poor, with a mean metallicity of [Fe/H] = –0.82 dex with a range of –1.31 to –0.35 dex and an [α/Fe] = 0.20 dex with range of –0.28 to 0.55 dex. For the Bulge a mean metallicity was found of [Fe/H] = –0.25 dex with a range of –1.15 to +0.53 dex and a mean [α/Fe] = 0.06 dex with range of –0.41 to 0.48 dex. Many elements (Si, Ca, Ti, Fe) in the Sgr dSph show an under-abundance when compared to the Bulge stars. The sample of stars studied in both galaxies does not include metal-rich populations which are seen in other studies because the selection criteria are biased towards metal-poor stars, which affects the mean metallicity and range found in this project.

For the Sgr dSph, the [α/Fe] ratio declines with [Fe/H] from 0.4 to –0.1 dex and the [α/Fe] knee is at approximately –0.8 dex. For the Bulge, the [α/Fe] ratio declines with [Fe/H] from 0.4 dex to –0.3 dex and the [α/Fe] knee is at approximately –0.6 dex. The difference in the metallicity of the [α/Fe] knees support the fact the enrichment occurred faster in the Bulge stars. Additionally, the low [α/Fe] ratios imply that type Ia supernovae contributed to the composition of the younger, metal rich Sgr dSph population. The extent to which the Sgr dSph has changed by the interaction with the Milky Way is currently difficult to assess. The lack of radial abundance variations in the Sgr dSph show that the population is homogeneous and

all the populations are seen at all radii. This is different to other dwarf galaxies and is likely a result of tidal stripping that is going on in the Sgr dSph.

Acknowledgements

Thanks to my supervisors Dr Iain McDonald and Professor Albert Zijlstra, for their guidance on this project and along Christian Johnson for his advice on various aspects of this project. Thanks to Ant and Bob for unending patience with computing-related queries. To the students of the East Wing, in particular Christina, Philippa Mike, Chris, Lucas, Jonathan, Nick, Stuart, Lee, Sarah and thanks for making JBCA such a vibrant and friendly place to work.

List of Abbreviations and Symbols

The following abbreviations and symbols are used throughout this thesis:

AGB – Asymptotic Giant Branch

BCD – Blue Compact Dwarfs

CMD – Colour Magnitude Diagram

dE – Dwarf Elliptical Galaxies

dSphs – Dwarf Spheroidal Galaxies

dI – Dwarf Irregular Galaxies

EW – Equivalent Width

FDU – First Dredge Up

FWHM – Full Width at Half Maximum

GB – Galactic Bulge

GC – Galactic Centre

HR – Hertzsprung Russell Diagram

HB – Horizontal Branch

IR – Infrared

ISM – Interstellar Medium

IMF – Initial Mass Function

$L_{\odot}$–Solar Luminosity

LMC - Large Magellanic Cloud

$M_{\odot}$ – Solar Mass

MC – Magellanic Cloud

MW – Milky Way

RGB – Red Giant Branch

SFR – Star formation Rate

SFH – Star formation History

Sgr dSph – Sagittarius Dwarf Spheroidal Galaxy

SN – Supernova

TP-AGB – Thermally Pulsating Asymptotic Giant Branch

Chapter 1

Introduction

1.1 Motivation

My motivation for carrying out this project is to develop our understanding of how chemical enrichment takes place in the Universe. This can be achieved by studying dwarf galaxies such as the Sagittarius Dwarf Spheroidal Galaxy (Sgr dSph). This galaxy is the closest metal-poor dwarf galaxy to the earth and hence this makes the Sgr dSph an excellent candidate for allowing comparisons to be made between populations of stars from different galaxies, such the Galactic Bulge (GB). The return of material to the interstellar medium (ISM) is a key process as new stars are born out of the dust and gas that exists between the stars. During the lifetime of stars, depending on their total mass, much of its mass may be returned to the ISM through stellar winds and explosive events such as supernova. Hence subsequent generations of stars can then form from this material.

Understanding the star-formation history of dwarf galaxies is important in understanding the composition of visible matter within the Universe today. I will review how this project will form part of a larger effort to help build a greater understanding of the chemical evolution of galaxies.

The chemical evolution in galaxies begins with a hydrogen and helium medium, which was formed in the Big Bang. The stars that are formed evolve and, over time, they return part of their mass back to the ISM. The ISM is then enriched with heavier elements (astronomical metals). By looking at the mass of stars in terms of their elemental, molecular and mineralogical return, as a function of their composition (metallicity) and mass (age), this can help to build a better understanding of the chemical enrichment of the Universe. The mass which is returned from stars to the ISM is a powerful driver of chemical change in a galaxy.

The wealth and amount of the material which is returned to the ISM will determine the chemical make up of the following generations of stars and planets. A large fraction of the metals returned to the ISM are ejected by highly evolved asymptotic giant branch (AGB) stars which lose mass via pulsation-enhanced, dust-driven winds (Gehrz 1989; Zhukovska, Gail & Trieloff 2008).

1.2 Stellar Evolution and Abundances

1.2.1 The first dredge up

For the majority of its life, a star spends its time on the main sequence (MS) during which it burns hydrogen into helium in its core via the proton–proton chain (pp chain) or the carbon-nitrogen cycle (CNO) which occurs only in stars of higher mass. Figure 1.1 shows a star's evolution from the main sequence to the AGB on the Hertzsprung-Russell diagram.

Once the hydrogen is exhausted in the core it contracts under gravity, the temperature rises and the hydrogen burning then moves towards a shell surrounding the helium core. After the exhaustion of core hydrogen, the star will be subjected to the first dredge up (FDU). In the FDU, material from the deep within the interior of the star is brought to the surface. Stars which have undergone first dredge up will then show an increase in ^{14}N, a decrease in ^{12}C and lower $^{12}C/^{13}C$ and

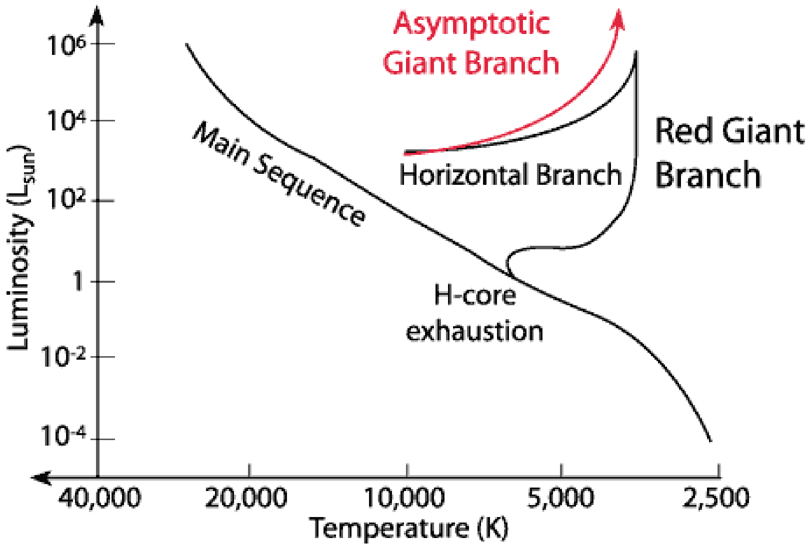

Figure 1.1: The location of the AGB on the Hertsprung-Russell diagram. Reproduced from http://www.noao.edu/outreach/press/pr03/sb0307.html.

$^{12}C/^{14}N$ ratios (Gratton, Sneden & Carretta 2004). Figure 1.2 shows the change in abundance with radius for ^{14}N and ^{12}C. Core contraction leads to an increase in temperature, which then causes the outer layers of the star to expand and its luminosity to increase. It begins to ascend the red giant branch (RGB). The hydrogen shell burning process produces further helium, which collects on the helium core. With the core continuing to contract, the temperature continues to increase, eventually reaching the point where helium burning can occur. In low mass stars (M $<$ 2-3 $M_\odot$), helium burning begins after a violent helium flash which eases the electron degeneracy of the core. During the helium burning stage, a star (Wood 2010) will lie on the horizontal branch (HB). Once all the helium is consumed within the core, helium burning then moves outwards to a helium-burning shell around the degenerate carbon-oxygen core, becoming as asymptotic giant branch (AGB) star (Blöcker, Driebe & Herwig 1999). AGB stars are characterised by an outer shell of burning hydrogen and an inner shell burning helium, both of which surround the dense, degenerate carbon and oxygen core. Figure 1.3 shows the degenerate C-O core surrounded by a He-burning shell above the core, and a H-burning shell below the deep convective envelope.

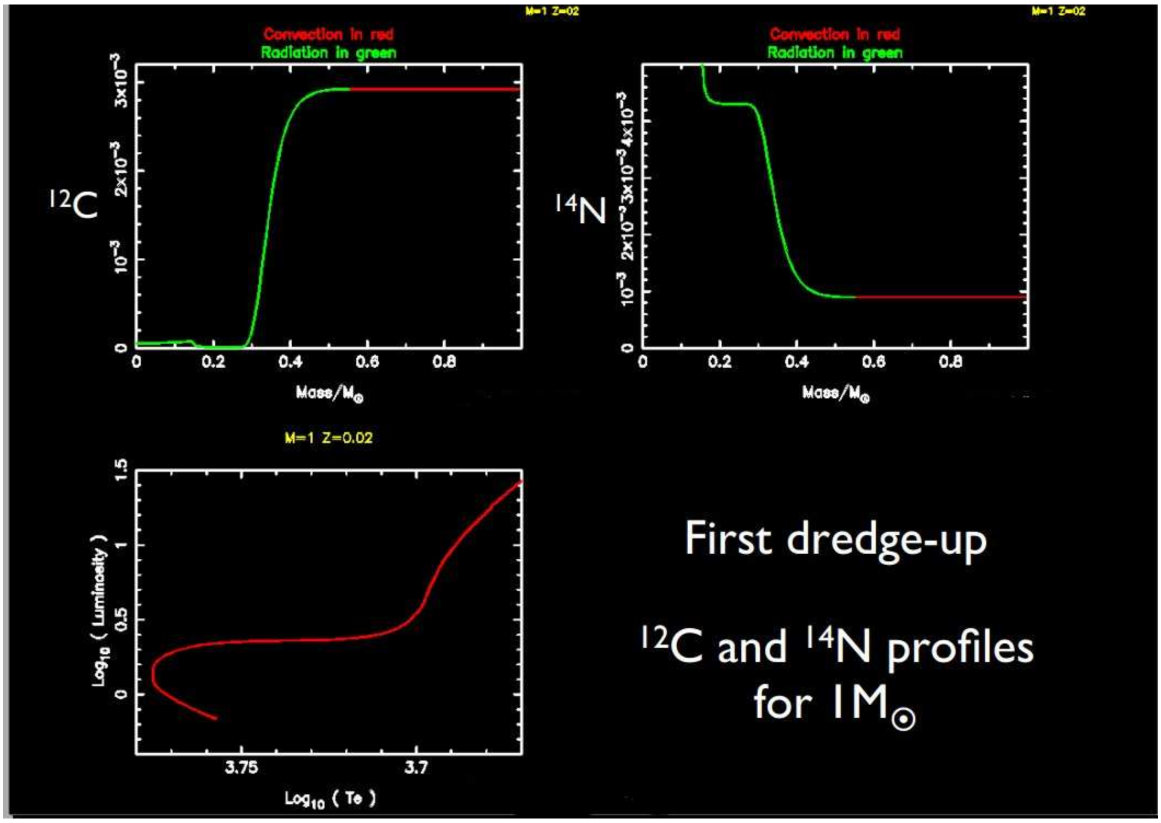

Figure 1.2: First dredge up ^{12}C and ^{14}N profiles for 1M⊙. Reproduced from http://users.monash.edu.au/johnl/StellarEvolnV1/

1.2.2 Asymptotic Giant Branch

The asymptotic giant branch is the final evolutionary point (Karakas 2011) for intermediate mass stars which have mass in the range 0.8 - 8M⊙. AGB stars account for the majority of the luminous red objects in the infrared and hence they provide a great proportion of the luminosity of intermediate age stellar systems. As a result, AGB stars make an excellent tracer of stellar and galactic evolution. In the interstellar medium the majority of the dust comes from mass-losing AGB stars (Izzard & Tout 2003). This makes the study of AGB stars key to help improve our understanding of galactic compositions. The AGB has two parts, the early AGB and the thermally pulsating AGB (TP-AGB). The structure of a star during the TP-AGB phase is schematically depicted in figure 1.4. In early AGB stars the luminosity is dominated by the helium shell burning.

This shell becomes thermally unstable, as it begins to oscillate and the oscillations

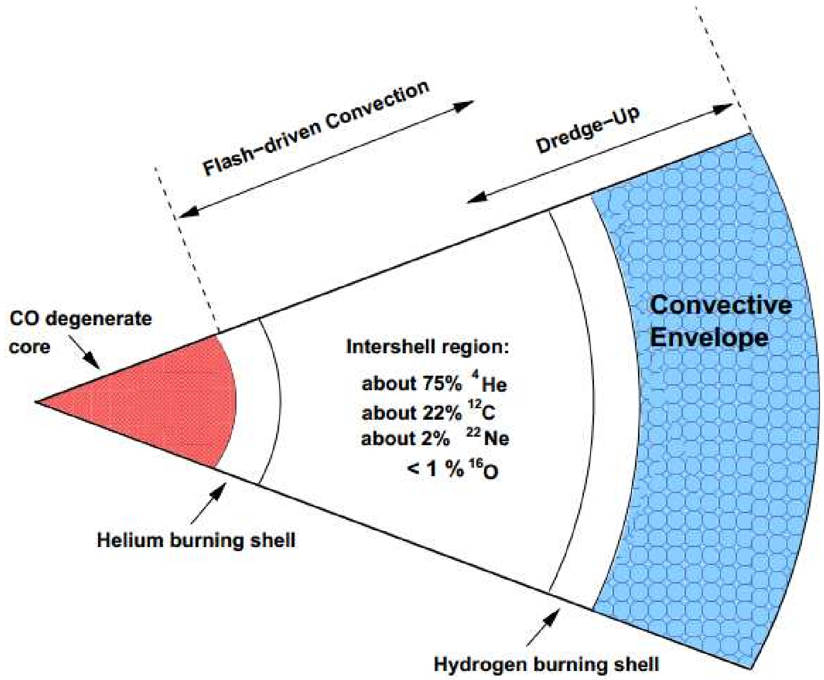

Figure 1.3: Schematic structure of an AGB star showing the degenerate C-O core surrounded by a He-burning shell above the core, and an H-burning shell below the deep convective envelope. It is the intershell region that becomes enriched in *s*-process elements. Reproduced from Karakas, Lattanzio & Pols 2002.

mark the beginning of the TP-AGB phase (Izzard & Tout 2003).

There are a number of distinct zones, including the molecular formation region and the dust formation region. These are controlled by the density and the stellar radiation field and the outermost region where the chemistry is dominated by the impinging interstellar radiation.

1.2.3 Third dredge up and thermal pulses

As the star is thermally pulsating, it will result in matter from deep within the star being dredged up and mixed to the surface, in third dredge up (Marigo, Bressan & Chiosi 1996). The process of the third dredge up will alter the chemical composition of the stellar envelope which has consequences later in evolution. When the stars is in the TP-AGB phase, large amounts of mass loss occur and this shown in figure 1.5. This ultimately leads to the termination of the star's life on the AGB. AGB

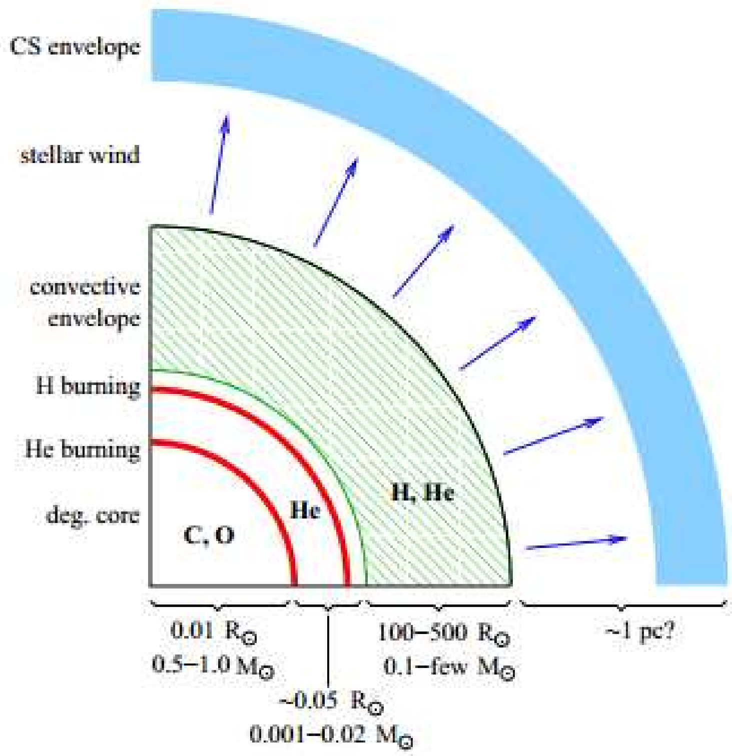

Figure 1.4: The structure of a star during the TP-AGB phase. Reproduced from http://www.astro.uni-bonn.de.

stars are categorised into two main types: oxygen rich (M-type) and carbon rich (C-type) stars, depending on the C/O ratio of the star. The C/O ratio is key in stellar spectroscopy as it controls the chemistry around AGB stars. If the value of the C/O ratio is less than 1, then all the carbon will be bound into carbon monoxide (CO), which forms very easily and is very stable (Kippenhahn & Weigert 2007). Stars with $C/O < 1$ are known as M-type, which are oxygen-rich stars whereas in carbon stars $C/O > 1$. Carbon stars are notable by an abundance of carbon-rich molecules in their atmosphere, such as SiC, rather than SiO of typical M stars. Stars in which with $C/O \approx 1$, are known as S-type stars (Neyskens et al. 2011).

In between the M and C spectral types are the s spectral-type stars. These S-type stars show ZrO lines in their atmospheres in addition to the TiO lines from M stars. The process of the third dredge-up (Iben & Renzini 1983) occurs during the TP-AGB. Due to the sudden increase in the energy flux from the helium-burning shell during a flash episode a convection zone is established between the helium-burning

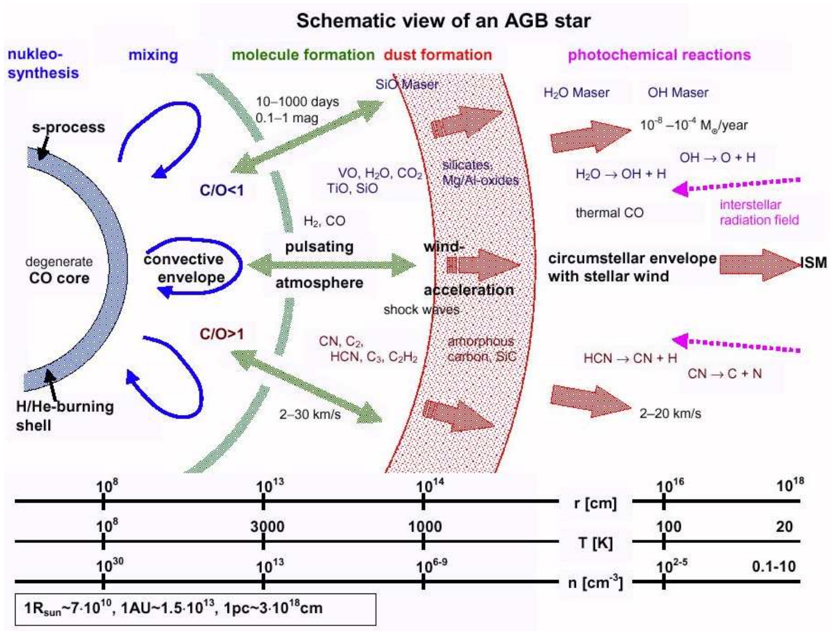

Figure 1.5: Mass-losing AGB star, the top half of the plot shows the chemistry in an oxygen-rich environment (C/O $<$ 1), and the bottom half of the figure shows the carbon-rich counterpart. There are a number of zones and this includes the molecular formation region and the dust formation region. Which are controlled by the density and the stellar radiation field, and the outermost region where the chemistry is dominated by the impinging interstellar radiation. Reproduced from http://www.univie.ac.at/agb/agbdetail.html.

shell and the hydrogen shell (Bradel & Ostile 2007). The energy which is produced during the helium shell burning, then flows out the stellar core resulting in the increase in luminosity escaping from the core. This results in the convective envelope extending inwards in mass. When the convective envelope penetrates regions where nucleosynthesis took place, this causes the dredge up of newly created helium- and hydrogen-shell burning products. A key consequence of the third dredge up, is the enrichment of the stellar envelope with ^{12}C and with each further thermal pulse further carbon is dredged up to the stellar surface. Third dredge up plays an important role in the formation of carbon stars. The AGB stars which experience the third dredge up also show an over abundance of ^{4}He and some s-process elements in their stellar envelopes. It is this s process over-abundance, observed in the spectra of AGB stars, which provides direct evidence of the 3rd dredge-up phase (Wood 2010).

1.3 Stellar Abundances and Nucleosynthesis

1.3.1 Galactic ecology

The Universe began with the Big Bang and at this time hydrogen and helium were essentially the only elements that were produced by the nucleosynthesis. Hence the first stars that were formed did so with hardly any metal content; Z= 0. The fraction by mass of heavy elements is denoted by Z (most of the metal poor stars in the Milky Way (MW) have Z = 10^{-5} - 10^{-4}). Consequently the next generation of stars that formed were extremely metal poor, having very low values of Z. The subsequent generation of stars that formed, result in higher and higher proportions of heavier elements, leading to metal-rich stars for which Z may reach values as high as 0.03 (Bradel & Ostile 2007). Stars are generally classified according to the relative abundance of heavier elements and the star's chemical composition can be characterized by table 1.1.

Table 1.1: Star's chemical composition

	Fraction by mass	Solar value
Hydrogen content	X	0.70
Helium content	Y	0.28
Everything else (C, O, Mg, Si etc: "metals")	Z	0.02

In reality, a broad range of metallicities exist in stars. To quantify the important parameter of composition, the ratio of iron to hydrogen has become almost universally adopted because iron lines are generally readily identifiable in stellar spectra. Supernovae eject iron, which in turn enriches the interstellar medium. Subsequent stars can then be created with greater abundance of iron in their atmosphere than in their predecessors. The ensuing iron content should correlate with stellar age, the youngest and most recently formed stars having the highest relative abundance of iron. The iron-to-hydrogen ratio in the atmosphere of a star is compared with the Sun's value through the following expression and this quantity is often used as an approximation for the metallicity:

$$[\text{Fe/H}] = \log_{10}[(N_{Fe}/N_H)_{star}/(N_{Fe}/N_H)_{sun}] \tag{1.1}$$

where N_{Fe} and N_H are the number of iron and hydrogen atoms per unit of volume respectively. Stars which have an abundance which is identical to the Sun's have [Fe/H] = 0.0. Stars which are metal poor have negative values of [Fe/H] and metal rich stars have positive values of [Fe/H]. Oxygen would be a better tracer and chronometer of metal enrichment (Wheeler, Sneden & Truran 1989) due to fact that it is the most abundant metal. Metallicity is determined by the [Fe/H] ratio, rather than [O/H] ratio, since the [O/H] ratio is much more difficult to measure in stellar atmospheres.

This apparent correlation between age and composition is referred to as the Age-Metallicity Relation (AMR) (Philips 2004). The age-metallicity relation is a very important tool for understanding the chemical evolution of a Galaxy (Kontizas et al. 2001). The AMR for nearby stars is a record of the gradual chemical enrichment of the star-forming interstellar medium during the evolution of the Galactic disk and hence provides clues regarding the star formation and chemical evolution history of the local environment (Carraro, Ng & Portinari 1998).

1.3.2 Enrichment timescales

A supernova is a stellar explosion that briefly outshines an entire galaxy, radiating as much energy as the Sun is expected to emit over its entire life span (Bartunov & Tsvetkov 1986). Supernova are classified based on the presence or absence of features in their optical spectra taken near maximum light. Supernova that show H in their spectra are Type II, and those that did not are Type I (Minkowski 1941). Type I supernovae can be found both in elliptical and spiral galaxies, while type II supernova are mainly observed in the spiral arms of galaxies and in H II regions, but not in elliptical galaxies.

Type I supernovae can be further sub-divided, based on the presence or absence of Si and He in their spectra. Type Ia supernovae have a obvious Si absorption at 6150Å, and type Ib have no Si (Foley & Mandel 2013) but show He emission lines, and type Ic display neither Si nor He. Studying the chemical abundance of long-lived stars provides strong insight into the nucleosynthesis in supernovae (SNe) and detailed chemical compositions (Tsujimoto & Bekki 2012) for very-metal-poor stars in the Galaxy (McWilliam et al. 1995; Cayrel et al. 2004). Type II SNe, first contribute to the chemical enrichment in the Universe, however due to the time delay until the explosion, the nucleosynthesis products from Type Ia Sne (SNe Ia) are superimposed on the interstellar medium later, which is already enriched by numerous SNe II.

This makes it challenging to assess SN Ia nucleosynthesis through observed data of stellar abundances. Type Ia supernovae result from mass transfer inside a binary system consisting of a white dwarf star and an evolving giant star and Type II supernovae are, in general, single massive stars which come to the end of their lives in a very spectacular fashion. Type Ia supernova (SNe Ia) produce more Fe than α elements. In terms of the synthesis of heavy elements by supernovae, Type Ia are responsible for Si, S Fe, while Type II are responsible for O, Mg, Si, S, Fe as shown in figure 1.6.

The chemical composition of stellar populations in galaxies provides crucial constraints on their evolutionary histories. Iron-peak elements are mainly produced in Type Ia supernova on relatively long time scales, while alpha-elements (oxygen, magnesium, calcium, etc.) are produced on shorter time scales in Type II Supernovae. The relative abundances of these and other elements therefore contain important information on the star-formation histories of the parent galaxies. However, until now, the MW has been the only (large) galaxy where it is possible to study chemical evolution in detail (McWilliam 1997).

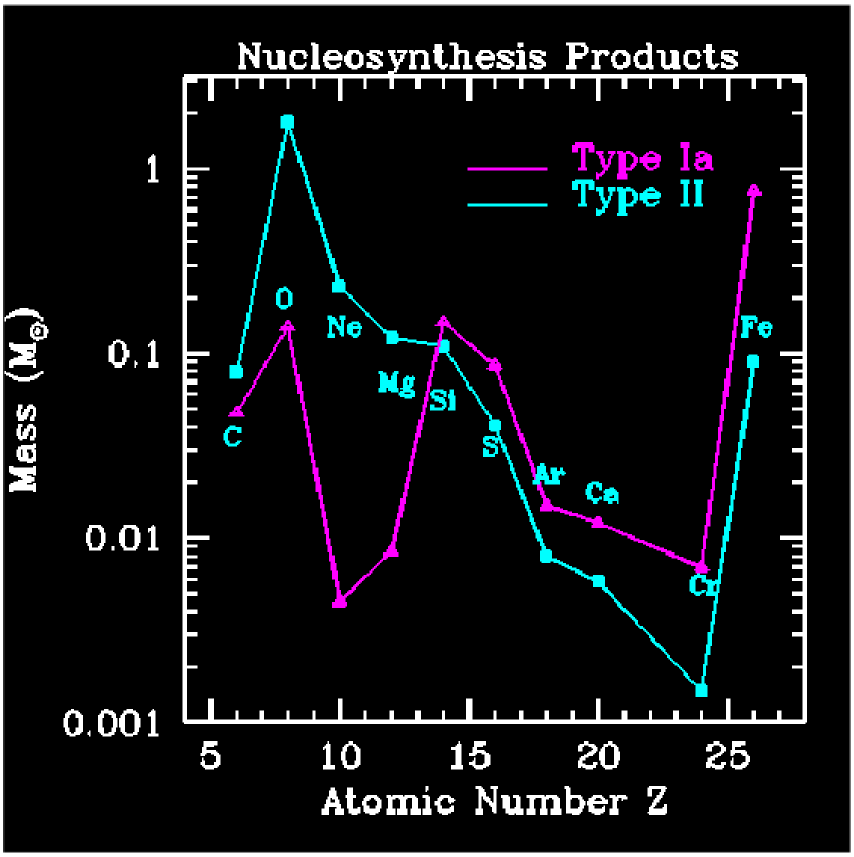

Figure 1.6: Elemental production in Type Ia and II supernova. Reproduced from http://hyperphysics.phy-astr.gsu.edu/hbase/astro/.

1.3.3 Galactic evolution

s and *r* process

The *s*-process is responsible for producing the most of the elements, which are heavier than iron. These isotopes are created via slow-neutron capture deep within the star (Iben & Truran 1978; Dray & Tout 2003). Nuclei which have progressively higher values of Z (the number of protons) form via stellar nucleosynthesis; this makes it difficult for the other charged particles, such as protons and alpha particles, to react with them. This is because of the existence of a high Coulomb potential barrier. These same limitations do not exist when neutrons collide with these nuclei. The resulting, nuclear reactions involving neutrons can occur even at relatively low temperatures, assuming, of course, that free neutrons are present in the gas. The reactions with neutrons

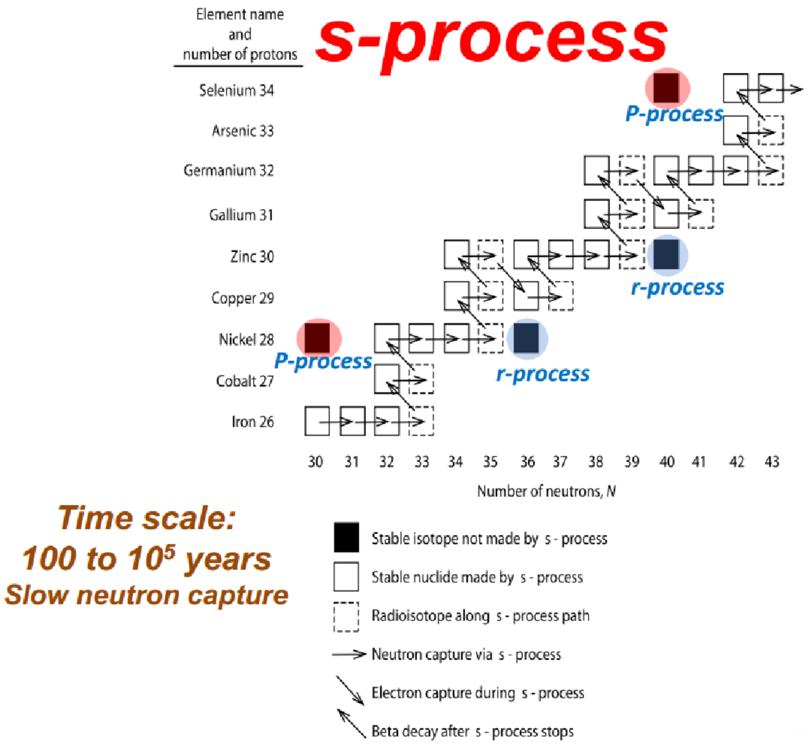

Figure 1.7: The s process, neutron captures increase the mass number through reactions and the products will beta-decay until a stable or long-lived isotope is reached. Reproduced from http://www.geol.umd.edu/hcui/highTemp.html

$$^{A}_{Z}X + n \rightarrow +^{A+1}{}_{Z}X + \gamma \tag{1.2}$$

result in more massive nuclei that are either stable or unstable against the beta-decay reaction,

$$^{A+1}{}_{Z}X \rightarrow^{A+1}_{Z+1} X + e^{-} + \overline{\nu_e} \tag{1.3}$$

If the beta-decay half-life is short compared to the timescale for neutron capture, the neutron-capture reaction is said to be slow process or an s-process reaction. Figure 1.7 show the s-process.

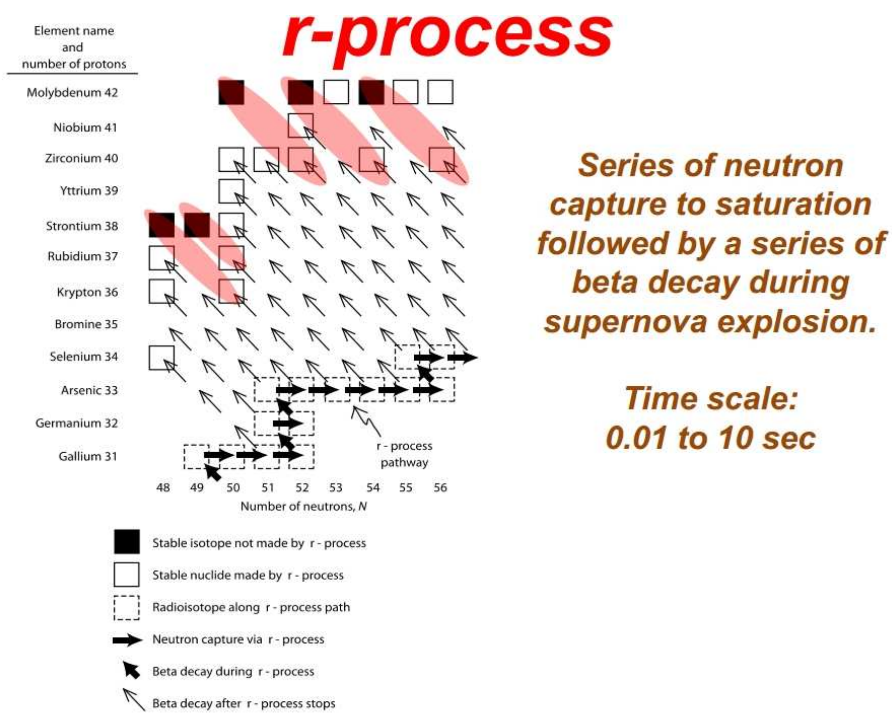

Figure 1.8: r-process, nucleosynthesis of neutron-rich nuclei via rapid neutron capture. Reproduced from http://www.geol.umd.edu/ hcui/HighTemp.html.

s-process reactions tend to yield stable nuclei, either directly or secondarily via beta decay. The synthesis of s-process elements requires a source of free neutrons that can be captured by iron seeds to build up heaver nuclei along the isotopic stability valley (Bonačić Marinović et al. 2007). The dominant reactions that can liberate neutrons are $^{13}C(\alpha, n)$ ^{16}O and $^{22}Ne(\alpha, n)$ ^{25}Mg. In these reactions, the neutron-rich isotopes-rich isotopes, ^{13}C and ^{22}Ne give up excess neutrons to heavier nuclei (Lugaro et al. 2003).

On the other hand, if the half-life for the beta-decay reaction is long compared with the time scale for neutron capture, then neutron-capture reaction is termed a rapid process or r-processes and results in neutron-rich nuclei, figure 1.8 shows the r-process. The r-process requires high neutron densities and it is believed to occur during explosives phases of stellar evolution (Nova, Supernovae and or x-ray binaries).

s-process reactions tend to occur in normal phases of stellar evolution, whereas r-processes can occur during a supernova when a large flux of neutrinos exists (Lugaro et al. 2003). Although neither process plays a significant role in energy production, they do account for the abundance ratios of nuclei with A>60. The *s*-process produces approximately half of isotopes of the elements heavier than iron and therefore plays an important role in galactic chemical evolution. The *s*-process is believed to occur mostly in AGB stars. In contrast to the *r*-process which is believed to occur over time scales of seconds in explosive environments, the *s*process is believed to occur over times scales of thousands of years, passing decades between neutron captures. Figure 1.9 shows an Z versus N diagram showing the production of isotopes by the *s*, *p* and *r* processes.

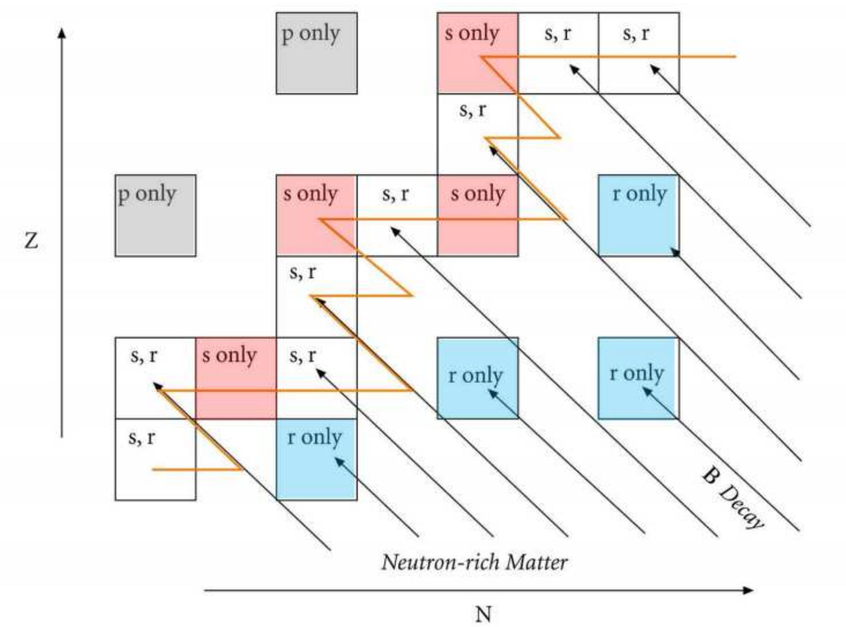

Figure 1.9: Shows Z versus N diagram showing the production of isotopes by the *s*, *p* and *r* processes. Squares are stable nuclei; orange lines are the beta-decay path of neutron-rich isotopes produced by the *s*-process; solid line through stable isotopes shows the *r*-process path. Reproduced from White (2012).

α elements

The α elements are O, Ne, Mg, Si, S, Ca and Ti. They are mainly produced during SNe II explosions. α-elements enhancement in metal-poor stars was firstly identified by Aller & Greenstein (1960) and further supported by Wallerstein (1962), who discovered an excess of Mg, Si, Ca and Ti relative to Fe. Tinsley (1979) suggested that the declining [α/Fe] trend with [Fe/H] is due to the time delay between SN II, which produce α-elements and Fe-peak elements (Woosley & Weaver 1995) and SN I a which yield in mostly iron-peak with little α-element production. Hence after some delay for the onset of SN Ia the [α/Fe] ratio declines from the SN II value.

The abundances of the α-elements can be measured in spectra. The α-elements have been thought of as a homogeneous group and their abundances are in some cases are averaged to produce a single [α/Fe] ratio, but their individual nucleosynthetic origin is not always the same. O and Mg are produced during hydrostatic He burning in massive stars and their yields are not expected to be affected by type II supernova (SNe II) explosion conditions. This difference has been seen in observations, where Si, Ca and Ti usually track one another, however O and Mg often show different trends with [Fe/H] (Tolstoy, Hill & Tosi 2009).

The α elements are measured as ratio of α elements to Fe. The [α/Fe] ratio is used to trace star formation in galaxies because it is sensitive to the ratio of SNe II to SNe Ia that have happened in the past. Since SNe Ia have a longer timescale than SNe II, as they start to contribute, they dominate the Fe enrichment and [α/Fe] predictably decreases. The result of which is that no star-formation history can take place which results in an enhanced [α/Fe], unless it is coupled with galactic winds. Which are responsible for removing (Tolstoy, Hill & Tosi 2009) only SN Ia ejecta and not that of SNe II. This can been seen as the 'knee' (the knee marks the time of the first SNI a) in the plot of [Fe/H] versus [α/Fe] (figure 1.10). The α-element enrichment is therefore a signature of chemical enrichment by massive stars, which are progenitors of SNII with very little contribution from lower mass

SNIa progenitors (Zoccali & Minniti 2009).

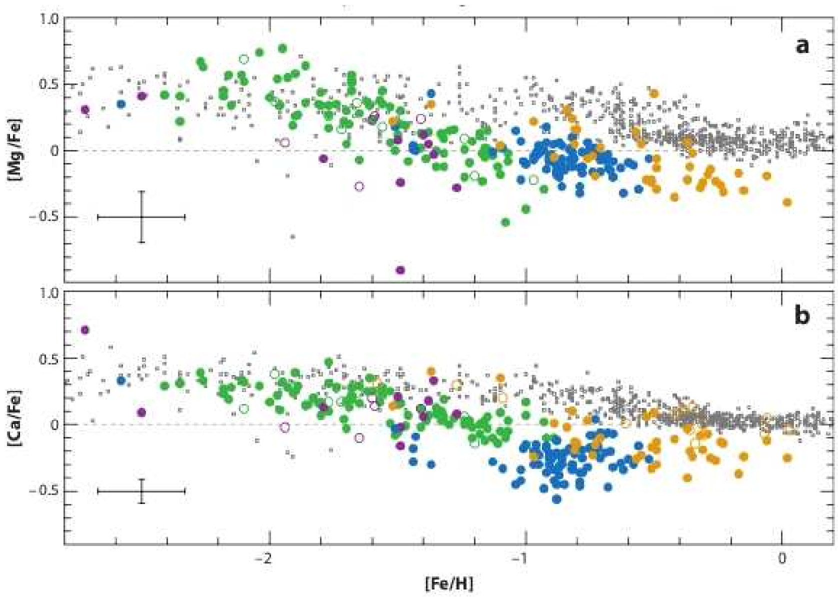

Figure 1.10: α elements (a) Mg and (b)Ca, in four nearby by dwarf spheroidal. The Sgr dSph (orange), Fnc dSph(blue), Scl dSph(green), and dSph Carina(purple). Reproduced from Tolstoy, Hill & Tosi (2009).

For example in figure 1.10 the position of the knee points to metal-enrichment which has been obtained by a galaxy at the time Sne Ia start to contribute to the chemical enrichment evolution (Matteucci & Brocato 1990). This is typically between 10^8 -10^9 years after the first star-formation period. In the case of galaxy which produces and keeps metals over this time period will reach a higher metallicity by the time SNe Ia start to contribute than a galaxy which either loses a large portion of metals in galactic winds or simply does not have a very high star-formation rate (SFR).

Abundance ratios can be used as a diagnostic of the initial mass function (IMF) and SFR parameters for chemically evolving systems. It was proposed by Tinsley (1979) that SN Ia progenitors have longer lifetimes than the SN II supernovae progenitors. Theoretical predications of SN II elements yields show that [α/Fe] increases with increasing progenitor mass, meaning the IMF of stellar system could be inferred from observed [α/Fe] ratios (Woosley & Weaver 1995).

The [α/Fe] ratio is also sensitive to the SFR (Tinsley 1979). If the SFR is high, then the gas will reach higher [Fe/H] before the first SN Ia occur and hence the position of the knee in the [α/Fe] versus [Fe/H] in figure 1.11 will be at a higher [Fe/H].

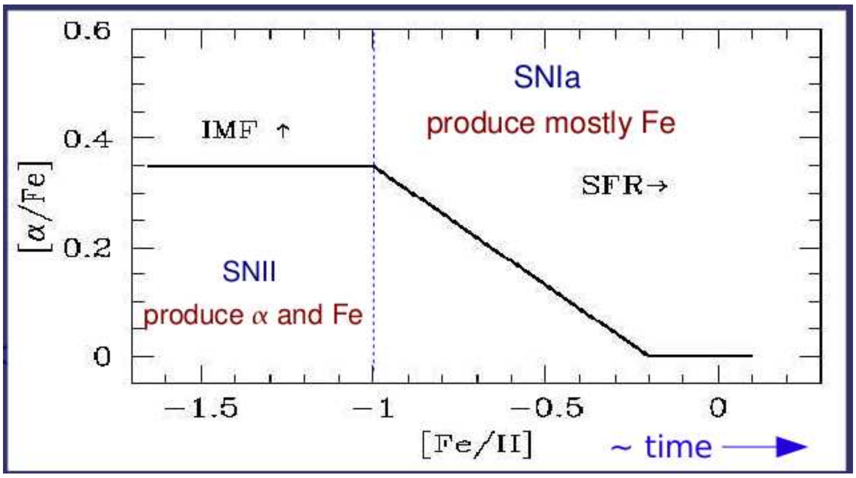

Figure 1.11: The trend of α-element abundance with metallicity. Where the increased IMF and SFR affect the trend in the directions indicated. The knee in the figure is probably due to the onset of type Ia supernovae. Reproduced from McWilliam (1997).

The formation time scale of a stellar system can be estimated by noting the fraction of stars with [Fe/H] below this knee point (figure 1.11). The α-elements in the Galactic Bulge show an unusual mixture of abundances. This is thought to be because stars of different masses produce different α-elements yields (figure 1.12) (Woosley & Weaver 1995).

Figure 1.12 shows the enhanced Mg observed in the Bulge could occur with relatively more 35-$M_{\odot}$ SN progenitors than in the Galactic Disk and the observed Ti enhanced is not explained by any SN nucleosynthesis predictions. The Ti enhancements which are seen in the Bulge stars present a qualitative explanation for the spectral type of Bulge M giants is later than disk M giants with the same temperature (more TiO absorption).

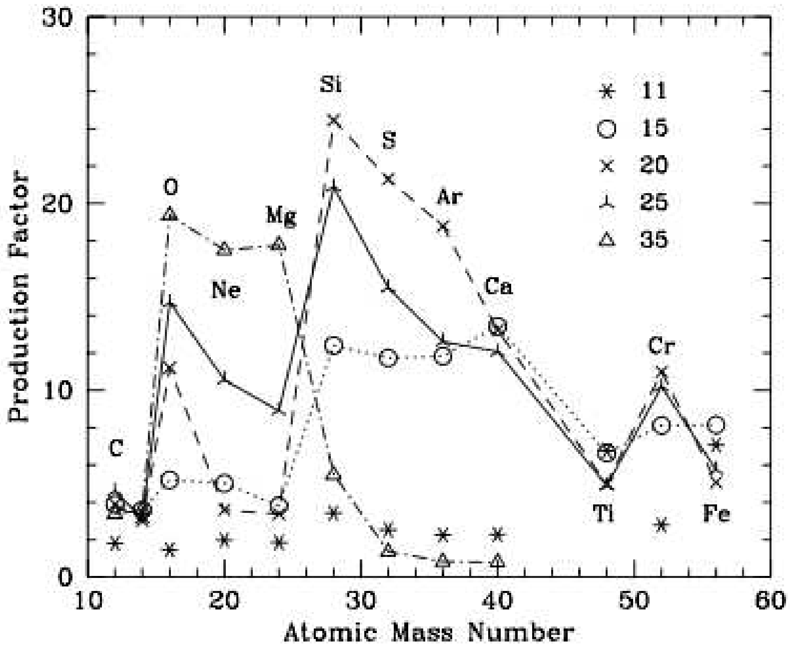

Figure 1.12: In the diagram the ejected elemental abundances for various progenitor are shown by the symbols. In the case of O and Mg they are produced in large quantities at high mass ($\sim$ 35M$_\odot$) but not in the lower mass (15-25$M_\odot$) SN. They are responsible for the majority of Si and Ca production. The models don't give considerable enhancements of Ti relative to Fe, which is in contrast to observations of stars in the Galactic Bulge. Reproduced from Woosley & Weaver (1995).

1.4 Metal-Poor Populations

Great progress has been made in quantifying the ages of the stars in the dwarf spheroidal galaxies (dSph) through colour-magnitude diagrams (CMD) due to increased use of wide-field charge-coupled device (CCD) cameras (Smecker-Hane & McWilliam 1999). Most dSph in the local group have complex star-formation histories (Smecker-Hane 1997), beginning to form stars $\sim$ 14 Gyr ago during the the period of globular cluster formation in our Galaxy. Some of the dSphs lost their gas and as a result stopped forming stars relatively quickly (Hernandez, Valls-Gabaud & Gilmore 1999) (e.g. Ursa Minor), however some dSphs continued forming stars (Mighell & Rich 1996) for many Gyr (e.g. Leo II), while other dSphs continued to form stars until 1 or 2 Gyr ago.

The majority of dSphs formed stars over many dynamical timescales (few x 0.1 Gyr), despite their low velocity dispersions ($\sim$ 10km/s). These dSphs were able to retain and recycle gas even though thousands of SNe have exploded in them and a critical observation about dSphs is that they form stars slowly (Smecker-Hane 1997).

Looking at the chemical abundance patterns of metal-poor stars offers a insight into the properties and role of the first generation of stars (Norris et al. 2013). The progenitors of these objects may have had zero metallicity and were the first stars to form in the Universe. The most chemically primitive stars in the MW hold important clues concerning the earliest phases of the formation and evolution of the Galaxy.

Population I-III stars represent the variety of metallicities we see today in the Galaxy. After the Big Bang, stars started out with Z = 0 and this increased with time to Z$\simeq$ 0.02, which we see today. The current value of Z depends on the availability and retention of gas by a population, which allows it to form progressively heavier stars.

Metal-poor populations are usually found in Globular Clusters and Dwarf Galaxies. Population I stars are metal rich, with Z $\sim$ 0.02, Population II stars are metalpoor, with Z $\sim$ 0 - 0.01, and Population III stars are essentially devoid of metals, with Z $\sim$ 0. Understanding metal-poor stars (Population II stars) is a key step towards a better understanding of the processes involved in evolving an early Universe of H and He to the metal-rich universe seen today. At high redshifts it is only possible to see Population II & II stars as light from these stars is only just reaching us.

The comprehensive evolutionary histories of dwarf galaxies are of particular interest because they are low-metallicity systems and hence they are assumed to be highly evolved. Of late, dwarf galaxies have been of particular interest due to their cosmological importance as possible building blocks of large systems. Nearby dwarf galaxies such as Sgr dSph are the closest we can get to the detailed study of a primordial system (Tolstoy, Hill & Tosi 2009). Dwarf galaxies typically have relatively simple structures and often have very low metallicities. It is assumed that small systems are the first to collapse in the early Universe; galaxies like were the first to form and are thus potential hosts of the first stars. Since dwarf galaxies were widespread throughout the early Universe, this make them suitable candidates to be able to re-ionize the Universe uniformly and rapidly (Tolstoy, Hill & Tosi 2009).

Recently large samples of stellar abundances of individual stars in nearby dwarf galaxies have been obtained (Monaco et al. 2007; Letarte, Hill & Tolstoy 2007). These will provide information on the chemical evolution through time and, in turn, will help determine the accurate evolutionary path of these small systems and their contribution to the build up of metals in the Universe.

Dwarf galaxies are most abundant type of galaxy in the local universe (Marzke & da Costa 1997), however they are hard to detect due to their low luminosity, low mass and small size. They are typically found in galaxy clusters (Popesso et al. 2006), often as companions to larger galaxies. Dwarf galaxies are categorized into three main types (Tolstoy, Hill & Tosi 2009; Marcolini et al. 2006):

1. Dwarf Elliptical Galaxies (dE) – These have many properties which are observed in normal elliptical galaxies but on a smaller scale. This type of galaxy has very little gas and there is no evidence of recent star formation. They have low metallicities. One of the most nearby dEs is M32, a satellite of the Andromeda Galaxy.

2. Dwarf Spheroidal Galaxies (dSphs) – These type of galaxies are more spherical than elliptical and tend to be much smaller than Dwarf Ellipticals. Due to their size and mass, these types of galaxies have so far not been seen much outside the Local Group.

3. Dwarf Irregular Galaxies (dI) – This type of galaxy has properties which are akin to larger irregular galaxies and they contain large amounts of gas and dust, along with evidence for ongoing star formation.

1.4.1 Explaining low metallicity in dwarf galaxies

A key issue in chemical evolution models of dwarf galaxies has been reconciling the low observed metallicity with the high SFR, as especially seen in blue compact dwarfs (BCDs). Four possible processes have been put forward to help explain these observations (Chiosi & Matteucci 1983):

1. The variations in initial-mass function, steeper initial-mass function-slopes or mass-range cut-offs have been suggested to reduce the chemical enrichment from massive stars.

2. The enrichment of a galaxy can be reduced by the affects of accretion of metal-free and very-metal-poor gases.

3. Galactic winds, which can occur as a result of supernova explosions in systems that have a shallow potential well.

4. Gas stripping via interactions with other galaxies, or metal-enriched gases being removed from a system via stripping by the intergalactic medium.

Explaining the low metallicity of dwarf galaxies may need one or a combinations of these processes and is still a matter of discussion (Tolstoy, Hill & Tosi 2009).

1.4.2 The [α/Fe] trends

Variations in the α-elements abundances are of particular interest because accurate values of [α/Fe] in pre-AGB stars set constraints on the star-formation history (Ryde et al. 2010). The α elements are synthesized by core collapse SNe II, while Fe is also synthesized by Type Ia Sne (Marconi, Matteucci & Tosi 1994). In the MW at low metallicities the [α/Fe] ratio is higher than at solar metallicity. Figure 1.13 shows the [α/Fe] versus [Fe/H] for the Sgr dSph and figure 1.14 for Galactic Bulge.

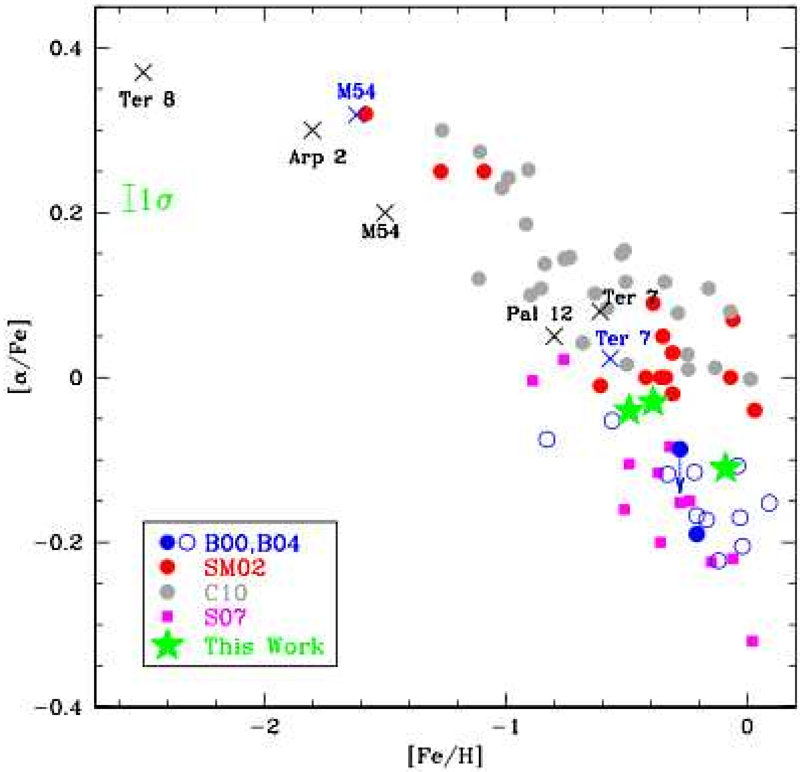

Figure 1.13: [α/Fe] versus [Fe/H] ratios for the Sgr dSph. The Sgr dSph from previous work, the grey circles (Carretta et al. 2010;C10), red circles(Smecker-Hane & McWilliam 2002;SMO2), open blue circles (Bonifacio et al. 2000, 2004), and magenta squares (Sbordone et al. 2007;CO7) and the green stars (McWilliam, Wallerstein & Mottini 2013). Reproduced from McWilliam, Wallerstein & Mottini (2013).

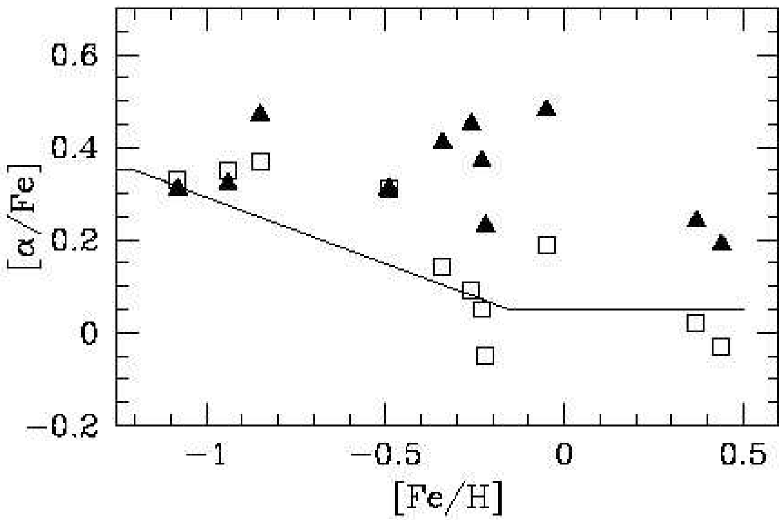

Figure 1.14: Trends of alpha-element abundances in the Galactic bulge. Reproduced from McWilliam & Rich (1994).

1.5 The Sagittarius Dwarf Spheroidal Galaxy

1.5.1 Structure

The Sgr dSph Galaxy or Elliptical Galaxy was discovered by Ibata, Gilmore & Irwin (1994). It is the second nearest dwarf galaxy to the MW. This metal-poor galaxy lies at a relatively close distance of ∼25 kpc (Giuffrida et al. 2010; Sbordone et al. 2007; Lagadec et al. 2009), closer to all but the newly discovered Canis Major Dwarf Galaxy (Martin et al. 2004). Despite its relative closeness, the Sgr dSph represents a challenge from an observational point of view, due to its very low surface brightness (in order to adequately populate the brightest part of the colour-magnitude diagram, sampling needs to carried out over a wide field) and the strong contamination by foreground stars. Despite its size, the Sgr dSph wasn't discovered until recently owing to the fact that is located behind the Galactic Bulge, hence statistical decontamination of colour-magnitude diagrams is required (Bellazzini, Ferraro & Buonanno 1999b).

The Sgr dSph covers a large area of the sky, with dimensions of approximately 15^o x 7^o (Giuffrida et al. 2010). The Sgr dSph has a short orbital period around the

MW of < 1Gyr (Sbordone et al. 2007; Bellazzini, Ferraro & Buonanno 1999b). The Sagittarius stream is long complex, structure made of stars that wrap around the MW in an almost polar orbit. It consists of stars which have been tidally stripped from the Sgr dSph. Figure 1.15 shows a model of the Sagittarius star stream torn by the MW (Lokas et al. 2012). Due to tidal effects the Sgr dSph is being destroyed (Koposov et al. 2012) by our Galaxy; the MW is accreting the dwarf galaxy by tidal stripping and will eventually integrate it completely.

Tidal tails are produced by tidal forces from two interacting galaxies. The resulting forces will distort the galaxies and, as a consequence of orbiting each other for a short period, the distorted regions are pulled away from the main body of each galaxy. Due to the galaxy differential rotation, the distorted regions will be sheared and this results in them being cast off into space and forming tidal tails.

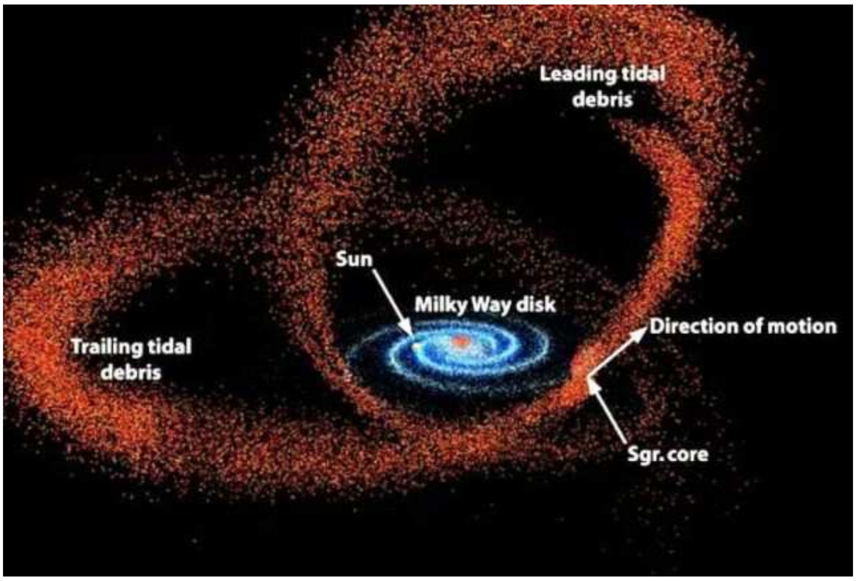

Figure 1.15: Model of model of the Sagittarius star stream torn by Milky Way. Reproduced from http://www.imagejuicy.com/images/space/sagittarius/5/.

1.5.2 The chemical composition of Sagittarius Dwarf Spheroidal Galaxy

The chemical composition of the Sgr dSph is very unlike that of the MW. There are considerable under-abundances of α-elements and other light elements such as Na, Al, Sc, V, Co, Ni, Cu and Zn, in comparison to Galactic stars with the same iron content. Additionally, over-abundances of La, Ce and Nd have been detected, as well as wildly different abundance ratios (Sbordone et al. 2007).

The galaxy contains a number of known populations and they are generally summarised into five separate groups by (Siegel et al. 2007).

- A considerable metal-poor population which has a [Fe/H] of ≈ –1.2 dex and t = 10–12 Gyr, which is mostly widespread in the fringes.
- Extremely metal-poor population which has a [Fe/H] of –1.7 dex, [α/Fe] ≈ +0.2 dex and an age of t≈ 13 Gyr (globular cluster M54).
- Within the galaxy there is a spread of metallicity within the bulk population and this ranges from [Fe/H] ≈ –0.7 to 0.4 dex, [α/Fe] ≈ +0.2 dex and the age ranges from t = 4 Gyr to t = 8 Gyr (Bellazzini et al. 2006).
- A diminutive higher-metallicity population with a [Fe/H] ≈ +0.4 to –0.1 dex, [α/Fe] ≈ +0.2 dex and t = 2-3 Gyr; (Sarajedini & Layden 1995; Siegel et al. 2007).
- A likely, but minuscule, metal-rich population with a [Fe/H] ≈ +0.5, [α/Fe]≈ 0 dex, t <1 Gyr (Siegel et al. 2007).

The Sgr dSph's most evolved AGB stars should be close to the lower mass limit for carbon-richness (McDonald et al. 2012). Previous works have noted several carbon stars in the galaxy, and linked them to the metal-rich population (Lagadec et al. 2009). The Sgr dSph provides a opportunity to study the stellar content and the star formation history of a dwarf spheroidal galaxy and the possible influence of the interactions with a parent galaxy on the SFH (Bellazzini, Ferraro & Buonanno 1999a,b).

It was discovered by Chou et al. (2007) that a metallicity gradient exists within the stellar part of the tidal stream being accreted by the MW, with more-metal-rich stars having been stripped from the Sgr dSph more recently. Currently no stellar population has been found within the MW which has the same chemical abundances as the dwarf spheroidal. Chou et al. (2007) showed that there is a vast difference between current chemical compositions of dwarf spheroidals and the stars they have accreted in the past.

1.5.3 The chemical evolution of Sagittarius Dwarf Spheroidal Galaxy

The abundances ratios of the various elements provides the clues to the chemical evolution of the Sgr dSph galaxy. Figure 1.16 shows the [X/Fe] vs [Fe/H] which is observed in the Sgr dSph galaxy compared to the predictions of the chemical evolutions models for the Sgr.

The most simple diagnostic is the [Fe/H] and in the case of the Sgr dSph the mean value of [Fe/H] is near –0.5 to –0.7 dex (Cole 2001; Bellazzini2008; Siegel2007), which is lower than the MW. This lower-than average value for [Fe/H] may be due also due to significant mass loss during its evolution, which truncated chemical enrichment before complete conversion of the gas into stars occurred (McWilliam 1997). A similar gas-loss mechanism was put forward to explain the low average [Fe/H] of the MW Halo by Hartwick (1976).

The outflows are more likely in low mass galaxies like the Sgr dSph than the MW. This is due to the relative shallow gravitational potential well, which would allow more high-velocity supernova ejecta to leave than for massive galaxies. Since tidal

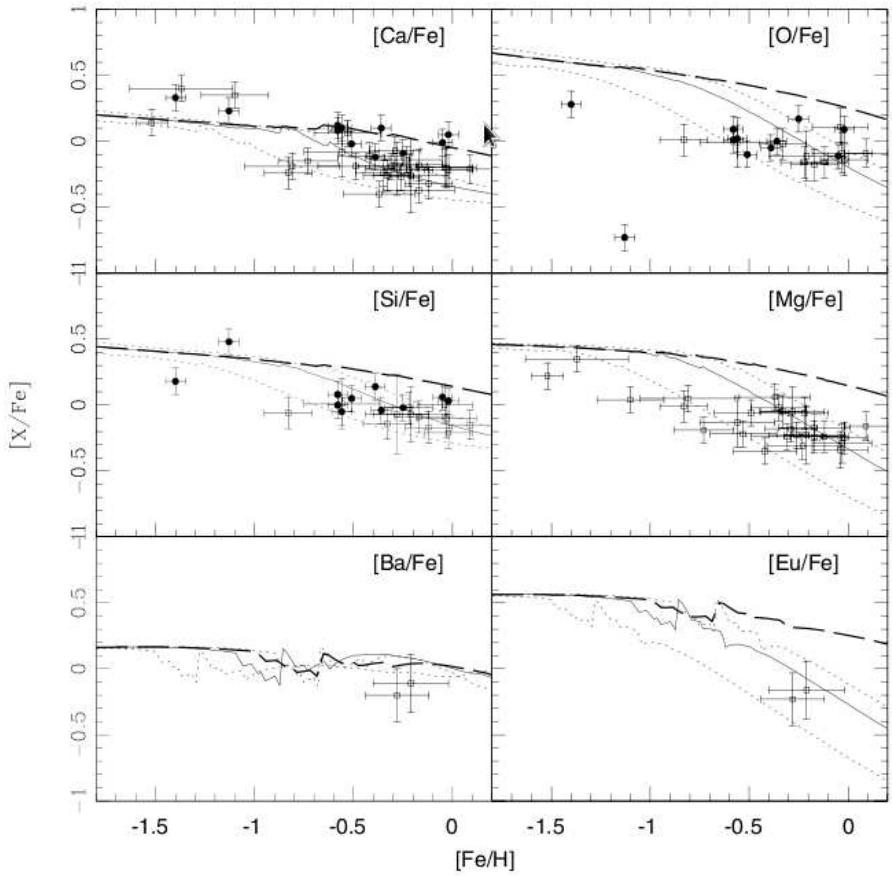

Figure 1.16: The diagram shows the [X/Fe] versus [Fe/H] observed in the Sgr dSph galaxy. The observed results are compared to predictions of chemical evolution model for the Sgr dSph. The dashed lines show the best model without galactic winds, while the solid line shows the best model and the dotted lines for upper and lower limits for the star formation efficiency. Reproduced from Lanfranchi, Matteucci & Cescutti (2006).

stripping is occurring in the Sgr dSph, this also must be a important gas-loss mechanism for the Sgr dSph as supported by the prominent stellar tidal tails, as the Sgr dSph almost contains no gas today. An alternative to overall mass loss is selective mass loss, an example of this is, energetic is material from SNIa or SNII ejecta which are more likely to be ejected from Sgr dSph, than low velocity ejecta from planetary nebulae. In considering the overall metallicity, selective mass loss from SNII and or SNIa would produce in a lower yield of metals per stellar generation and this would result in a reduction of gas to be recycled into the stars. Both of these mechanisms would result in a lower mean [Fe/H].

Alternatively, this lower mean [Fe/H] could also be due to a steep stellar IMF (Recchi et al. 2014). For example in the closed box model of chemical evolution (Caimmi 2011), the average metallicity for a galaxy, after all the gas is consumed, is equal to the yield. The yield is the ratio of the mass of the metals produced divided by the mass which is locked up in low mass stars (Searle & Sargent 1972). A system which had steep IMF slope, will subsequently have a smaller yield. The mean metallicity will, therefore be lower than for a normal IMF slope. For a steep IMF more gas is locked up in low-mass stars, which leaves fewer high-mass stars to produce the metals and hence the final average metallicity is lower (McWilliam, Wallerstein & Mottini 2013).

1.6 The Galactic Bulge

The central part of our MW consists of the Galactic Bulge (GB), the central part of the Halo and the Galactic Centre. The bulge contains $\sim 10^{10}$ $M_\odot$ of stars or $\sim 20\%$ of the total stellar mass of our galaxy (Kent, Dame & Fazio 1991). Understanding the formation of elliptical galaxies and the bulges of spiral galaxies, helps us to build a better understanding of galaxy formation and star-formation history (Zoccali et al. 2003). The evaluation of the GB of the MW is active area of research and bulges are thought to be similar to elliptical galaxies with possible origins in minor mergers (Gesicki et al. 2014). This is supported by the relation between bulge/spheroid luminosities and their central black-hole masses (Graham 2007). Within the MW bulge there is evidence for old stellar populations along with young stellar populations.

The metallicity is close to the solar abundance (Vanhollebeke, Groenewegen & Girardi 2009) and when considering the age and duration of star formation in the GB, there is evidence that the metal-poor and and metal-rich populations are formed at different times with metal-poor population extending over 2 Gyr and metal-rich over 4 Gyr (Tsujimoto & Bekki 2012; Bensby et al. 2010, 2011, 2013).

Bensby et al. (2010) showed that stars with sub-solar metallicities are mainly old, typically around 10 Gyr, as expected in the GB. However at super-solar metallicities, it cab be shown that there are a wide range of ages with a peak around 5 Gyr and a tail towards the higher ages. Bensby et al. (2010) concluded that the origin of the GB is poorly constrained and hypothesises that the young stars might be the manifestation of the inner thin disk. Gonzalez et al. (2011) found evidence for a separate, high metallicity component of the bulge, which they attribute to stars originating from the thin disk.

The Galactic Bulge (GB) is observable within 20^0 x 20^0 around the Galactic centre, the corresponding angular size encloses a radius of 2.8 kpc (Barbuy et al. 2008). The bulge is the spheroidal component at the centre of the MW (Zoccali & Minniti 2009) and its total mass is about 1.6 x 10^{10} M$\odot$ (Popowski et al. 2005; Hamadache et al. 2006) which is approximately four times smaller than the disk (7.0 x 10^{10} $M_\odot$) and 16 times larger than that of the halo ($\sim 10^9$ $M_\odot$). There are various theories on its formation and they include primordial free-fall collapse or remnants of accretion episodes and secular evolution of bar instabilities (Fulbright, Rich & McWilliam 2006).

The Bulge was investigated as this allows a good comparison with Sgr dSph galaxy as they have similar age but has very different formation histories. There have been various studies of Bulge stars (Johnson et al. 2013, 2014; Gonzalez et al. 2011) who found the mean abundance of the Bulge, [Fe/H] <–0.5 dex, [Ti/Fe] = 0.40 dex and [Si/Fe] = 0.35 dex. Metal-poor stars with [Fe/H] = –0.2 dex show a extraordinary homogeneity at different locations within the Bulge. McWilliam & Rich (1994) and Zoccali et al. (2003) found that the Bulge metallicity spans a wide distribution from [Fe/H] $\sim$ –1.5 to $\sim$ +0.5 dex, with a peak around [Fe/H] = –0.2 dex. Figure 1.17 shows abundance trends for the α elements in the bulge.

In comparison to the Sgr dSph, the mean [Fe/H/]= 0.6 dex and [Fe/H] ranges approximately from –2.0 dex to 0.0 dex, which is similar to the Sgr dSph. The thick disk stellar ages covers range of approximately 5 Gyr (Reddy, Lambert & Allende

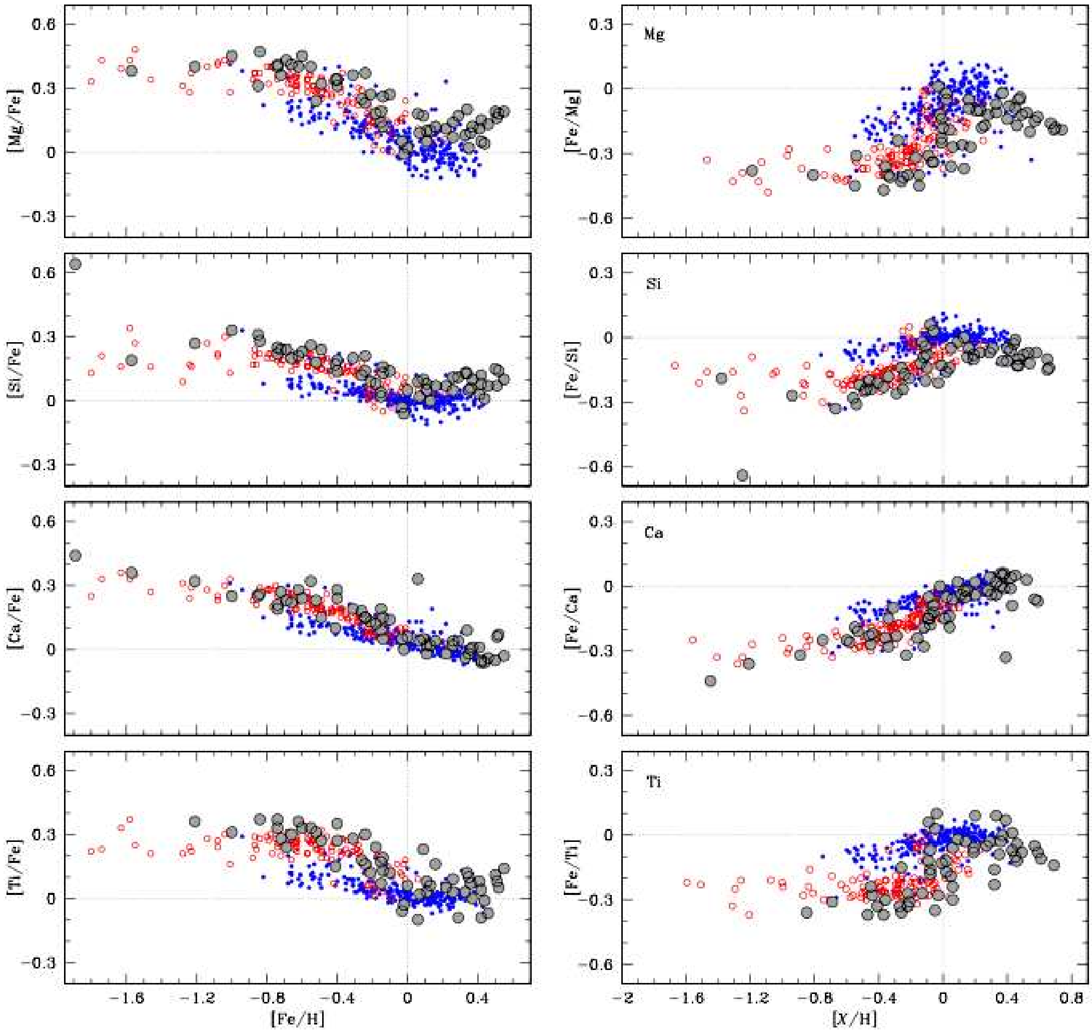

Figure 1.17: The abundance trends for the α elements (Mg, Si, Ti, Ca) in Bulge. The left hand side shows the [X/H] versus [Fe/H, where X = Ca, Si, Ti, Ca and the right hand side shows the [Fe/X] versus [X/H]. The grey circles indicate the microlensed Bulge dwarf stars and the red and blue circles are thick and thin dwarf stars. Reproduced from Bensby et al. (2013).

Prieto 2006), similar to the age difference between the two Sgr dSph ,populations which have studied by Siegel et al. (2007) and because the thick disk composition is well measured. Hence the metallicities and time scale are similar for both these to systems (Galactic Bulge and Sgr dSph), so any chemical composition differences are less likely to be due to metallicity or time scale parameters.

1.7 The Project

Over the last few years, a considerable amount of observing time has been devoted to the analysis of dwarf spheroidal galaxies of the Local Group. These galaxies have been favoured for analysis because of their relative proximity, which enable several observational constraints to be determined with high accuracy (e.g. SFHs, total mass, elemental abundances, abundances ratios etc.). From observations that have been carried out, the dSphs are characterized by low star efficiencies, with complex SFHs (Lanfranchi, Matteucci & Cescutti 2006). Some of these galaxies contain metal-poor, young metal-rich, intermediate, or even mixed populations of stars and have central regions which is almost depleted of neutral gas (Lanfranchi, Matteucci & Cescutti 2006).

The aim of the project is to develop a better understanding of chemical enrichment of the Sgr dSph galaxy. In order to understand the how the Sgr dSph evolved, the abundance ratios need to be compared to a standard population and for this reason the Galactic Bulge stars were chosen. As a result, 27 stars both in Sgr dSph and Galactic Bulge galaxies were selected for analysis. The abundances of Ca, Si, Ti and Fe were measured for both galaxies. Subsequently, the [α/Fe] value is going to be calculated and this will allow a comparisons to made of the chemical evolution in both galaxies.

In Chapter 2, I will discuss how the target stars were selected in the Sgr dSph and Galactic Bulge along with how the abundances of the Fe and Ca, Si and Ti are calculated. The [Fe/H] results for the Sgr dSph will also be presented in this chapter. In Chapters 3, I will present the results for the α-elements for the Sgr dSph. While in Chapter 4, I will present the [Fe/H] and α-elements results for the Galactic Bulge. In Chapter 5, I will discuss how the Bulge and Sgr dSph results compare along with how the results in this project compare with published data. In Chapter 6, I will draw together the project's conclusions.

Chapter 2

Determining the abundance of elements within stars

2.1 Stellar types and spectral lines

The spectrum can tell us a range of things which includes the temperature and composition of a star. A stars atmosphere is mostly hydrogen and there are small traces of other elements, which all contribute to producing the spectrum of a star. Figure 2.1, shows how the various atoms and molecules contribute to the formation of spectral lines as function of temperature (Vakarchuk, Rykalyuk & Yankiv-Vitkovska 1998).

By looking at individual spectral lines, it is possible to identify which atoms are causing them and work out how strong they are by measuring their equivalent widths (EW). From this it is possible to determine how much of that element exists, provided that the surface temperature and surface gravity of the star can be calculated. The effective surface temperature of star, T_E, is defined as the temperature of the black body of the same size which would give the same luminosity. For a star of luminosity L and radius R

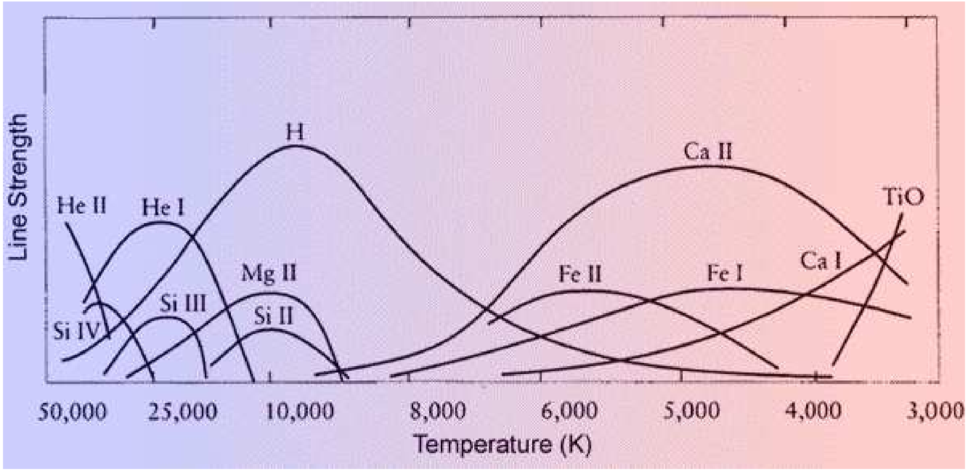

Figure 2.1: How temperature affects the strength of spectral lines. Reproduced from http://www.kcvs.ca/martin/astro/au/unit2/63/chp63.html.

$$L = 4\pi R^2 \sigma T_E^4 \tag{2.1}$$

where σ is the Stefan's constant (Philips 2004). As radiation travels through the photosphere (the surface region from where most of the observed radiation originates), radiation at certain wavelengths is absorbed by ions and atoms. This gives rise to a spectrum, which contains dark absorption lines. The absorption lines in the spectrum allow a classification of stars according to spectral type. The spectral type depends on the degree of excitation and ionization of atoms and ions in the photosphere. The resulting spectral type is denoted by a letter O, B, A, F, G, K or M and this sequence largely reflects a steady decrease in surface temperature of the star from 30 000K to 3000K (Philips 2004).

In this project I will be looking at K–type stars which have a surface temperature from 3500-5000K. Figure 2.2 shows the range of temperatures for stars. The spectra for K–type stars shows a lot more metals lines (atomic lines) than M–type stars, which have stronger metal lines but they are masked by molecular features. The M–type stars have surface temperature from 2500-3500 K, which makes them fainter at visual wavelengths when compared to K–type stars. The K–type stars represent a 'sweet spot' between too few lines and too many molecular lines. The cooler the

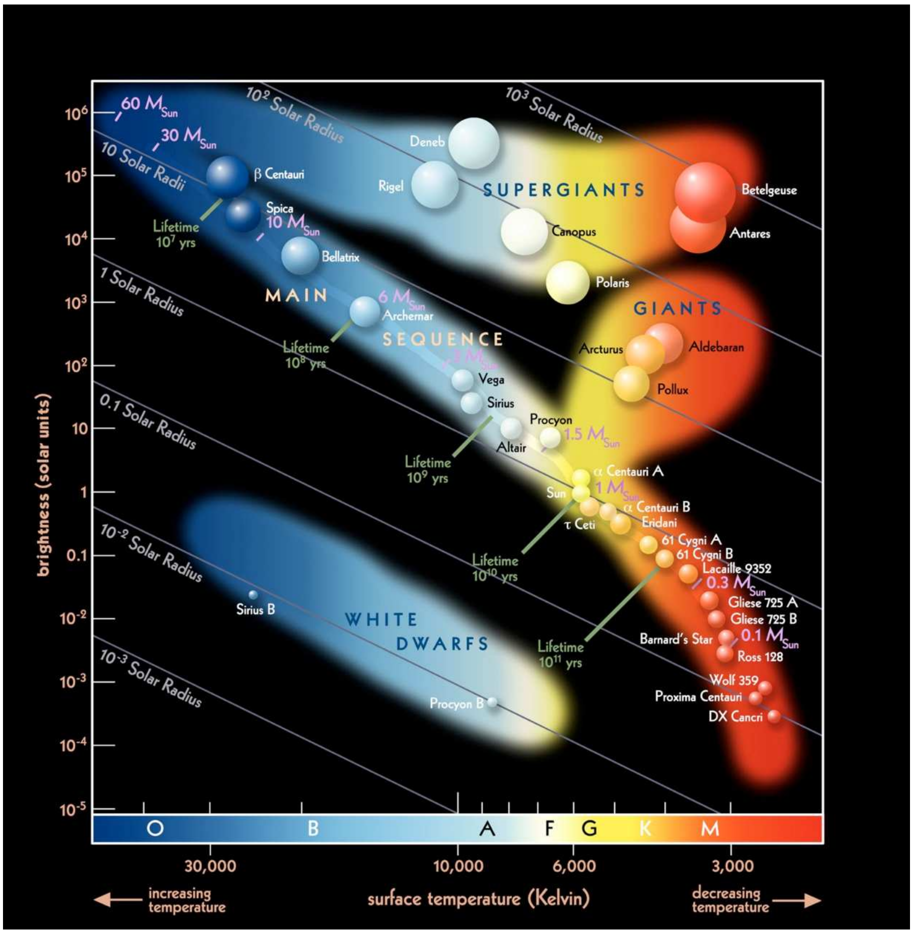

Figure 2.2: The Hertzsprung-Russell diagram showing the range of temperatures in stars. Reproduced from http://astronomyuniverse.pbworks.com.

star, the more "metal" lines are present. Hence the overall spectra for hot stars (e.g. OBA) are relatively smooth (except for the hydrogen lines), while the spectra for cooler stars (e.g. FGK) become more distorted by metal lines. The M stars have spectra so dominated by TiO molecular bands and metal lines that no continuum is visible. Figure 2.3 shows some typical example spectra, from the data I will later be using, selected from stars just below RGB tip (top M-type #105, middle: C-type 1015, bottom: K-type #949), in four observed settings. Notable atomic and molecular lines are shown.

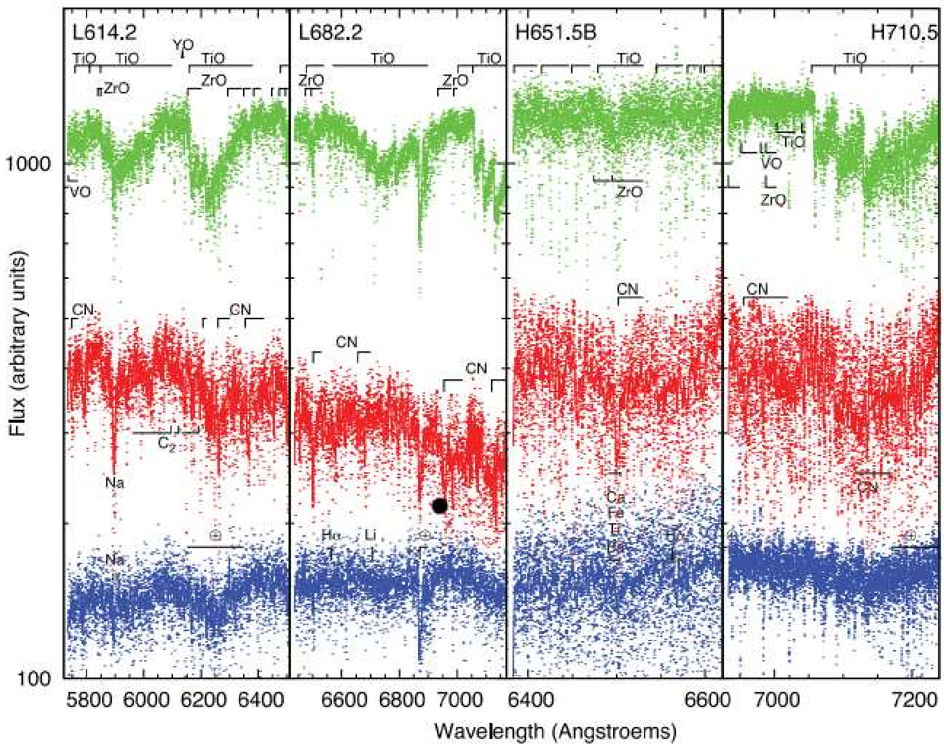

Figure 2.3: Examples of typical spectra, selected from stars just below the RGB tip (top: M-type#105, middle: C–type#1015, bottom: K-type#949), in the four observed filter settings. Notable atomic and molecular lines are shown. Reproduced from McDonald et al. (2012).

2.2 Equivalent widths

Stellar abundances are determined using standard equivalent width (EW) analysis. Figure 2.4 shows the radiant flux (F_λ) as a function of wavelength for a hypothetical absorption line. The EW can be used to describe the relative strength of a line compared to the continuous emission at nearby wavelengths. The flux level of the continuous level is called the continuum level. For an emission line the spectrum rises above this level, while for an absorption line the spectrum dips below this level, as figure 2.4 shows.

$$W_\lambda = \int_{\lambda_1}^{\lambda_2} \frac{F_c - \mathrm{F}_\lambda}{F_c}\, d\lambda \tag{2.2}$$

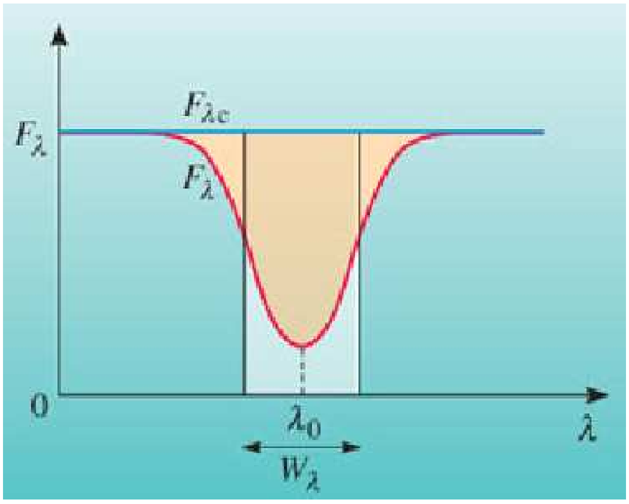

Figure 2.4: The continuum level level, $\mathrm{F}_\lambda c$ (blue) and the absorption line (red). The EW, W_λ is the width of the rectangle of the same height as the continuum. The rectangle has the same area as the absorption line. Reproduced from http://dspace.jorum.ac.uk/

The integral is taken from one side of the line to the other. The EW of a line in the visible spectrum is typically of the order of 0.01 nm (Bradel & Ostile 2007).

2.3 Observations

The data for this project comes from The Very Large Telescope (VLT/FLAMES and VLT/UVES) and 1058 stars were observed in total. The Fibre Large Array Multi Element Spectrograph (FLAMES) is a fibre-fed, multi-object instrument connected to GIRAFFE, a spectrograph which has a medium-high resolution (R = 7500–30 000). It has already been determined whether the stars are carbon or oxygen by work carried out by McDonald et al. (2012). The Arcturus atlas is used as a reference for selecting suitable spectral lines (Hinkle et al. 2000). FLAMES was used to observe the Sgr dSph at both low and high resolution optical spectroscopy over nine fields, covering 1058 stars with GIRAFFE.

The HR16 (TiO/CN) grating has been chosen in order to determine carbon /oxygen-richness. Observations were also taken in the low-resolution LR5 and LR6 settings but were not used in this analysis due to their low resolution. The HR16 (wavelength range 31.3$\AA$ and resolving power of 23 900) and HR14B (wavelength range 24.3$\AA$ and resolving power of 28 800)[1] filters were chosen because of their high resolution, the HR16 and HR14B filters allows the H line to be seen along other metal such as Fe, Ti, Ca and Ba. In this project only K–type oxygen rich stars are going to be looked at and not M or C type stars.

[1]http://eso.org/sci/facilities/paranal/instruments/flames/doc/

2.4 Data Analysis

2.4.1 Target selection

The observed stars for this project were sampled from the 2MASS catalogue (Cutri et al. 2003). The 2MASS ($J - K_{\rm s}$) versus $K_{\rm s}$ CMD for 3° around M54 (taken to be the centre of the Sgr dSph; McDonald et al. (2012)) shows a defined feature which is associated with the Sgr dSph giant branch. Stars within this feature can be separated from the foreground Galactic population by using a colour cut of $K_{\rm s}$ >20.35 – 9 (J –$K_{\rm s}$) mag (McDonald et al. 2013). Data for 1058 stars was collected but not all of theses stars could be analysed (the data is mixed and contains data K, M and C type stars), due to the quality and selection criteria used in the project limited the number of stars which could be selected for analysis.

One of the selection criteria used in this project, is that only K–type stars would be analysed as the lack of molecular lines makes it easier to calculate the equivalent widths. A second inspection for molecular lines was performed. Figure 2.5 shows the distinctive TiO band seen is seen in many of the Sgr dSph stars and hence stars with this type of spectrum are not selected for further analysis.

When looking at Sgr dSph data, the issue of low S/N (table 3.5)made the task of calculating the abundances a very challenging task. This, however, was less of a problem for the GB stars, where the data had higher S/N when compared to the Sgr dSph data. In order to produce a target list of stars to analysis for the Sgr dSph, stars were listed according to the S/N value. From this list, stars with the highest S/N, were selected for further analysis. This involved plotting the spectrum of the star using Gnuplot, to allow a visual inspection to be made of the star's spectrum (stars with molecular bands were discounted). The S/N level determined which stars could be analysed, if the S/N is to low then it very difficult to calculate the EW and set the continuum, due to the amount of noise in the spectrum (if the noise is to great then the lines cannot be accurately identified).

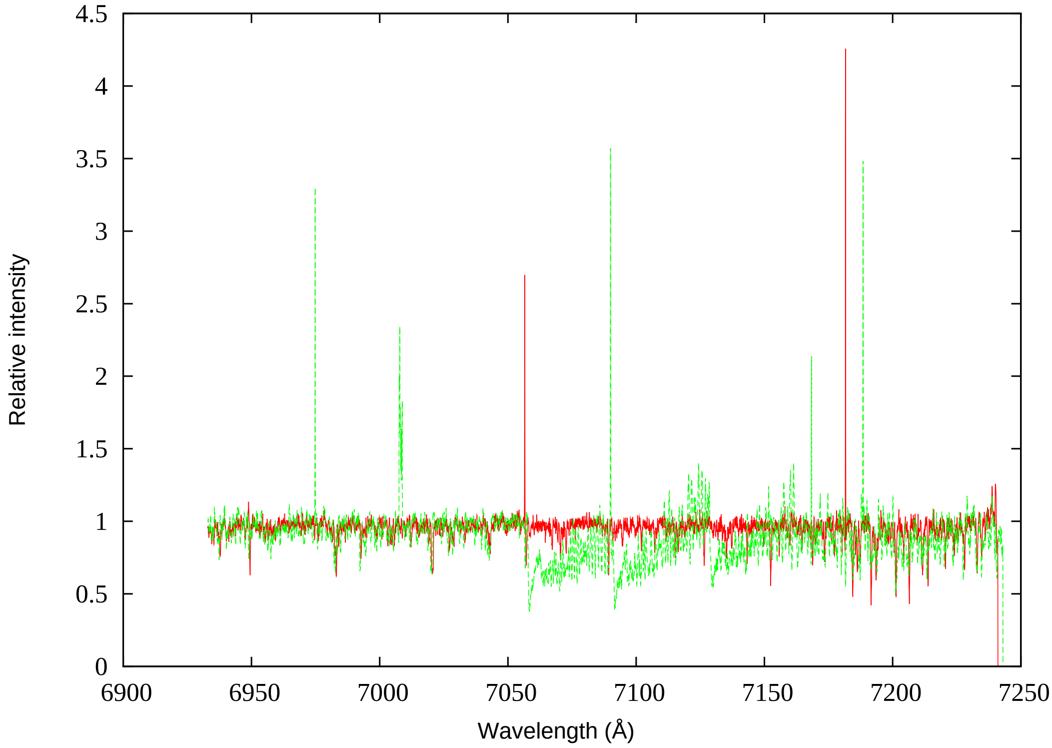

Figure 2.5: P5093 (red) is hotter star (4000K) when compared to P2827(green) which is a cool star and has molecules in its atmosphere, which produces the distinctive TiO band, which are seen between 7050–7150 Å.

If stars with lower S/N had been selected then there would have been some changes in the overall results, as this creates observational bias. Due to the colour cut used when selecting the stars, which results in metal poor stars being preferentially selected. Since metal poor stars have hotter surfaces and their spectra peak is in the infrared, hence metal poor stars are brighter in the optical and have more chance of yielding high S/N spectrum.

Figure 2.6 shows the spectrum for P3222 and P2703 which has molecular bands and therefore was not selected for analysis. In total 27 stars were selected for analysis in the Sgr dSph (only stars with the highest S/N were selected, section 3.1.2 and 4.3). The net overall effect of the above selection criteria is that it allowed the best possible candidates from Sgr dSph to analysed, which helped in reducing the variation in the results.

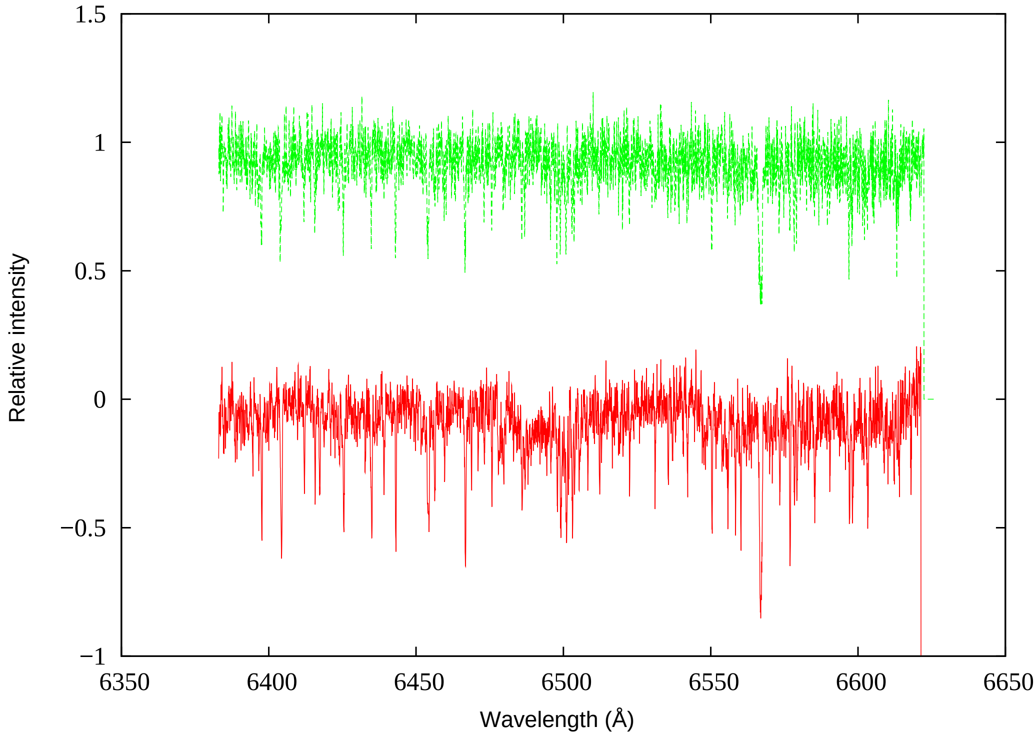

Figure 2.6: P3222 (green spectra) and P2703(red spectra- which has molecular bands in the spectrum) star in the Sgr dSph.

The issue of low S/N was not as a major issue in the data for the GB stars (table 4.6), as this data had generally a higher S/N when compared to the Sgr dSph. In order to produce a target list of stars, the data was visual inspected by using Gnuplot. This allowed confirmation of whether the stars are in the Bulge or whether they are foreground stars. Figure 2.7 shows the spectrum for star 01056, which is a high-gravity foreground dwarf star, while 00956 is a Bulge star with lower surface gravity. In total 27 stars were selected for analysis from the GB. More could have been selected but it was decided to use only 27 as this would allowed an even comparison to be made with the Sgr dSph.

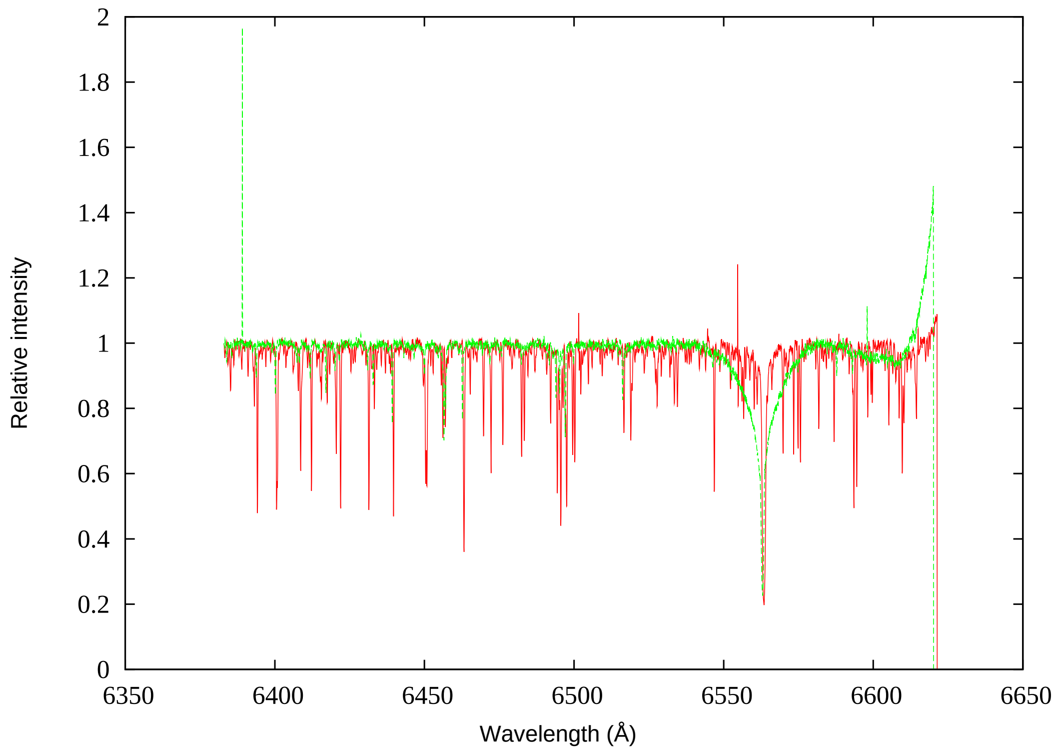

Figure 2.7: 01056(green) is star with high surface gravity(with collisional broadening of the H-α line) foreground dwarf star. 00956 (red) is a low-gravity background Bulge star.

.

2.4.2 Equivalent width determination

Equivalent width software

One of the selection criteria used in this project, is that only K–type stars would be analysed as the lack of molecular lines makes it easier to calculate the equivalent widths. The second selection criteria used is that stars without molecules lines were considered for analysis. Figure 2.5 shows the distinctive TiO band seen is seen in many of the Sgr dSph stars and hence stars with this type of spectrum are not selected for further analysis.

The "abfind" package of MOOG uses equivalent widths (EWs) to fit abundances using a curve of growth method. Consequently, equivalent widths have to be measured for lines of the elements that you want abundances for. The ideal type lines for calculating EW are ones which are clean and don't appear to be blended and have shapes that can be fitted nicely using SPECTRE. The abundances of Fe I and Fe II were calculated by measuring the equivalent widths, using software developed by Johnson et al. (2008), which is an interactive, semi-automatic code. The final abundances are derived using the 2010 version of the LTE line analysis code MOOG (Sneden 1973). The first step in the measurement process involved setting up a parameter file to load into the EW software, this contains the name of spectrum for star, name of the output file for the EW measurement, reference spectrum and linelist for the region wavelength region being looked at. For each star two parameter files were created covering wavelengths which range from 6381-6624$\AA$ and 6931-7246$\AA$. Once the parameter file is loaded, the first step then is to get the spectrum of the star to align with the reference spectrum, this is achieved by shifting the wavelength (velocity shift) of the star until the troughs of both spectra match. After getting the two spectra to align and setting the continuum, single isolated lines were fitted with a Gaussian profile and blended lines were de-blended with up to five Gaussian profiles and then the best fitting profile is selected. Figure 2.8 shows the EW being measured for an Fe I line (P2944)and figure 2.9 shows a Fe I line being de-blending.

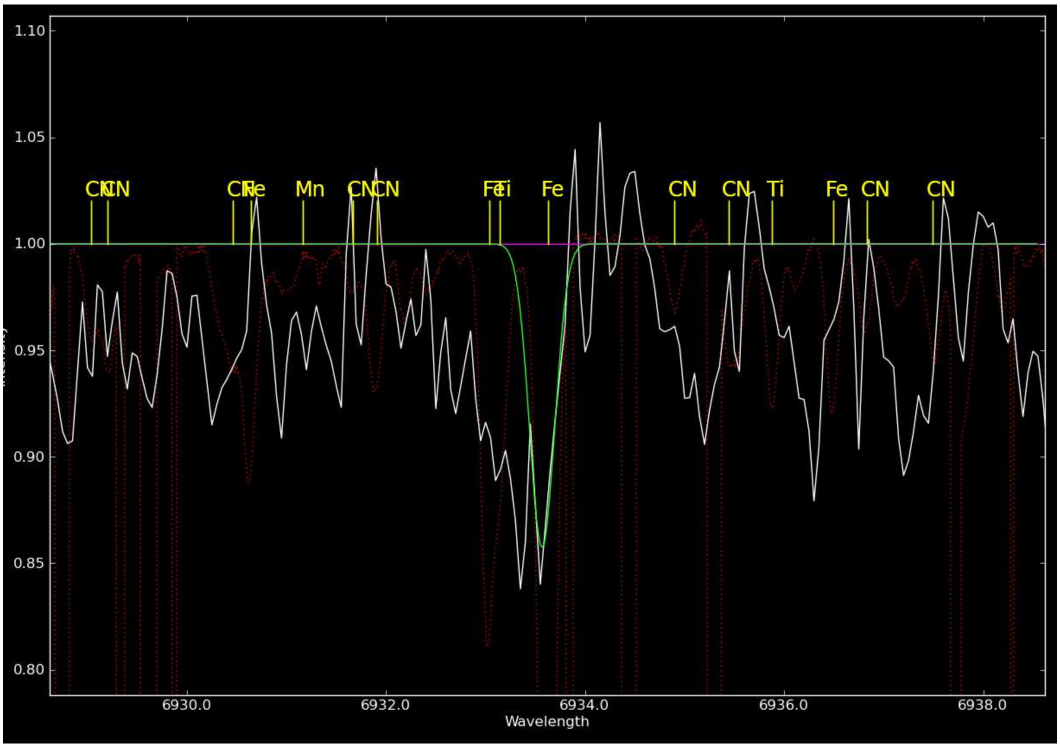

Figure 2.8: Calculating the equivalent width for Fe line for P2944 a Sgr dSph star. The white spectrum is the spectrum of the star being analysed; the red spectrum is the reference star, Arcturus (Hinkle et al. 2000); the green curve is the Gaussian fit matching the star spectrum and the purple line the continuum.

Once the EW are measured for the two wavelengths regions, the results are then combined into a single linelist (which is in the MOOG abfind package format), the data is ordered according to the elements. This file is then used in calculating the chemical abundance of the elements (e.g. Fe I and Fe II) using the MOOG software (Sneden 1973). Atmospheric absorption bands have not been removed (since removing the bands does not greatly increase the accuracy of the final measurements because of the remaining uncertainty in atmospheric removal process) from the spectra and it makes it difficult to measure the EW of the spectral lines in the regions of atmospheric absorption.

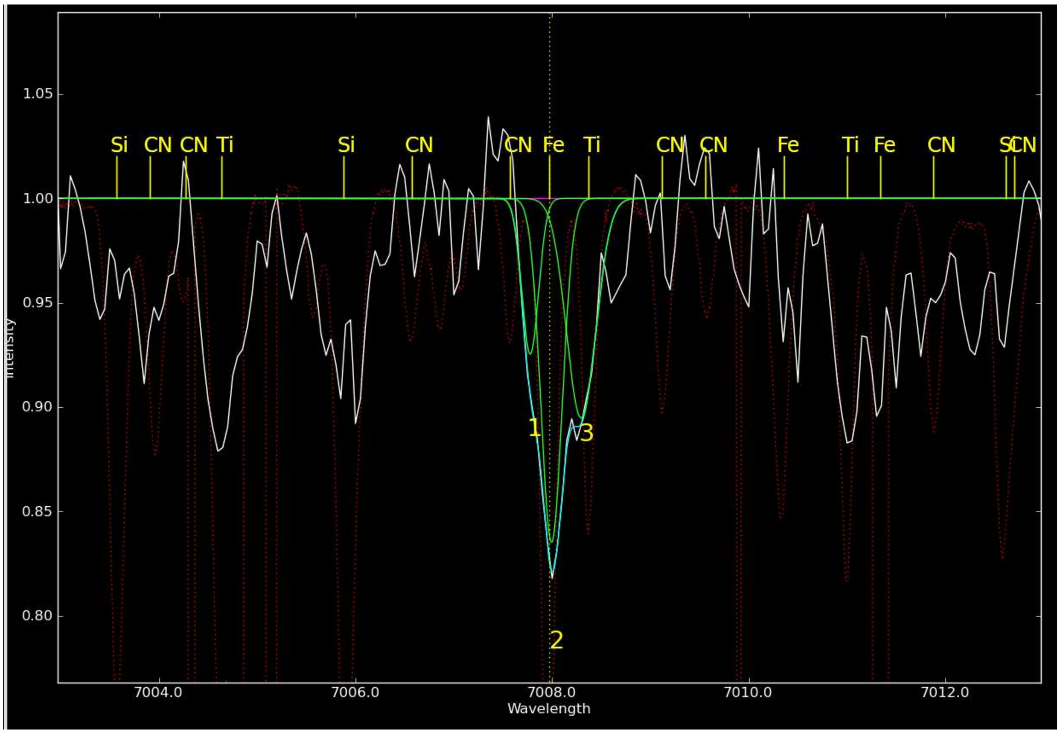

Figure 2.9: A Fe line being de-blended for P5093 a Sgr dSph star. The Fe, Ca and Ti lines are a very close together and have nearly the same intensity. Hence they have to be de-blended in order to measure the equivalent width of the Fe line accurately.

The measurement process followed the standard procedure of fitting single or multiple Gaussian profiles to the spectra for isolated and weakly blended lines respectively. The Sgr dSph stars were selected mainly on S/N (signal to noise ratio) in an effort to reduce the measurement uncertainties. The effects of low S/N make the task of calculating EW very difficult because it is difficult to see the lines of the elements due to noise. The two linelists used when finding the EW for Fe I (where a line of neutral iron is denoted by 26.0, its atomic number) and Fe II (26.1, the decimal tells MOOG that the ionization state of the next line is coming next, where .1 is a single ionized state) are shown in table 2.1 and 2.2. The excitation potential of the line is the minimum potential required to excite a free neutral atom from its ground state to a higher state. The log (gf) gives the probability that the specified transition will occur for a given line and is the largest source of uncertainty for some lines (Epstein et al. 2010; Johnson & Pilachowski 2010). In theory there were 54 observable Fe I lines and 3 Fe II lines. However it not always possible to measure this many lines due to the the quality of the data especially in the case of the Sgr dSph data.

Table 2.1: The atomic linelist used for 6931–7246$\mathring{A}$ part of spectrum for finding equivalent width of Fe I.

Wavelength ($\mathring{A}$)	Ionization State	Excitation Potential (eV)	log (g_f) (dex)
6933.62	Fe I	2.43	–3.598
6936.48	Fe I	4.61	–2.280
6945.20	Fe I	2.42	–2.452
6951.25	Fe I	4.56	–1.061
6951.62	Fe I	4.28	–2.562
6971.93	Fe I	3.02	–3.480
6999.88	Fe I	4.10	–1.510
7000.61	Fe I	4.14	–2.126
7007.97	Fe I	4.18	–1.870
7038.22	Fe I	4.22	–1.150
7071.86	Fe I	4.61	–1.600
7083.40	Fe I	4.91	–1.382
7086.73	Fe I	3.60	–2.677
7090.38	Fe I	4.23	–1.090
7091.92	Fe I	4.96	–1.478
7112.17	Fe I	2.99	–3.008
7114.55	Fe I	2.69	–4.080
7151.47	Fe I	2.48	–3.600
7179.99	Fe I	1.49	–4.770
7212.44	Fe I	4.96	–1.102
7219.68	Fe I	4.08	–1.680

Table 2.2: The atomic linelist used for 6381–6624Å part of spectrum for finding equivalent width of Fe I and Fe II.

Wavelength (Å)	Ionization State	Excitation Potential (eV)	log (g_f) (dex)
6385.72	Fe I	4.73	–1.850
6392.54	Fe I	2.28	–4.090
6393.60	Fe I	2.43	–1.562
6400.00	Fe I	3.60	–0.470
6400.32	Fe I	0.92	–4.178
6408.02	Fe I	3.69	–1.128
6411.65	Fe I	3.65	–0.755
6412.20	Fe I	2.45	–5.063
6416.92	Fe II	3.89	–2.447
6419.64	Fe I	3.94	–2.580
6419.95	Fe I	4.73	–0.280
6430.85	Fe I	2.18	–1.886
6432.68	Fe II	2.89	–3.587
6436.41	Fe I	4.19	–2.410
6456.38	Fe II	3.90	–2.155
6469.19	Fe I	4.83	–0.260
6475.62	Fe I	2.56	–2.832
6481.87	Fe I	2.28	–2.934
6483.94	Fe I	1.49	–5.638
6494.50	Fe I	4.73	–1.176
6494.98	Fe I	2.40	–1.313
6495.74	Fe I	4.83	–1.060
6496.47	Fe I	4.79	–0.650
6498.94	Fe I	0.96	–4.489
6518.37	Fe I	2.83	–2.620
6533.93	Fe I	4.56	–1.380
6546.24	Fe I	2.76	–1.556
6551.68	Fe I	0.99	–5.970
6556.79	Fe I	4.80	-1.638
6569.21	Fe I	4.73	–0.350
6574.23	Fe I	0.99	–4.923
6581.21	Fe I	1.49	–4.789
6592.91	Fe I	2.73	–1.603
6593.87	Fe I	2.43	–2.342
6597.56	Fe I	4.79	–1.040
6609.11	Fe I	2.56	–2.632

Fitting

The analysis of the data for the Sgr dSph has been challenging and this has been mainly due to S/N issues. A key issue has been setting/placing the continuum when measuring the EW's for each star. The continuum has been difficult to set especially for Sgr dSph data because it is hard to find the mean of the noise, the spectra have been hard to normalize properly and it has been difficult to determine what is a spectral line. If the continuum is set too high or too low this greatly effects the EW's of each line. If the continuum is set too high, this then results in an overestimation of the EW's and if the continuum is set too low then this results in an underestimation of the EW's. This then affects the calculations the abundances of each the elements. It also affects the model atmospheres parameters (e.g. T_{eff}, log(g), [Fe/H] and υ_t) for each star. This issue of where to set the continuum has not been an issue when analysing the Galactic Bulge stars.

The other issue which has made analysing the Sgr dSph stars spectra difficult is line broadening of the spectra. There are two mechanisms which produce line broadening, they are Doppler broadening and collision induced broadening. The effects of broadening due the instrument and macroturbulence are also important. The effects of Doppler and collision-induced broadening are generally worse in the Bulge compared to the Sgr dSph because the Bulge stars are higher gravity stars and, because they are smaller they rotate faster (Carlberg 2014), which results in greater Doppler broadening of the spectra. The Bulge stars are more dense and this results in greater number of collisions per molecule.

The broadening, results in a lack of sharpness in the spectrum line which causes the broadening. This broadening made calculating the EW's more time consuming and difficult, in order to measure the Fe I and Fe II , the line spectra for each star had to de-blended. The majority of stars analysed in the Sgr dSph data had to be de-blended and this is due to the selection criteria used when selecting the stars to analysed, as K–type stars are cooler and they have more lines than hotter stars. Broadening is a problem in metal poor stars (Sgr dSph) as they have weaker lines and wide lines have more noise, which causes problems with S/N.

Results

From the linelists there are 54 Fe I lines, 3 Fe II , 3 Ti I , 3 Si I and 9 Ca I lines, but it not always possible to measure this many lines. Table 2.3 show the typical number of lines that could be measured for the stars in the Sgr dSph and Galactic Bulge stars.

Table 2.3: The number of Fe I, Fe II, Ca I, Si I and Ti I lines measured for Sgr dSph and Galactic Bulge stars.

	Fe I lines	Fe II lines	Ca I lines	Si I lines	Ti I lines
Sgr dSph	26	2–3	6–9	1–2	1–3
Bulge	32	2–3	7–9	1–2	2–3

2.4.3 Iron abundance determination

The MOOG software was used in order to determine the chemical abundances. MOOG is a FORTRAN-base code that performs a spectral line analysis and spectrum synthesis assuming local thermal equilibrium. Once the data has been processed using MOOG, metallicity histograms and abundance trends are produced. In order to determine the abundances for each star, a parameter file is created for each star and this is loaded into MOOG. The parameter file used in MOOG contains a linelist of EW measurements, the name of an output file and an initial model atmosphere file. The model atmospheres used in calculating the abundances are based on the stellar atmosphere models by Kurucz (Castelli & Kurucz 2004) . The model atmosphere has four primary input parameters, which can used to describe a stars'; effective temperature ($T_{\rm eff}$), surface gravity (log(g)), metallicity ([Fe/H]), and microturbulence (υ_t). The final values for the model atmosphere parameters are determined via an iterative process described below. Table 2.4 shows the final values for the model atmosphere for used for abundance calculations, for the Sgr dSph stars.

Table 2.4: The model atmospheres for Sgr dSph stars. For detail of MWZ ID see McDonald et al. (2012)

MWZ ID	Star ID	Right ascension (J2000)	Declination (J2000)	Temp (K)	log g (dex)	[Fe/H] (dex)	Vt (km s^{-1})
813	P5093	$18^h\ 59^m\ 21.10^s$	–30° 55′ 23.16″	4000	0.50	–1.31	2.40
491	P2924	$18^h\ 54^m\ 55.33^s$	–30° 48′ 38.38″	4300	1.80	–0.52	1.89
18	P3672	$18^h\ 57^m\ 41.12^s$	–30° 45′ 30.45″	4120	0.70	–0.82	2.30
583	P3127	$18^h\ 53^m\ 22.25^s$	–30° 46′ 06.29″	4050	0.70	–0.84	2.50
599	P3185	$18^h\ 53^m\ 22.25^s$	–30° 46′ 06.29″	4225	1.10	–0.86	2.25
730	P4198	$18^h\ 58^m\ 43.80^s$	–30° 36′ 46.96″	4050	1.78	–0.47	2.14
392	P2778	$18^h\ 54^m\ 04.97^s$	–30° 36′ 02.93″	4075	0.75	–0.64	2.00
527	P2994	$18^h\ 53^m\ 25.54^s$	–30° 35′ 24.76″	4450	1.00	–0.95	1.60
618	P3222	$18^h\ 53^m\ 44.32^s$	–30° 51′ 53.87″	4500	2.80	–0.50	2.10
890	P5890	$18^h\ 59^m\ 38.96^s$	–31° 11′ 34.80″	4500	2.00	–0.61	2.70
707	P3928	$18^h\ 58^m\ 20.11^s$	–30° 37′ 58.65″	4550	3.13	–0.50	1.80
792	P4834	$18^h\ 58^m\ 49.06^s$	–31° 00′ 27.18″	4500	1.58	–0.79	2.20
405	P2796	$18^h\ 54^m\ 02.14^s$	–30° 36′ 21.85″	4350	2.40	–0.48	2.35
776	P4607	$18^h\ 59^m\ 03.37^s$	–30° 46′ 52.11″	4350	2.53	–0.85	3.00
579	P3120	$18^h\ 56^m\ 57.09^s$	–30° 36′ 36.78″	4350	2.40	–0.71	3.30
556	P3047	$18^h\ 53^m\ 45.22^s$	–30° 45′ 14.49″	4600	2.40	–0.57	2.50
437	P2844	$18^h\ 56^m\ 22.30^s$	–30° 30′ 42.80″	4550	2.90	–0.36	2.70
888	P5876	$18^h\ 58^m\ 35.55^s$	–31° 25′ 43.85″	4750	3.50	–0.72	1.60
825	P5226	$18^h\ 59^m\ 04.08^s$	–31° 05′ 54.21″	4525	2.45	–0.52	2.62
378	P2758	$18^h\ 55^m\ 41.60^s$	–30° 17′ 45.10″	4475	2.05	–1.23	2.61
496	P2933	$18^h\ 54^m\ 19.65^s$	–30° 46′ 43.15″	4500	2.41	–1.21	2.38
771	P4539	$18^h\ 59^m\ 05.76^s$	–30° 41′ 05.89″	4450	2.10	–0.98	2.15
879	P5764	$18^h\ 59^m\ 27.06^s$	–31° 12′ 22.65″	4425	2.42	–1.12	1.85
403	P2794	$18^h\ 55^m\ 15.28^s$	–30° 13′ 55.68″	4250	2.68	–1.17	2.20
539	P3015	$18^h\ 54^m\ 42.88^s$	–30° 50′ 55.68″	4200	0.50	–1.23	2.30
676	P3703	$18^h\ 57^m\ 44.69^s$	–30° 45′ 06.09″	4250	1.12	–1.30	2.30
677	P3707	$18^h\ 57^m\ 51.63^s$	–30° 41′ 39.89″	4300	2.43	–1.03	2.40

Figure 2.10 shows an example of abundance output from equivalent width matching, when MOOG is run using the initial parameter file. The top panel (influenced by temperature) shows the Fe I abundances from individual lines plotted as function of excitation, reduced equivalent width (middle panel, this is influenced by microturbulence) [2] and wavelength (bottom panel, this is not influenced by the atmospheric parameters but gives an indication of the accuracy of the EW measurements). An iterative process is needed to derive the stellar atmosphere parameters because their

[2] The reduced equivalent width is the equivalent width divided by the wavelength of the line at which the width was measured.

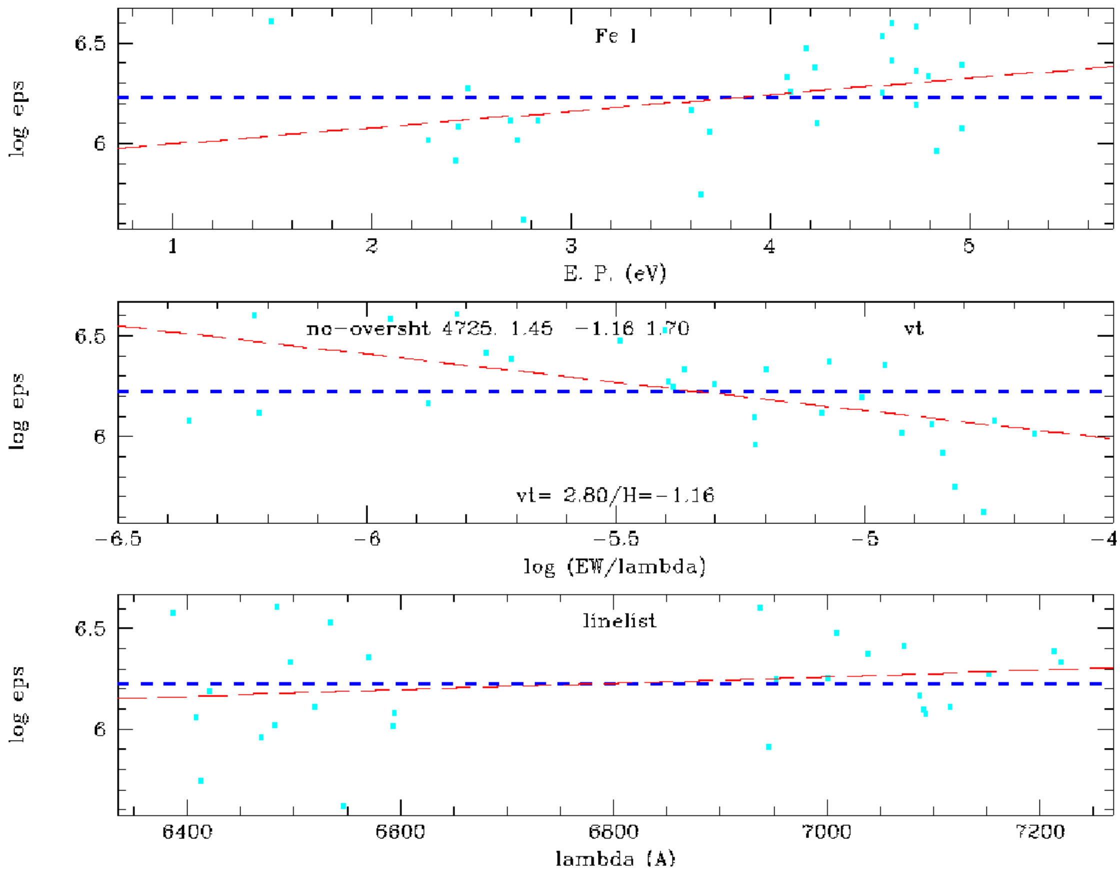

Figure 2.10: Example of abundance output from equivalent width matching, theses are: In the top panel, Fe I abundances from individual lines plotted as functions of excitation and in the middle and bottom panels, reduced equivalent width and wavelength. The dashed blue lines represent the mean Fe I abundance, while the dashed red lines represent (linear) trends of abundance with the three variables. The middle plot also contains details about the stellar model atmosphere used in this analysis. The bottom plot has information on the stellar equivalent widths. The vertical axis abundance units are logarithmic number densities on a standard scale, in which log ϵ (H) = 12. It is possible to adjust the microturbulent velocity while MOOG is running.

effects on the EW are correlated. In the iteration process, the four primary model atmosphere input parameters are adjusted. Initially the microturbulence is adjusted and this is followed by the effective temperature. Each time this happens a new model atmosphere file is created with revised [Fe/H]. After fixing the microturbulence and temperature, which ensures that the top two plots are flat (figure 2.10). The surface gravity can then be determined. The log (g) is adjusted until the Fe abundance derived from Fe I and Fe II are equal and the process is iterated. The Fe I and Fe II should be equal as they are ionization states of the same element.

Figure 2.11 shows the result when the model atmosphere input parameters have been optimized, converging to a unique solution for each star.

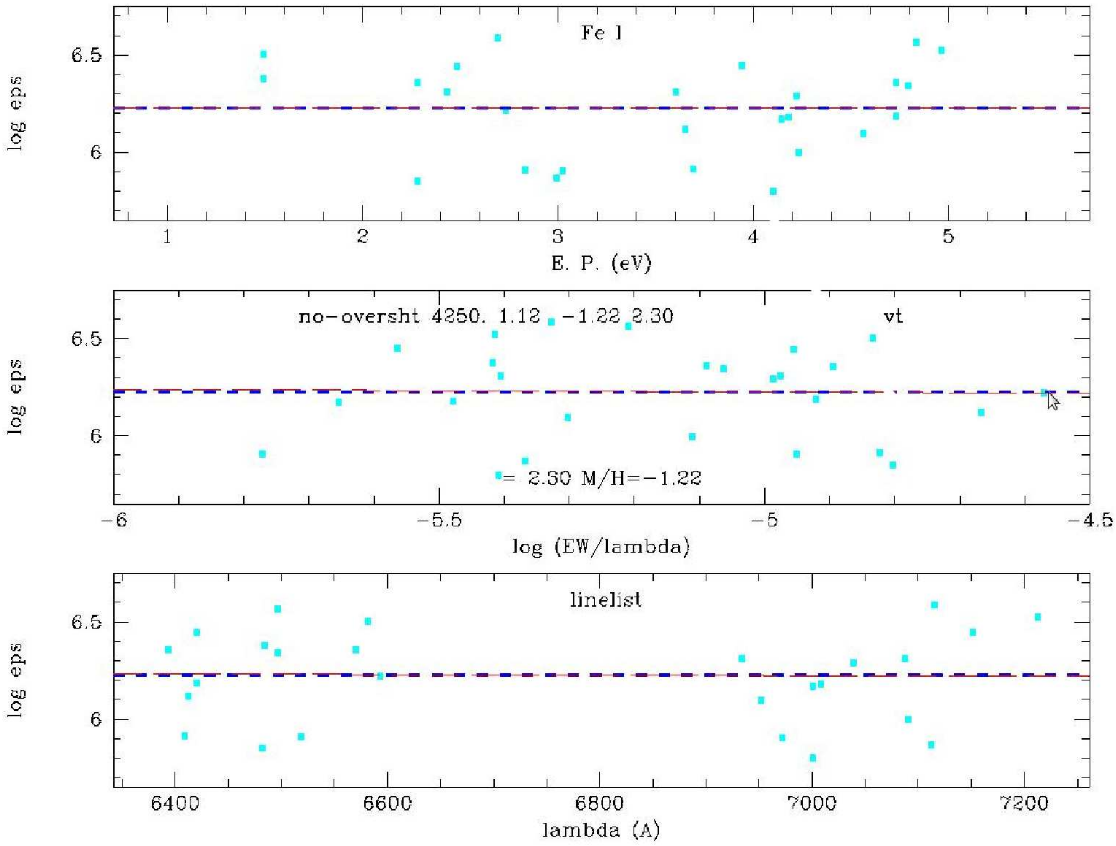

Figure 2.11: The final abundance output, after the model atmosphere input parameters have been optimized.

2.4.4 Error analysis

To calculate the errors in Fe I , Fe II , Ca, Si and Ti the following equation was used

$$\chi_{FeI} = \frac{\sigma_{FeI}}{\sqrt{N}} \tag{2.3}$$

χ_{FeI} is error in Fe I and N is the number of lines measured for Fe I ,Fe II , Ca, Si and Ti in the EW measurements and σ_{FeI} is the standard deviation. To work out σ[Si/Fe], σ[Ca/Fe] and σ[Ti/Fe] the following equation is used:

$$\sigma[\mathrm{Si/Fe}] = \sqrt{(\sigma[\mathrm{Fe/H})^2 + (\sigma[\mathrm{Si/H}])^2} \tag{2.4}$$

and the error in $\sigma[\alpha/\mathrm{H}]$ was calculated using the following equation:

$$\sigma[\alpha/\mathrm{H}] = \sqrt{\sigma[Ca/H])^2 + (\sigma[Si/H])^2 + (\sigma[Ti/H])^2} \tag{2.5}$$

and then the error in $\sigma[\alpha/\mathrm{Fe}]$ is then calculated using the following equation:

$$\sigma[\alpha/\mathrm{Fe}] = \sqrt{(\sigma[\alpha/\mathrm{H}])^2 + ([\mathrm{Fe/H}])^2} \tag{2.6}$$

The error analysis which has been carried out is only a statistical error and this is caused by a scatter between the EWs and the models. The error analysis does not cover any uncertainties in setting the model parameters.

2.4.5 Abundance uncertainties caused by model atmosphere parameter uncertainties

In order to estimate the sensitivity of the abundances to the adopted model atmospheres parameters, each of the parameters was changed, while the others were kept constant and the change in abundances recorded. P4607 was selected as Sgr dSph star with typical properties (T_{eff}, S/N, [Fe/H]). The initial model atmosphere parameters used for P4607, were T_{eff} = 4350 K, log(g) = 2.53 dex, [Fe/H] = –0.81 dex and υ_t = 3.00 km s^{-1}. They were changed by the following amounts, T_{eff} = ± 100 K, log(g) = ± 0.6 dex, [Fe/H] = ± 0.15 dex and υ_t = 0.35 km s^{-1}, chosen to match the scatter of these parameters in stars with otherwise similar properties. This avoided additional errors due to the inter-dependences among the parameters. The abundance uncertainty due to the parameters, σ_{atm} was calculated using:

$$\sigma^2_{\rm atm} = \sigma^2_{\rm Teff} + \sigma^2_{\rm log(g)} + \sigma^2_{\rm [Fe/H]} + \sigma^2_{\upsilon_{\rm t}} \tag{2.7}$$

where $\sigma_{\rm Teff}$, $\sigma_{\rm log(g)}$, $\sigma_{\rm [Fe/H]}$ and $\sigma_{\upsilon_{\rm t}}$ represent the change in derived abundance caused by changing the effective temperature, surface gravity, metallicity and micro-turbulent velocity of the stellar atmosphere model by the above amounts. The total error ($\sigma^2_{\rm tot}$) was obtained by adding the errors due to the model atmospheres parameters, $\sigma^2_{\rm atm}$ to the observational errors, $\sigma^2_{\rm obs}$ which are listed in table 3.3:

$$\sigma^2_{\rm tot} = \sigma^2_{\rm atm} + \sigma^2_{\rm obs} \tag{2.8}$$

The parameter which has the most influence seems to be the effective temperature, as it has an impact on the Fe I, Fe II, Ca, Ti and Si abundances. The surface gravity and the metallicity mainly affect the ionisation balance state of Fe, since Fe II and singly ionised transition metals are more reliant on electron pressure which is affected by metallicity and the surface gravity. The micro-turbulence had small

Table 2.5: The abundance sensitivity to model atmosphere parameters.

Abundances	T_{eff} $\pm$100K	log(g) $\pm$ 0.60 dex	[Fe/H] $\pm$0.15 dex	υ_t $\pm$0.35 kms^{-1}	σ_{atm} (dex)	σ_{obs} (dex)	σ_{tot} dex
[Fe/H]I	$\pm$0.02	$\pm$0.13	$\mp$ 0.04	$\mp$0.07	0.15	0.05	0.16
[Fe/H]II	$\mp$0.15	$\pm$0.35	$\mp$0.06	$\pm$0.03	0.39	0.13	0.41
[Si/H]	$\mp$0.08	$\pm$0.16	$\pm$0.04	$\mp$0.01	0.18	0.05	0.19
[Ca/H]	$\pm$0.13	$\mp$0.04	$\mp$0.00	$\mp$0.12	0.17	0.20	0.27
[Ti/H]	$\pm$0.15	$\pm$0.02	$\pm$0.00	$\mp$0.07	0.18	0.20	0.25

effects on Si, Fe I, Fe II, but greater influence on Ca and Ti. Table 2.5 shows the abundance sensitivity to the model atmosphere parameters.

Chapter 3

The alpha element abundances

3.1 Introduction

Detailed understanding of the chemical compositions are key in helping to study the origin and evolution of stellar populations, since they carry characteristic signatures of the objects that enrich the interstellar gas. Since abundance ratios are sensitive to the time scales of star formation and the initial mass function, this may reveal the relationship between different stellar groups, since different elements are synthesized by different stars and processes (Ryde et al. 2010).

The α elements O, Mg, Si, Ca and Ti don't have the same nucleosynthetic origin and in the case of Si, Ca and Ti they are mostly produced during SNII explosions, these elements have strong lines in the spectra which have been analysed in this project. These elements are also produced in large quantities by high mass AGB stars, hence the α abundance measurements are measure of the amount of enrichment of the proto-stellar cloud by the ejecta of stars that have undergone Type II supernovae.

3.1.1 Ca, Si and Ti abundance determination

Ca, Si and Ti were selected for measurement because strong lines are needed in the wavelength range in which the analysis is being carried out. The method used to determine the abundance of Fe and EW (section 2.4.3) is also used to determine the abundance of Ca, Si and Ti. Table 3.1 shows the atomic linelist used for Ca I, Ti I, and Si I.

Table 3.1: The atomic linelist used for finding equivalent width of Ca I, Ti I and Si I.

Wavelength (Å)	Ionization State	Excitation Potential (eV)	log gf (dex)
6395.47	Ti I	1.50	–2.540
6439.07	Ca I	2.53	0.010
6449.81	Ca I	2.52	–0.772
6455.60	Ca I	2.52	–1.460
6471.66	Ca I	2.53	–0.806
6493.78	Ca I	2.52	–0.389
6499.65	Ca I	2.52	–0.958
6554.23	Ti I	1.44	–1.150
6556.07	Ti I	1.46	–1.060
6572.78	Ca I	0.00	–3.950
7017.29	Si I	5.87	–1.750
7017.65	Si I	5.87	–1.212
7148.15	Ca I	2.71	0.007
7202.20	Ca I	2.71	–0.422

3.1.2 The results of [X/H] for Sgr dSph

The values of Si, Ca, Ti and Fe used in calculating the [X/H] ratios are shown in appendix A and the mean values for [X/H] are shown in table 3.2. There were a number of issues which affected the task of measuring the lines and subsequently the abundance measurements, this included the following:

1. The low number of lines that could be measured for each star. In the case of Si it was typically possible to measure 1-2 lines, for Ti 2-3 lines and for Ca 6-9 lines, table 3.3 shows the number lines that could measured. They [Si/Fe]

determination gave the least amount of scatter when compared to the Ca and Ti results (table 3.4).

2. The low S/N in the Sgr dSph data (table 3.5) made the task of calculating the EW difficult.

3. When determining the EW of the Ca lines, far greater amount of de-blending was required when compared to the Si and Ti lines.

Stars which are Fe poor are also poor in the α elements (Ca, Si and Ti). The correlation between [Ca, Si, Ti/H] and [Fe/H] is shown in figures 3.1 – 3.3. In figure 3.1 there is a correlation (Pearson correlation co-efficient, $R^2 = 0.76$) but there is scatter in the data, which is mostly due to the low number of lines (1–2 lines, table 3.3) that could measured and S/N issues (section 2.4.2). Table 3.3 shows the [X/H] (where X = Fe or Si or Ca or Ti) results and table 3.4 shows the [X/Fe] (where X = Ca or Ti or Si or α) results along with the number of lines that could be measured for each element. In the case when there is just one spectral line, the statistical uncertainty was calculated by taking the average of the statistical uncertainties for the other stars and multiplying this by $\sqrt{N}$, where N is the number of lines. [Si/Fe], [Ca/Fe] and [Ti/Fe] were averaged to produce a single [α/Fe] ratio.

Figure 3.2 shows the plot of [Ca/H] vs [Fe/H]. There is a correlation but not as strong ($R^2 = 0.57$), [Si/H] vs [Fe/H] as there is much more scatter, which is due to the difficulties in measuring the EW of the spectral lines. Even though it was possible to measure up to 7-9 lines, the Ca lines were highly blended and required a considerable amount of de-blending in order to measure the EW. This additional uncertainty probably provides most of the variation in the [Ca/H] abundances. Figure 3.3 shows the plot of [Ti/H] vs [Fe/H]. In this plot there is less correlation ($R^2 = 0.56$) when compared to the Ca and Si and this is partially due to the number lines that could be measured (1-3 lines). Figures 3.1 – 3.3 show that Si, Ca and Ti track each other but the amounts of scatter varies, with Ca and Ti having the greater amount of scattering.

Table 3.2: Mean values for [X/H] and[X/Fe] for Sgr dSph Stars.

X	[X/H]	[X/Fe]
Fe	–0.82±0.05	
Si	–0.59±0.28	0.23±0.40
Ca	–0.85±0.25	–0.02±0.37
Ti	–0.40±0.22	0.38±0.0.36
α		0.20±0.30

The metallicity spread [Fe/H] in the the Sgr dSph was found to be –1.305 to –0.355 dex. This spread was lower than the results achieved by Bellazzini, Ferraro & Buonanno (1999b) and Layden & Sarajedini (2000), who found the spread to be –2.0 $\lesssim$ [Fe/H] $\lesssim$ –0.7, which came from analysis of the spectra of 14 red giants. Bellazzini, Ferraro & Buonanno (1999b) concluded that 80–90 % of Sgr stars are metal-poor, [Fe/H] < –1. The results in this project are in agreement Smecker-Hane & McWilliam (2002), who found metallicities ranging from –1.6 $\leqslant$ [Fe/H] $\leqslant$ –0.05 . This is confirmed by the results achieved in this project (table 3.2 and 3.3), where 30 % of the stars show [Fe/H] > –1 and 70% of the stars have, [Fe/H] < –1, so bulk of the stars in this projects have been found to be metal poor. The discrepancy between results achieved by Bellazzini, Ferraro & Buonanno (1999b) and Smecker-Hane & McWilliam (2002) is understandable since the degeneracy of age and metallicity in colour magnitude diagrams. The derived ages of the stars in Smecker-Hane & McWilliam (2002) study varies from $\sim$ 0.5 to 15 Gyr and since many of the Sgr dSph stars are greatly younger than the globular clusters. This greatly reduces the age of the stars, which would have been inferred from higher metallicity (Smecker-Hane & McWilliam 2002).

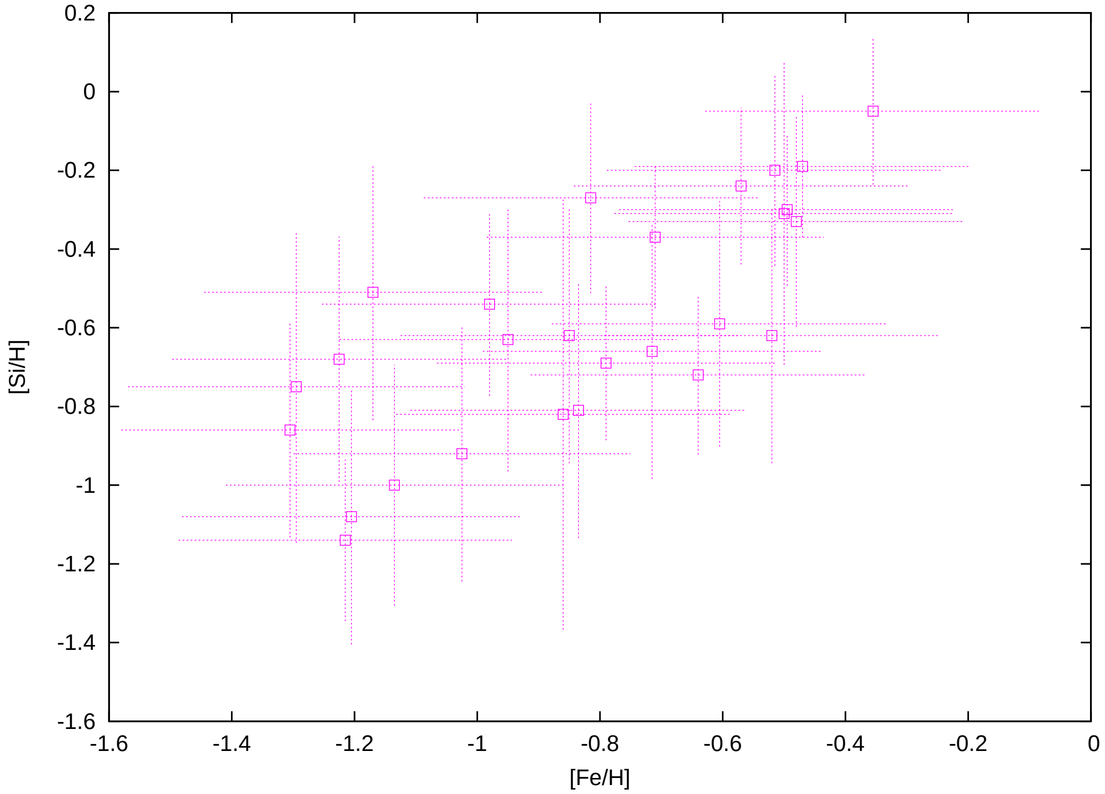

Figure 3.1: [Si/H] versus [Fe/H] for the Sgr dSph stars

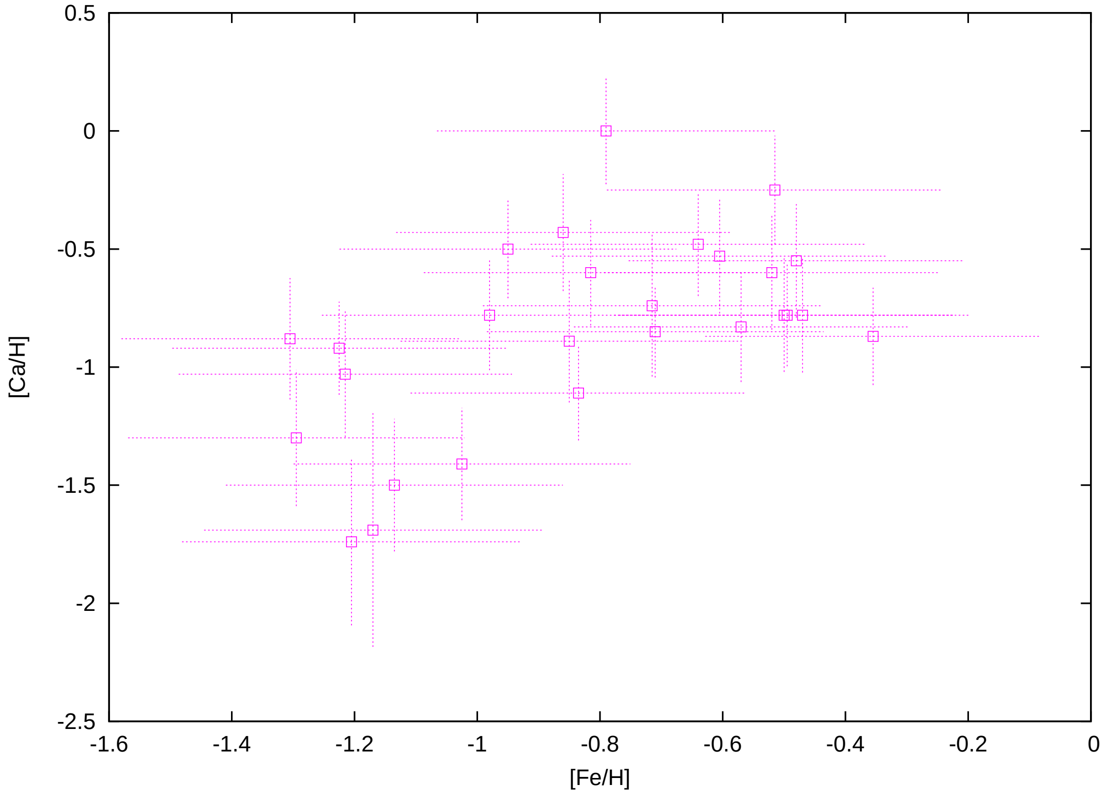

Figure 3.2: [Ca/H] versus [Fe/H] for the Sgr dSph stars

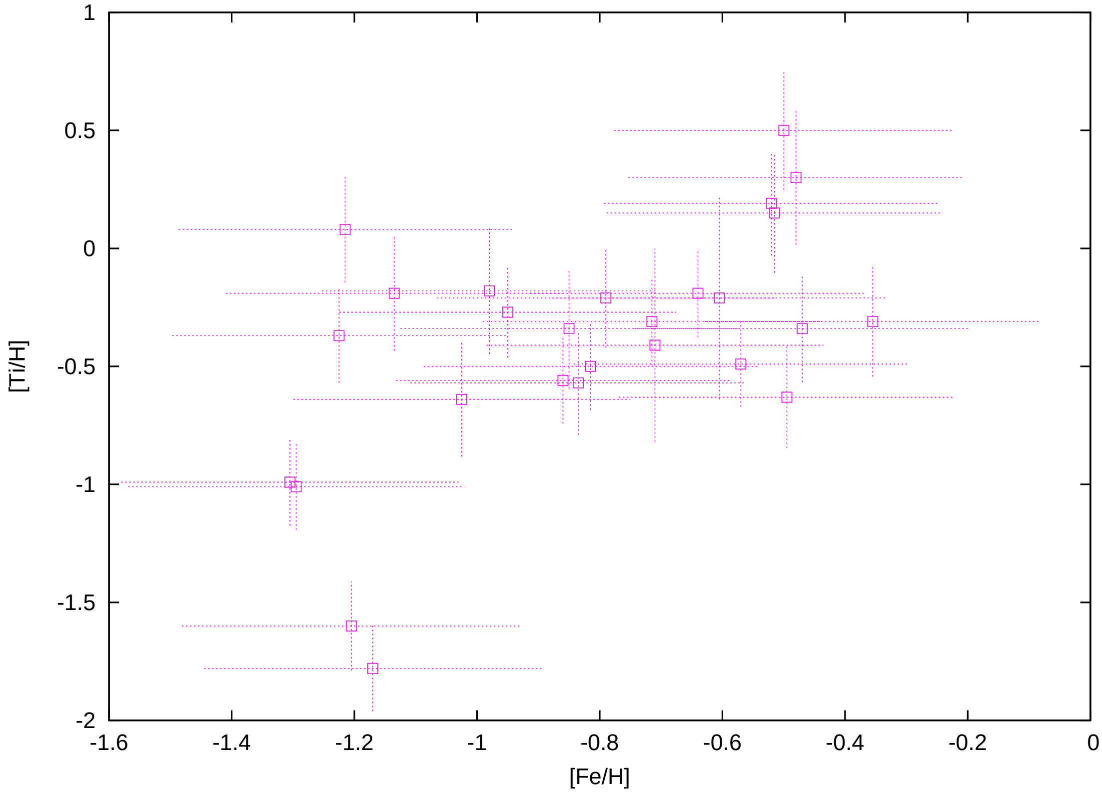

Figure 3.3: [Ti/H] versus [Fe/H] for the Sgr dSph stars

Table 3.3: The [Fe/H], [Si/H] and [Ti/H] results for Sgr dSph stars

StarID	[Fe/H]	No of lines	[Si/H]	No of lines	[Ca/H]	No of lines	[Ti/H]	No of lines
P5093	−1.31±0.28	21	−0.86±0.27	2	−0.88±0.26	7	−0.99±0.18	3
P2924	−0.52±0.27	28	−0.20±0.24	2	−0.25±0.23	8	0.15±0.25	2
P3672	−0.82±0.27	26	−0.27±0.24	2	−0.60±0.22	8	−0.50±0.18	3
P3127	−0.84±0.27	35	−0.81±0.27	1	−1.11±0.20	8	−0.57±0.22	3
P3185	−0.86±0.27	35	−0.82±0.55	2	−0.43±0.25	8	−0.56±0.18	2
P4198	−0.47±0.27	31	−0.19±0.18	2	−0.78±0.24	8	−0.34±0.23	3
P2778	−0.64±0.27	33	−0.72±0.20	2	−0.48±0.22	8	−0.19±0.19	2
P2994	−0.95±0.27	30	−0.63±0.34	2	−0.50±0.21	8	−0.27±0.19	3
P3222	−0.50±0.27	26	−0.30±0.19	2	−0.78±0.22	8	−0.63±0.22	2
P5890	−0.61±0.27	27	−0.59±0.31	2	−0.53±0.24	8	−0.21±0.43	2
P3928	−0.50±0.28	19	−0.31±0.38	2	−0.78±0.24	8	0.50±0.25	2
P4834	−0.79±0.28	27	−0.69±0.20	2	0.00±0.23	8	−0.21±0.21	3
P2796	−0.48±0.27	33	−0.33±0.27	2	−0.55±0.24	7	0.30±0.28	2
P4607	−0.85±0.27	27	−0.62±0.27	1	−0.89±0.26	9	−0.34±0.25	3
P3120	−0.71±0.27	26	−0.37±0.18	2	−0.85±0.19	9	−0.41±0.41	2
P3047	−0.57±0.27	30	−0.24±0.20	2	−0.83±0.23	8	−0.49±0.18	3
P2844	−0.36±0.27	19	−0.05±0.19	2	−0.87±0.21	8	−0.31±0.23	2
P5876	−0.72±0.28	21	−0.66±0.27	1	−0.74±0.30	8	−0.31±0.18	2
P5226	−0.52±0.27	30	−0.62±0.27	1	−0.60±0.24	6	0.19±0.22	3
P2758	−1.23±0.27	32	−0.68±0.31	2	−0.92±0.20	9	−0.37±0.20	2
P2933	−1.21±0.28	22	−1.08±0.27	1	−1.74±0.35	7	−1.63±0.19	2
P4539	−0.98±0.27	29	−0.54±0.23	2	−0.78±0.23	8	−0.18±0.27	2
P5764	−1.12±0.27	23	−1.00±0.31	2	−1.50±0.28	9	−0.19±0.24	2
P2794	−1.17±0.28	19	−0.51±0.23	1	−1.69±0.50	7	−1.78±0.18	2
P3015	−1.23±0.27	22	−1.14±0.21	2	−1.03±0.27	8	0.08±0.22	3
P3703	−1.30±0.27	26	−0.75±0.40	2	−1.30±0.29	8	−1.01±0.18	2
P3707	−1.03±0.27	22	−0.92±0.27	1	−1.41±0.24	9	−0.64±0.24	3

Table 3.4: The [Si/Fe], [Ca/Fe], [Ti/Fe] and [α/Fe] results for Sgr dSph stars

Star ID	[Si/Fe]	[Ca/Fe]	[Ti/Fe]	[α/Fe]
P5093	0.45±0.39	0.43±0.38	0.29±0.33	0.39±0.30
P2924	0.32±0.37	0.27±0.36	0.46±0.37	0.39±0.30
P3672	0.55±0.36	0.22±0.35	0.27±0.33	0.34±0.30
P3127	0.03±0.42	–0.28±0.34	0.24±0.35	0.00±0.31
P3185	0.04±0.61	0.43±0.37	0.26±0.33	0.24±0.30
P4197	0.28±0.33	–0.31±0.37	0.09±0.36	0.02±0.30
P2778	–0.08±0.34	0.16±0.35	0.40±0.33	0.16±0.30
P2994	0.32±0.43	0.45±0.34	0.65±0.34	0.47±0.30
P3222	0.20±0.34	–0.29±0.35	–0.18±0.35	–0.09±0.31
P5890	0.02±0.41	0.08±0.37	0.36±0.43	0.15±0.30
P3928	0.19±0.47	–0.28±0.37	0.95±0.37	0.29±0.30
P4834	0.10±0.34	0.79±0.36	0.54±0.35	0.48±0.30
P2796	0.15±0.38	–0.07±0.36	0.75±0.39	0.28±0.31
P4607	0.23±0.43	-0.04±0.38	0.48±0.37	0.22±0.30
P3120	0.34±0.33	–0.14±0.34	0.27±0.49	0.16±0.30
P3047	0.33±0.34	–0.26±0.36	0.03±0.33	0.03±0.30
P2844	0.31±0.33	–0.52±0.34	0.02±0.36	–0.06±0.30
P5876	0.06±0.43	–0.03±0.41	0.38±0.33	0.14±0.30
P5226	-0.10±0.42	–0.08±0.36	0.67±0.35	0.16±0.31
P2758	0.55±0.41	0.31±0.34	0.81±0.34	0.55±0.30
P2933	0.13±0.43	–0.54±0.45	–0.43±0.33	–0.28±0.30
P4539	0.44±0.36	0.20±0.36	0.76±0.38	0.47±0.31
P5764	0.14±0.41	–0.37±0.39	0.91±0.37	0.23±0.30
P2794	0.66±0.43	0.52±0.57	–0.65±0.33	–0.17±0.30
P3015	0.08±0.34	0.19±0.38	1.24±0.35	0.50±0.31
P3703	0.55±0.48	–0.01±0.40	0.24±0.33	0.26±0.31
P3707	0.11±0.42	–0.39±0.36	0.34±0.37	0.02±0.30

Table 3.5: The S/N for the Sgr dSph stars for 6931-7246$\AA$ and 6381-6624$\AA$ part of the spectrum.

MWZ ID	Star ID	S/N for 6931-7246Å	S/N 6381-6624Å
813	P5093	27.8	60.7
491	P2924	26.7	67.6
18	P3672	27.9	60.0
583	P3127	25.5	58.3
599	P3185	26.4	61.2
730	P4198	27.2	58.4
392	P2778	30.0	68.4
527	P2994	23.8	58.7
618	P3222	21.8	49.0
890	P5890	24.5	51.9
707	P3928	23.9	53.2
792	P4834	21.7	48.2
405	P2796	24.7	62.1
776	P4607	23.9	54.4
579	P3120	20.5	52.9
556	P3047	23.0	56.3
437	P2844	20.9	57.2
888	P5876	18.0	43.2
825	P5226	22.6	48.4
378	P2758	17.8	46.1
496	P2933	19.2	47.2
771	P4539	23.5	50.0
879	P5764	17.5	37.6
403	P2794	21.7	50.4
539	P3015	20.7	51.4
676	P3703	21.0	44.7
677	P3707	22.3	47.2

Chapter 4

The Galactic Bulge Stars

4.1 Introduction

The Bulge stars were analysed as this would allow a comparison to be made with the Sgr dSph stars. For the Bulge stars the chemical abundances of Fe, Si, Ti and Ca for a sample of 27 stars (from the same field as the Sgr dSph stars) were calculated, using the same methods which were used to calculate the EW and chemical abundances for the Sgr dSph stars (see 2.4.2 and 2.4.3). This study of the Bulge stars, which were observed at latitudes b= -13^o, are among the furthest from the Galactic centre ever undertaken. Hence, the population we are studying is the kinematically 'hottest', outer region of the Bulge. This often corresponds to the oldest, most metal-poor population in a system.

A sample size of 27 stars was chosen, to allow a comparison to be made with the Sgr dSph stars, as 27 stars were selected for analysis in that galaxy. However far more stars in the Bulge could have been analysed than the 27 selected, as the Bulge stars did not have the S/N issues which affected the Sgr dSph stars (table 3.5).

There are a number of differences between the Sgr dSph and Galactic Bulge stars, including:

1. The Bulge stars have higher S/N than the Sgr dSph stars (table 3.5).
2. The stars in the Bulge have a higher temperature. The average temperature of the stars selected was 4650K, this compared with the Sgr dSph stars which have a average temperature of 4353K.
3. There is greater broadening of the spectral lines of the Bulge stars, which is due to the stars having higher gravity.

4.2 Selection criteria

The selection criteria used are discussed in section 2.4.1. Visual inspection of spectra (figure 2.7) allowed separation of high gravity foreground dwarfs stars from the Bulge giants, allowing the Bulge giants to be selected for analysis. Foreground giants in the Galactic disc are not entirely removed, and remain a contaminant in the Bulge sample. The selection criteria is biased towards

1. Brighter targets in the Galactic foreground.
2. Warmer, metal-poor stars in the Galactic Bulge, that are brighter in the optical.
3. Warmer, metal poor stars due to our exclusion of M-type stars.

4.3 The results of [X/Fe] and [X/H] for Bulge

Table 4.1 shows the averages for each sequence and the final model atmosphere parameters of each star are shown in table 4.2 and the number of lines which could be measured for each element were a factor in how accurately the abundances could be determined. Table 4.3 shows the [X/H] (where X = Fe or Ca or Si or Ti) along with the number of lines that could be measured for each star and table 4.4 shows the [X/Fe] results. In the case of Ti and Si it is typically only possible to measure between 1-3 lines and in the case of Ca it possible to measure 7-9 lines. This resulted in greater accuracy in the Ca abundance compared to the Sgr dSph. In the case of Fe it was typically possible to measure between 16-46 lines. Table 4.5 shows the mean values of [X/Fe] and [X/H].

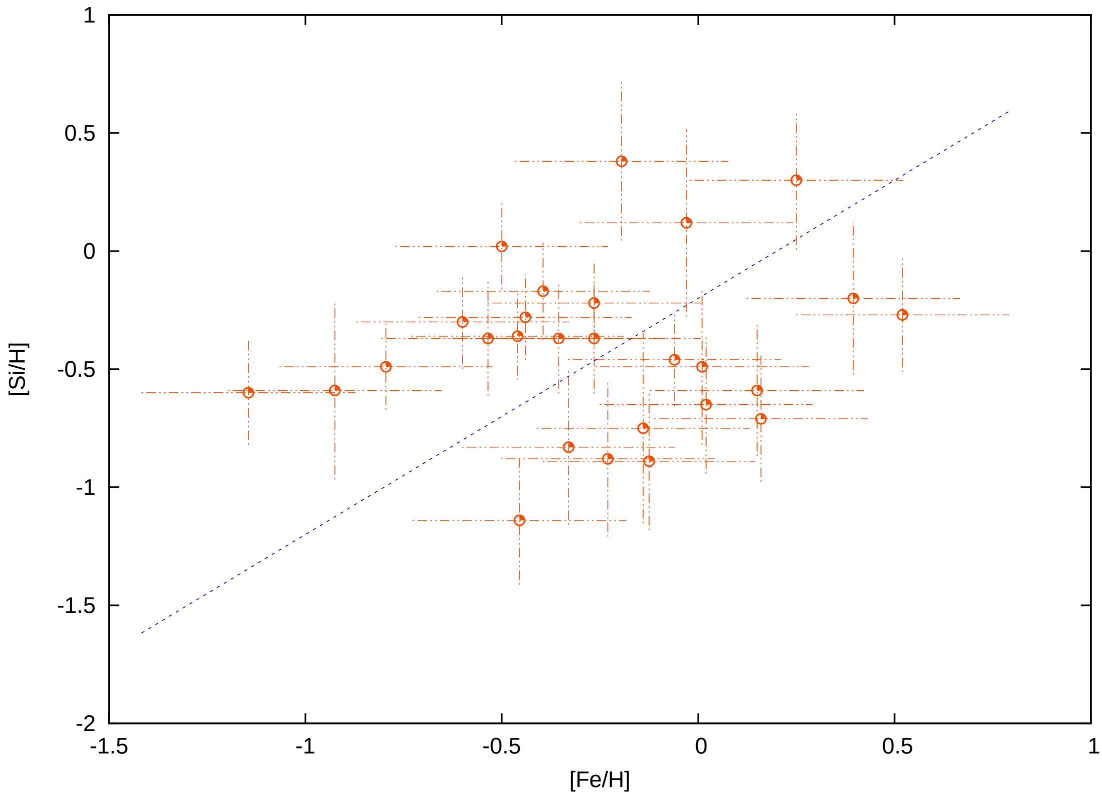

Figure 4.1: [Si/H] versus [Fe/H] for the Galactic Bulge stars.

Figures 4.1 – 4.3 show the [Si/H], [Ca/H], [Ti/H] versus [Fe/H]. The plots of [Ca/H] and [Ti/H] versus [Fe/H] both show strong correlation (R^2 for [Ca/H] = 0.84 and for [Ti/H] = 0.71) however the plot of [Si/H] versus [Fe/H] does not show the same

Table 4.1: The mean abundances of elements for Galactic Bulge stars.

Element	Si rich but metal poor	Si poor but metal rich
[α/Fe]	0.31±0.04	0.25±0.05
[Ti/Fe]	0.29±0.12	0.54±0.09
[Ca/Fe]	0.18±0.05	0.04±0.12
[Si/Fe]	0.27±0.05	0.18±0.06
[Fe/H]	0.43±0.11	0.07±0.07

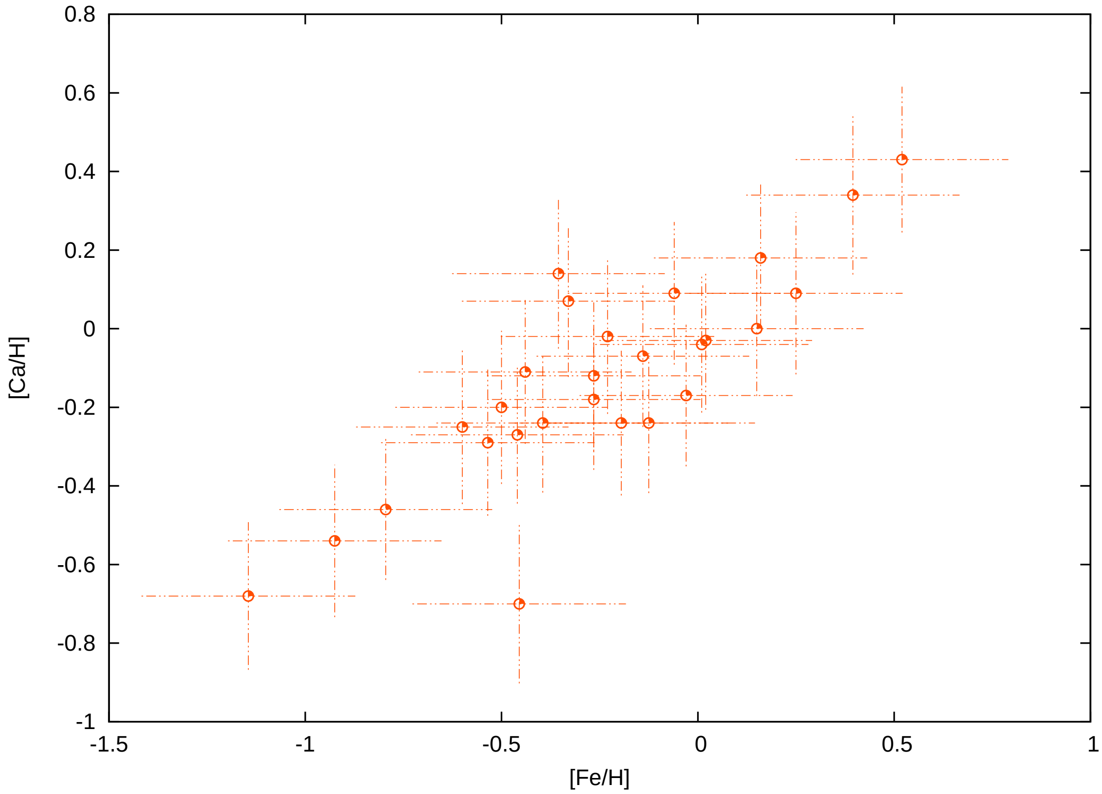

Figure 4.2: [Ca/H] versus [Fe/H] for the Galactic Bulge stars

strong correlation (R^2 for [Si/H] = 0.17). In the [Si/H] versus [Fe/H] plot (figure 4.1) there are two distinct sequences, the stars at the bottom right (Si poor but metal rich, table 4.1) of that plot show lower average value for [Si/H] = 0.18 dex than stars in the top left (Si rich but metal poor, table 4.1) of the plot, [Si/H]= 0.27 dex. The average abundance for stars on left side of [Si/H] plot (figure 4.1), are higher than those on the right side of plot, except for Ti. Part of the reason why these stars have lower average value for Si is that it was only possible to measure between 1-2 Si lines. For the Si lines which could be measured, the task of calculating the EW was very difficult, since these Si lines are narrow in width when compared to the

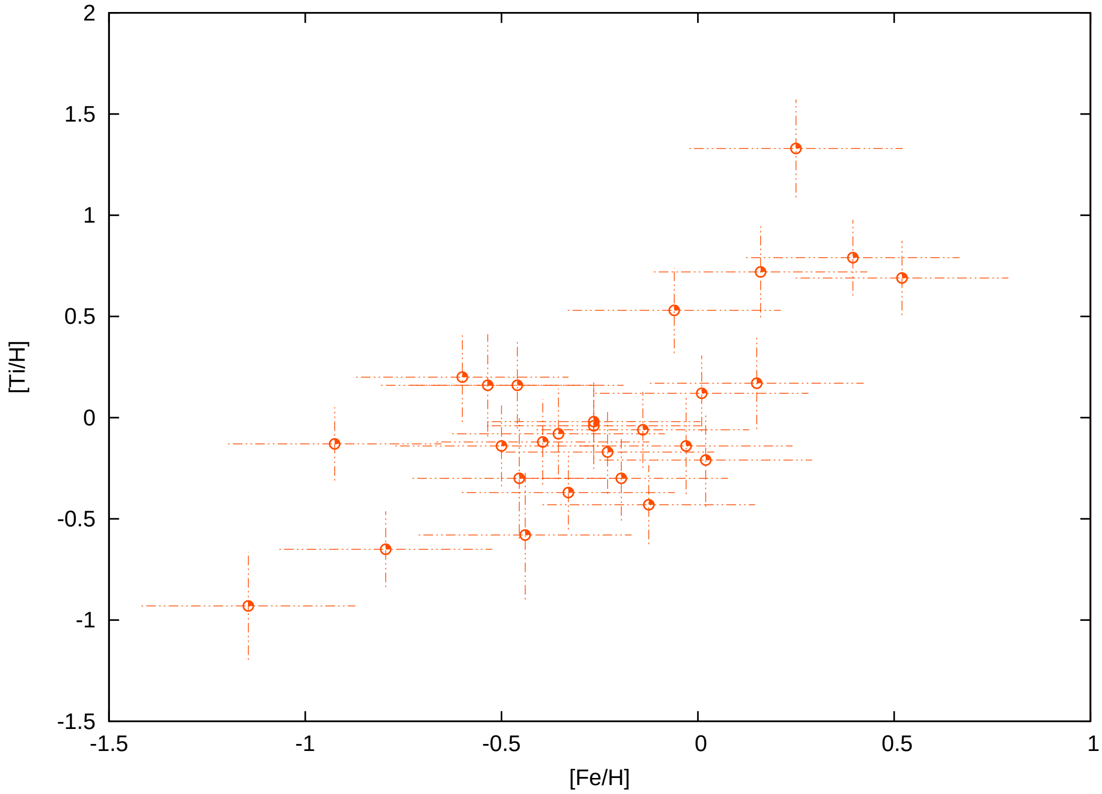

Figure 4.3: [Ti/H] versus [Fe/H] for the Galactic Bulge stars

Si lines in Sgr dSph stars. It remains unclear why there is difference and whether there is a observational bias or real effect.

The plot of [Ca/H] versus [Fe/H], figure 4.2 shows a strong correlation as it was possible to measure between 7-9 lines and the Ca lines required very little de-blending which helped improve the accuracy of abundance calculations. Star 00522 has a low [Ca/H] value compared to the other stars, it also has lower values for Si, Ca and Ti (table 4.3) when compared to the other stars on the plot. For this star it was difficult to measure the EW for the Ca, Si and Ti lines (due to the low S/N, table 4.6) and this is the main reason why the abundances measurements are low when compared to the other stars. Another factor which affected the abundance results for the some of the stars is the issues of setting the continuum (which is due to the low S/N), which results in either a over estimation or underestimation of the EW, which in turn affects the model atmospheres and hence the final abundance results (section 2.4.2).

Of the three alpha elements analysed, Ca shows the best defined trend and can be considered the most reliable of the alpha element abundances in this study. It is expected to be enriched exclusively by SNII explosions. Figure 4.4 shows the EW being measured for Si lines, 02983 is in Bulge and P2924 is in Sgr dSph. The Si lines in Bulge stars, are blended into the other lines, which makes measuring the EW very difficult. However in the case of Si lines in the Sgr dSph, there is less blending of the lines and the task measuring the EW is more accurate, even though the data lower S/N than the Bulge data.

In comparison measuring the Ca lines is easier in the Bulge stars, since there is very little blending of lines into each other. This shown in figure 4.5. Whereas, in the Sgr dSph stars, calculating the EW was difficult due to considerable blending of the lines (at lower temperatures the CN and Ca lines blind into each other more than at higher temperatures as the Bulge stars are higher in temperature than the Sgr dSph stars) and the low S/N, which made setting the continuum difficult. Since it was possible to measure a greater number of lines for Ca, the Ca abundances should be more accurate than the Si abundances.

Table 4.2: The model atmospheres for the Galactic Bulge Stars. For detail of MWZ ID see McDonald et al. (2012)

MWZ ID	Star ID	Right ascension (J2000)	Declination (J2000)	Temp (K)	log g (dex)	[Fe/H] (dex)	Vt (km s^{-1})
64	00956	$18^h\ 53^m\ 38.52^s$	–30° 12′ 08.87″	4850	2.70	0.02	1.55
134	02971	$18^h\ 58^m\ 10.60^s$	–30° 45′ 05.14″	5100	1.80	–0.91	1.80
23	00571	$18^h\ 53^m\ 36.30^s$	–30° 30′ 03.17″	5000	2.55	–0.22	1.50
30	00629	$18^h\ 55^m\ 59.24^s$	–30° 13′ 14.57″	4250	1.80	–0.46	1.70
90	01360	$18^h\ 53^m\ 24.20^s$	–30° 49′ 37.18″	4550	2.10	–0.12	1.75
45	00792	$18^h\ 53^m\ 58.23^s$	–30° 46′ 20.08″	4350	1.80	–0.51	1.83
30	06290	$18^h\ 56^m\ 33.84^s$	–30° 25′ 33.25″	4725	1.45	–1.15	1.70
117	02443	$18^h\ 57^m\ 52.34^s$	–30° 44′ 07.22″	4375	2.10	–0.59	1.80
162	03734	$18^h\ 58^m\ 48.91^s$	–30° 32′ 50.93″	4445	2.10	–0.03	1.60
107	01998	$18^h\ 57^m\ 38.75^s$	–30° 40′ 50.07″	4550	2.37	–0.13	1.55
5	00270	$18^h\ 55^m\ 24.90^s$	–30° 17′ 22.26″	4800	2.33	–0.45	1.55
219	07086	$18^h\ 57^m\ 51.75^s$	–31° 25′ 43.55″	4800	2.37	–0.19	1.70
253	08713	$18^h\ 58^m\ 50.11^s$	–31° 25′ 43.10″	4750	3.10	0.01	1.55
128	02810	$18^h\ 58^m\ 17.29^s$	–30° 35′ 54.79″	4750	3.65	0.25	1.70
99	01491	$18^h\ 52^m\ 55.59^s$	–30° 14′ 10.59″	4500	2.50	-0.06	1.65
2	00138	$18^h\ 55^m\ 18.97^s$	–30° 21′ 01.66″	4600	2.70	0.15	1.75
202	06068	$18^h\ 58^m\ 23.84^s$	–31° 13′ 45.11″	4600	1.28	–0.26	1.70
87	01295	$18^h\ 53^m\ 30.45^s$	–30° 49′ 57.07″	4500	2.36	0.53	1.60
195	05789	$18^h\ 58^m\ 12.94^s$	–31° 13′ 51.28″	4500	2.36	0.40	1.92
231	07750	$19^h\ 00^m\ 14.93^s$	–30° 51′ 46.90″	4525	2.54	0.16	2.00
20	00522	$18^h\ 53^m\ 40.40^s$	–30° 28′ 00.92″	4525	1.35	–0.45	1.75
86	01289	$18^h\ 53^m\ 34.33^s$	–30° 50′ 39.20″	4675	2.00	–0.80	1.73
114	02392	$18^h\ 57^m\ 35.25^s$	–30° 50′ 04.09″	4625	1.47	–0.36	1.33
78	01158	$18^h\ 53^m\ 54.90^s$	–30° 51′ 54.28″	4625	2.35	–0.39	1.52
135	02983	$18^h\ 52^m\ 05.14^s$	–30° 08′ 12.69″	4750	1.53	–0.33	1.35
150	03458	$18^h\ 58^m\ 36.25^s$	–30° 38′ 55.79″	5025	3.05	–0.54	1.60
153	03528	$18^h\ 58^m\ 15.47^s$	–30° 52′ 06.13″	4800	3.00	–0.27	1.46

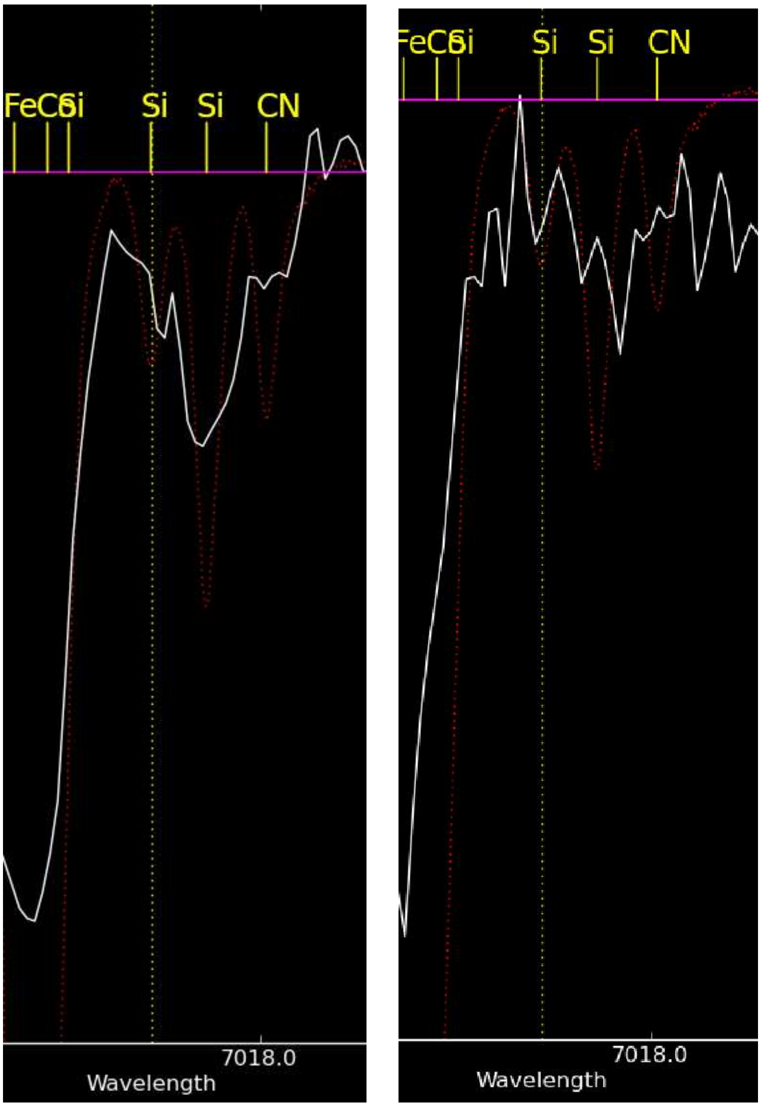

(a) 02983 (b) P2924

Figure 4.4: Only the highlighted Si line and one to the right are being measured in both cases. The leftmost Si line is not measured as it is too heavily blended with the strong neighbouring Fe line. a) Measuring the EW of Si line was difficult for the Bulge stars, due to the amount of blending of Si lines with each other and with neighbouring Fe line b) Measuring the EW of Si lines for Sgr dSph stars was easier than the Bulge as there is less blending of the lines.

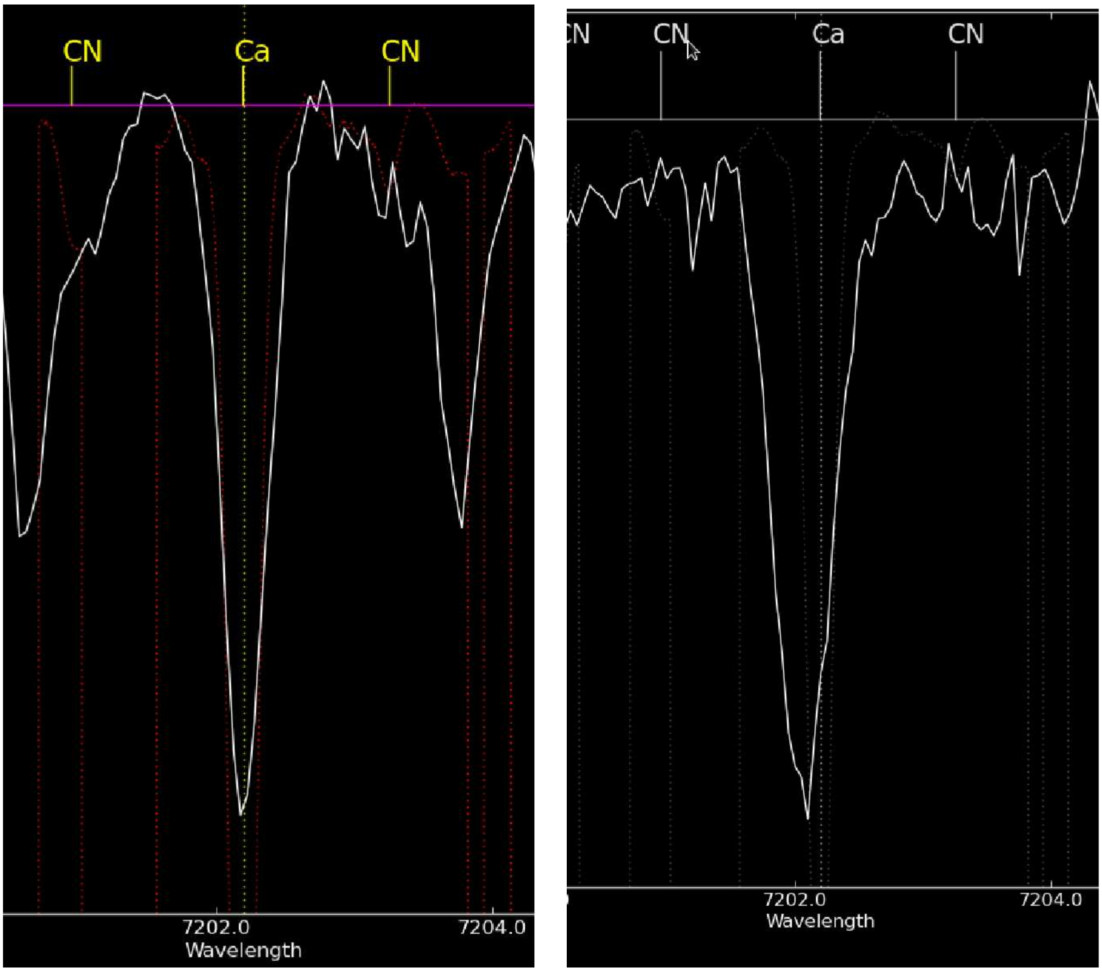

(a) 02983 (b) 2924

Figure 4.5: Comparing Ca lines in the Sgr dSph and Galactic Bulge. a) Measuring the EW of Ca line was less challenging for the Bulge stars as there less blending of the lines. b) Measuring the EW of Ca lines for Sgr dSph stars was difficult due to the low S/N and blending of the lines.

Table 4.3: The [Si/H], [Ca/H] and [Ti/H] Results for Galactic Bulge Stars

Star ID	[Fe/H]	No of lines	[Si/H]	No of lines	[Ca/H]	No of lines	[Ti/H]	No of lines
00956	0.02±0.27	38	–0.65±0.29	1	–0.03±0.18	8	–0.21±0.23	3
02971	–0.91±0.27	26	–0.59±0.38	2	–0.54±0.19	9	–0.31±0.18	2
00571	–0.22±0.27	23	–0.88±0.33	2	–0.02±0.20	8	–0.17±0.21	2
00629	–0.46±0.27	37	–0.36±0.19	2	–0.27±0.18	8	0.16±0.21	3
01360	–0.12±0.27	35	–0.89±0.29	1	–0.24±0.18	8	–0.43±0.20	3
00792	–0.51±0.27	39	0.02±0.18	2	–0.20±0.19	8	–0.14±0.20	3
06290	–1.15±0.27	28	–0.60±0.22	2	–0.68±0.19	7	–0.93±0.27	3
02443	–0.59±0.27	35	–0.30±0.20	2	–0.25±0.20	5	0.20±0.22	3
03734	–0.03±0.27	35	0.12±0.40	2	–0.17±0.18	8	–0.14±0.24	3
01998	–0.13±0.27	43	–0.75±0.40	2	–0.07±0.18	8	–0.06±0.19	2
00270	–0.45±0.27	46	–0.28±0.18	2	–0.11±0.18	8	–0.58±0.32	3
07086	–0.19±0.27	44	0.38±0.34	2	–0.24±0.18	8	–0.30±0.21	2
08713	0.01±0.27	34	–0.49±0.33	2	–0.04±0.17	8	0.12±0.19	2
02810	0.25±0.27	24	0.30±0.29	2	0.09±0.21	7	1.33±0.24	3
01491	–0.06±0.27	16	–0.46±0.20	2	0.09±0.18	8	0.53±0.21	3
00138	0.15±0.27	43	–0.59±0.28	2	0.00±0.17	8	0.17±0.23	3
06068	–0.26±0.27	25	–0.37±0.23	2	–0.12±0.19	8	–0.04±0.21	3
01295	0.53±0.27	23	–0.27±0.24	2	0.43±0.19	8	0.69±0.18	2
05789	0.40±0.27	22	–0.20±0.32	2	0.34±0.20	8	0.79±0.19	3
07750	0.16±0.27	26	–0.71±0.27	2	0.18±0.19	8	0.72±0.22	2
00522	–0.45±0.27	35	–1.14±0.27	2	–0.70±0.20	8	–0.30±0.30	3
01289	–0.80±0.27	36	–0.49±0.18	2	–0.46±0.18	7	–0.65±0.19	3
02392	–0.36±0.27	26	–0.37±0.23	2	0.14±0.19	8	–0.08±0.22	3
01158	–0.39±0.27	35	–0.17±0.21	2	–0.24±0.18	8	–0.12±0.21	3
02983	–0.33±0.27	34	–0.83±0.33	2	0.07±0.19	7	–0.37±0.18	2
03458	–0.54±0.27	29	–0.37±0.24	2	–0.29±0.19	7	0.16±0.25	2
03528	–0.27±0.27	31	–0.22±0.18	2	–0.18±0.18	8	0.02±0.18	3

Table 4.4: The [Si/Fe], [Ca/Fe], [Ti/Fe] and [α/Fe] Results for Galactic Bulge Stars

Star ID	[Si/Fe]	[Ca/Fe]	[Ti/Fe]	[α/Fe]
00956	–0.67±0.40	–0.05±0.32	–0.27±0.36	–0.33±0.30
02971	0.32±0.47	0.37±0.33	0.74±0.33	0.48±0.30
00571	–0.66±0.43	0.20±0.34	0.01±0.34	–0.15±0.30
00629	0.10±0.33	0.19±0.32	0.58±0.35	0.29±0.29
01360	–0.77±0.40	–0.12±0.32	–0.35±0.33	–0.41±0.30
00792	0.53±0.33	0.31±0.33	0.33±0.34	0.39±0.29
06290	0.55±0.35	0.47±0.33	0.18±0.38	0.40±0.30
02443	0.29±0.34	0.34±0.33	0.75±0.35	0.46±0.29
03734	0.15±0.48	–0.14±0.33	–0.15±0.36	–0.05±0.30
01998	–0.62±0.49	0.06±0.33	0.03±0.33	–0.18±0.30
00270	0.17±0.33	0.34±0.33	–0.17±0.42	0.11±0.30
07086	0.57±0.43	–0.05±0.33	–0.15±0.34	0.12±0.30
08713	–0.50±0.43	–0.05±0.32	0.07±0.33	–0.16±0.30
02810	0.05±0.40	–0.16±0.34	1.04±0.36	0.31±0.30
01491	–0.40±0.33	0.15±0.33	0.55±0.34	0.10±0.29
00138	–0.74±0.39	–0.15±0.32	–0.02±0.35	–0.30±0.30
06068	–0.11±0.36	0.14±0.33	0.18±0.35	–0.07±0.30
01295	–0.80±0.36	–0.10±0.33	0.12±0.33	–0.26±0.30
05789	–0.60±0.42	–0.06±0.34	0.35±0.33	–0.10±0.29
07750	–0.87±0.38	0.02±0.33	0.52±0.35	–0.11±0.30
00522	–0.69±0.39	–0.25±0.34	0.11±0.40	–0.28±0.30
01289	–0.31±0.33	0.34±0.33	0.11±0.33	0.25±0.29
02392	–0.01±0.36	0.50±0.33	0.24±0.35	0.24±0.29
01158	0.22±0.34	0.15±0.32	0.23±0.34	0.20±0.29
02983	–0.50±0.43	0.40±0.33	–0.08±0.33	–0.06±0.30
03458	0.17±0.36	0.25±0.33	0.66±0.37	0.36±0.30
03528	0.05±0.33	0.09±0.33	0.21±0.33	0.12±0.29

Table 4.5: Mean values for [X/H] and [X/Fe] for Galactic Bulge.

X	[X/H]	[X/Fe]
Fe	–0.25±0.27	
Si	–0.41±0.27	–0.17±0.38
Ca	0.12±0.19	0.12±0.33
Ti	0.01±0.22	0.22±0.35
α		0.06±0.30

Table 4.6: The S/N for the Galactic Bulge stars for 6931-7246Å and 6381-6624Å part of the spectrum.

MWZ ID	Star ID	S/N for 6931-7246Å	S/N 6381-6624Å
64	00956	154.9	152.6
134	02971	108.4	178.7
23	00571	107.8	167.1
30	00629	150.6	164.4
90	01360	121.8	144.8
45	00792	95.2	165.3
30	06290	93.9	169.4
117	02443	103.4	176.9
162	03734	93.8	124.4
107	01998	102.6	145.8
5	00270	82.8	150.9
219	07086	89.6	146.6
253	08713	82.3	124.9
128	02810	94.9	103.4
99	01491	78.2	123.8
2	00138	74.6	109.1
202	06068	64.0	115.0
87	01295	62.3	81.7
195	05789	67.4	99.1
231	07750	69.1	88.9
20	00522	60.9	112.4
86	01298	62.1	125.3
114	02392	60.5	109.9
78	01158	57.9	110.3
135	02983	65.2	104.0
150	03458	47.9	98.0
153	03528	53.0	104.5

Chapter 5

Discussion

5.1 Overview

Abundances for the Bulge stars were less challenging to measure when compared to the Sgr dSph as the Bulge spectra have higher S/N. De-blending is also a problem for the Bulge data, though it affects different lines. The average abundances of Fe I, Fe II, Ca, Si and Ti are higher for the Bulge stars when compared to the stars in the Sgr dSph galaxy which helps to confirm the status of the Sgr dSph as a metal-poor galaxy. Table 5.1 shows the average values for [X/H] and [X/Fe] for Galactic Bulge and Sgr dSph Stars.

Table 5.1: Mean values for [X/H and [X/Fe] for Galactic Bulge and Sgr dSph stars.

Abundance Ratio	Sgr dSph	Galactic Bulge
[Fe/H]	–0.82±0.005	–0.25±0.27
[Si/H]	–0.59±0.28	–0.41±0.27
[Ca/H]	–0.85±0.25	0.12±0.19
[Ti/H]	–0.40±0.22	0.01±0.22
[Si/Fe]	0.23±0.40	–0.17±0.38
[Ca/Fe]	–0.02±0.37	0.12±0.33
[Ti/Fe]	0.38±0.36	0.22±0.35
[α/Fe]	0.20±0.30	0.06±0.30

5.2 Iron abundances

The Fe abundance is lower in the Sgr dSph than the Galactic Bulge, see table 3.3 and 4.3. The variation in Fe abundance in Sgr dSph is due to a number of reasons, including:

1. There is a mostly real, intrinsic spread in the Fe abundance within the Galaxy.
2. The additional artificial spread arises from errors in continuum setting (2.4.2) and noise in the spectra.

5.2.1 Comparison between Sgr dSph and Bulge

The metallicity spread for the stars Sgr dSph (table 3.3) was found to be [Fe/H]= –1.30 to –0.36 dex, with a mean of [Fe/H] = –0.82 dex. While 70% of the stars had a [Fe/H]<–1, the other 30% had [Fe/H] > –1 (table 4.3). For the Bulge the metallicity distribution is wide and covers all metallicities between [Fe/H] = –1.15 to +0.53 dex, with a mean [Fe/H] = –0.25 dex. A small population of 4% of the Bulge stars had –1<[Fe/H] < 0 and 70 % had [Fe/H] < –1, with another population of 26 % having a [Fe/H] > 0, with a maximum of +0.53 dex. These results do confirm that the Sgr dSph is metal poor when compared with the Bulge, which shows greater range of metallicities. A possible explanation for the range of metallicities seen in both galaxies is that the stars in the Sgr dSph are more homogeneous than those in the Bulge which exhibit a range of [Fe/H] values.

The abundances of metal-rich ([Fe/H]>-1) stars are dominated by the ejecta of an old metal poor population, which includes products of type Ia supernovae and AGB stars (McWilliam & Smecker-Hane 2005). There are two possible explanations for this result:

1. Chemical enrichment has taken place over prolonged time-scales in a galaxy which has experienced considerable mass loss during its evolution, which cut

short the chemical enrichment before the whole conversion of the gas into stars could occur.

2. The results we are seeing are the due to the chemical enrichment from a system which may have experienced a considerable burst of star formation, which is followed by a dormant period of many Gyr.

It is probable that both of the above mechanisms may function in the Sgr dSph. These type of conditions are generally applicable to low mass systems and it would be expected to find similar abundance results in other dwarf galaxies. This is supported by the chemical composition of the stars in Fornax dwarf galaxy, which leads to the idea that Sgr dsph and Fornax both shared a history (McWilliam & Smecker-Hane 2005).

Another possible explanation for the low mean [Fe/H] is the results of steep stellar IMF (McWilliam, Wallerstein & Mottini 2013). The most likely answer to the question of the reason for the low mean [Fe/H], is that since the Sgr dSph is low mass galaxy, the chemical evaluation took place in the presence of considerable gas loss (e.g. leaky box evolution) (McWilliam, Wallerstein & Mottini 2013).

5.2.2 Comparison to existing literature

In this project the mean [Fe/H] for the Sgr dSph was –0.82 dex with a spread from –1.31 to –0.36 dex. The Sgr dSph contains several identified populations (McDonald et al. 2012), which been summarized by Siegel et al. (2007) (section 1.5.2). Bellazzini et al. (2006) found that the the bulk population of the Sgr dSph had [Fe/H] $\approx$ –0.7 to –0.4 dex, which can be compared to the mean [Fe/H] = –0.82 dex found in the project (section 1.5.2). Smecker-Hane & McWilliam (2002), found a metallicity range of –1.6$\leqslant$ [Fe/H]$\leqslant$ –0.05, this spread is lower in this project and in my judgement this is due the selection criteria used as only K–type stars were selected for analysis and S/N issues in the spectra of the Sgr dSph stars (section 2.4.1).

Based on the results from Smecker-Hane & McWilliam (2002) the stars in this project cover a wide a range of ages from ∼1.5 to ∼15 Gyr, which cover the full age distribution of stars found the Bulge (Bensby et al. 2013). The data from this project and other studies indicate (Bensby et al. 2013; Johnson et al. 2014, 2011) that there is more than one population in the Bulge. In this project for the Bulge, the mean [Fe/H]= –0.25 dex, with a spread from –1.15 to +0.53 dex. The results from Bensby et al. (2010) found that the Bulge stars span the full range of metallicities from [Fe/H] = –0.72 to +0.54 dex and the study carried out by Gonzalez et al. (2011), who found mean, [Fe/H] < –0.50 and (McWilliam & Rich 1994) and (Zoccali et al. 2003) found that Bulge metallicity spans a wide range, ~ -1.5 to $\sim +0.5$ and this fits in with results found for the Bulge in the project, were [Fe/H] = –1.15 to +0.53 dex. The difference in the results is part due the selection criteria used in this project for the Bulge stars, as only K–type were analysed (section 4.2) and the location of the stars within the Bulge.

5.2.3 Colour-Magnitude Diagram

Figure 5.1 shows the 2MASS colour–magnitude diagram in the direction of the Sgr dSph and Galactic Bulge stars. The right-most branch in the CMD is the giant branch of the Sgr dSph, extending from K ≈ 13 up to the RGB tip around K ≈ 10. The majority of the stars analysed here are mostly towards the base of the giant branch at lower $(J - K_{\rm s})$ values, towards the left edge of the Sgr dSph giant branch.

The position on this diagram of the Sgr dSph stars we have analysed is due to the selection criteria (K–type stars were analysed, see section 2.4.1) used in this project. These criteria resulted in only metal poor stars being analysed. The metal-poor stars have fewer metal lines, hence less atmospheric opacity and they radiate energy more effectively, which results in the stars being warmer. These warmer stars have lower $(J - K_{\rm s})$ colours. Hence they are more likely to be K–type stars. As these stars will tend to be (a) warmer so that TiO can't form and (b) metal-poor because [Ti/H] and [O/H] mean less TiO absorption. Hence the stars observed are biased toward observing metal-poor stars.

The Bulge stars on the CMD diagram extend up to the RGB tip around K ≈ 6.8. The spread in position of the observed Bulge stars is due in part to the criteria used in selecting these Bulge stars (section 4.2). These stars are typically hotter than those analysed in the Sgr dSph (table 2.4 and 4.2) and as a result of the selection process, M-type stars have been excluded. Additionally stars were selected which had the best S/N and this tended towards the warmest stars, which resulted in bias towards the metal-poor stars.

However, it is likely that some of the Bulge stars are not in the Bulge but are in the Galactic Disc, which explains their higher metallicity, [Fe/H]. The stars in the Galactic Disc will be typically be closer to the stars analysed in this project and hence they will have a higher surface gravity at any given effective temperature.

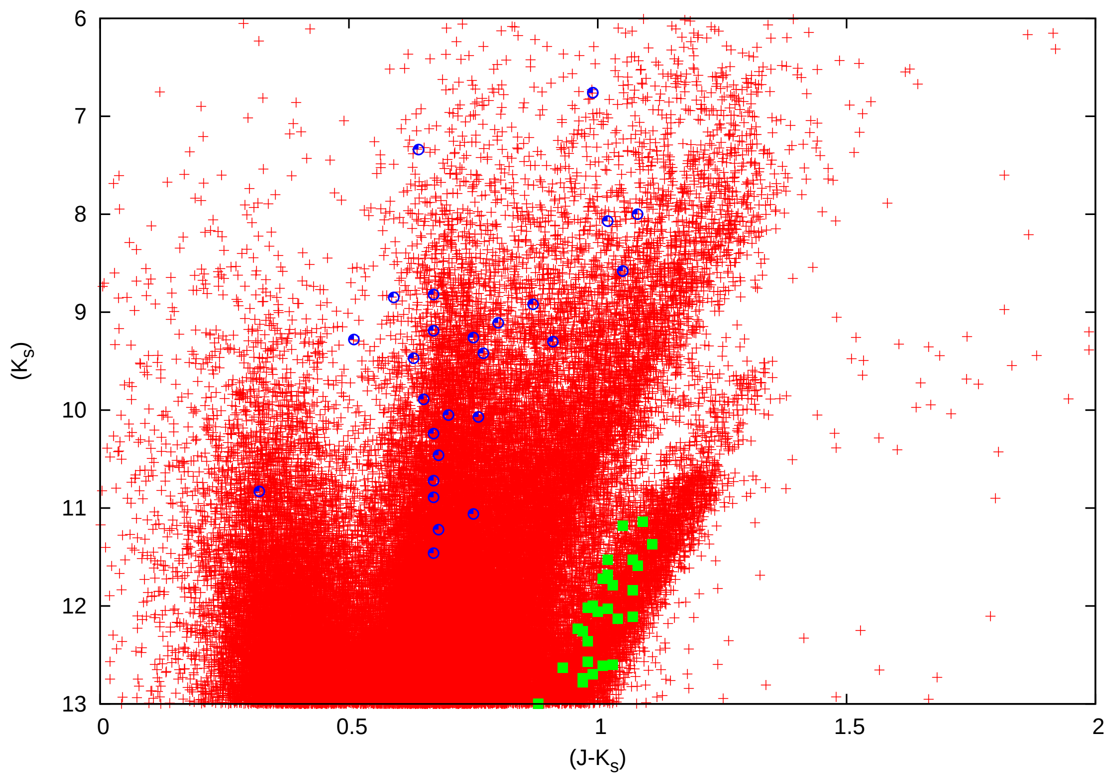

Figure 5.1: Colour–magnitude diagram for the Sgr dSph (green squares) and Galactic Bulge (blue circles) stars, compared to the complete 2MASS(red crosses) sample towards the Sgr dSph.

Figures 5.2 and 5.3 show T_{eff} versus log(g) for the Sgr dSph and Bulge stars.

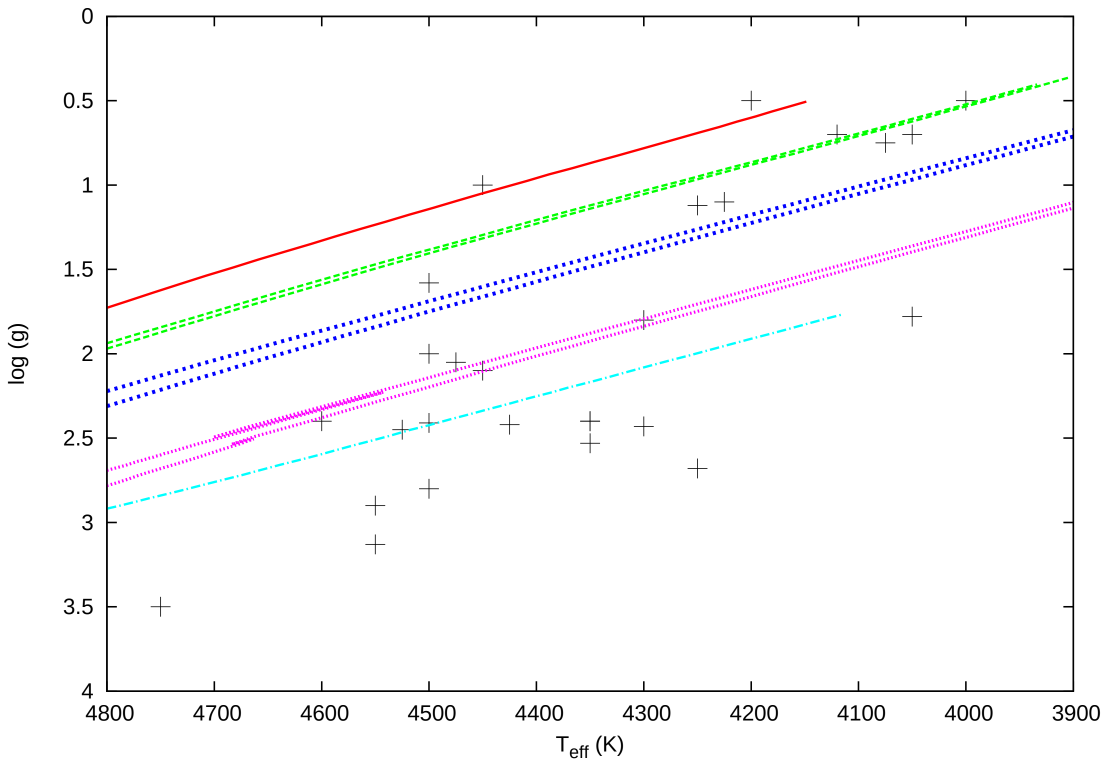

Figure 5.2: T_{eff} versus log(g) for the Sgr dSph stars overplotted with Dartmouth synthetic isochrones presented by McDonald et al. (2013). Where the red represent the M54 population; blue represents the metal-intermediate population; magenta represents the metal-rich population and cyan represents the very metal rich population.

Figure 5.2 shows T_{eff} versus log(g) for the Sgr dSph Stars. Most of the stars lie on or are close to the isochrones when taking into account the amount of scatter in the data. Figure 5.3 shows show T_{eff} versus log(g) for the Bulge stars, most of the stars lie close to the isochrones but stars which lie above the isochrones are likely to be red clump or AGB stars.

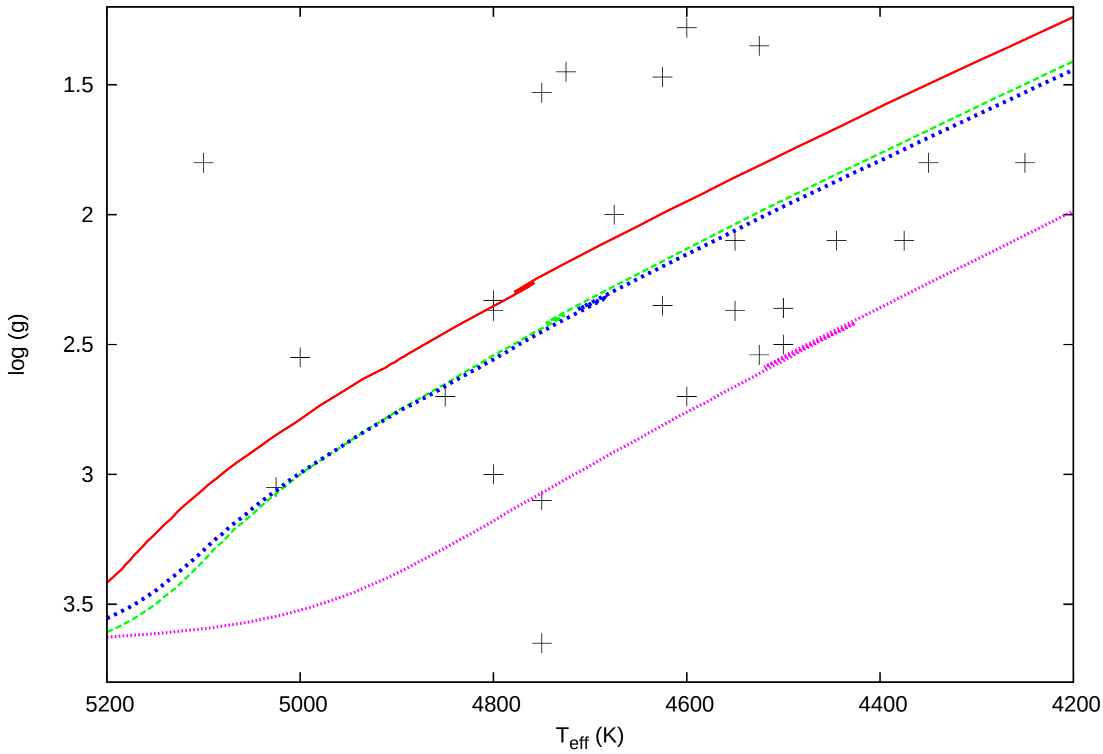

Figure 5.3: T_{eff} versus log(g) for the Bulge stars. Where red line is 12 Gyr([Fe/H] = –1.0 and [α/Fe] = +0.4); green 9 Gyr [Fe/H] = –0.6 and [α/Fe] = +0.2; blue 6 Gyr [Fe/H] = –0.4 and [α/Fe] = 0.0) and pink 3 Gyr [Fe/H] = +0.4 and [α/Fe] = -0.2) (Gesicki et al. 2014)

5.3 Abundance of the other elements

The variation in and accuracy of the abundances of Ca, Si and Ti are influenced by a number of factors which include the number of lines which could be measured along with the S/N in each stellar spectrum. In the case of Si and Ti it was in some cases only possible to measure just a few lines (1-3) and this had a bigger impact on the results when compared to Ca and Fe where far more lines could be measured (table 4.3 and 3.3).When calculating the stellar abundances, the errors are dominated by the uncertainties in the EW measurements and stellar parameters (T_{eff}, log g, [Fe/H] and υ_t), which are used in MOOG to determine the abundances of the elements.

5.3.1 [Ca/Fe] versus [Fe/H] trends

Figure 5.4 shows plots [Ca/Fe] vs [Fe/H] for the Sgr dSph and Bulge stars. The [Ca/Fe] for the Sgr dSph has greater amount of scatter (which is due to the S/N issues and the number of lines that could be measured) and hence it is difficult to determine any changes in [Ca/Fe] with [Fe/H] for the Sgr dSph. However in the case of the Bulge, the position of the knee is well defined, at [Fe/H] $\approx$ –0.4 dex. In this project a mean of [Ca/Fe] = –0.02 dex and [Ca/Fe] = 0.12 dex were found for the Sgr dSph and the Bulge respectively. This compares with Monaco et al. (2005) who found a mean of, [Ca/Fe] = –0.12 dex (for bright RGB stars in Sgr dSph) and Bonifacio et al. (2004), [Ca/Fe] = –0.22 dex (for metal rich stars in Sgr dSph) and in the case of the Bulge, Gonzalez et al. (2011) found, [Ca/Fe] $\sim$ 0.16 dex. The difference in results found in this project and published work can in part be explained by the selection criteria used in this project for both the Sgr dSph and Bulge galaxies. Since the selection criteria (section 2.4.1) is biased towards metal poor stars, this would result in a higher mean [Ca/Fe]. The issues of low S/N and blending of the lines, has not greatly affected the mean abundance but has produced scatter in results (table 4.4 and 3.4).

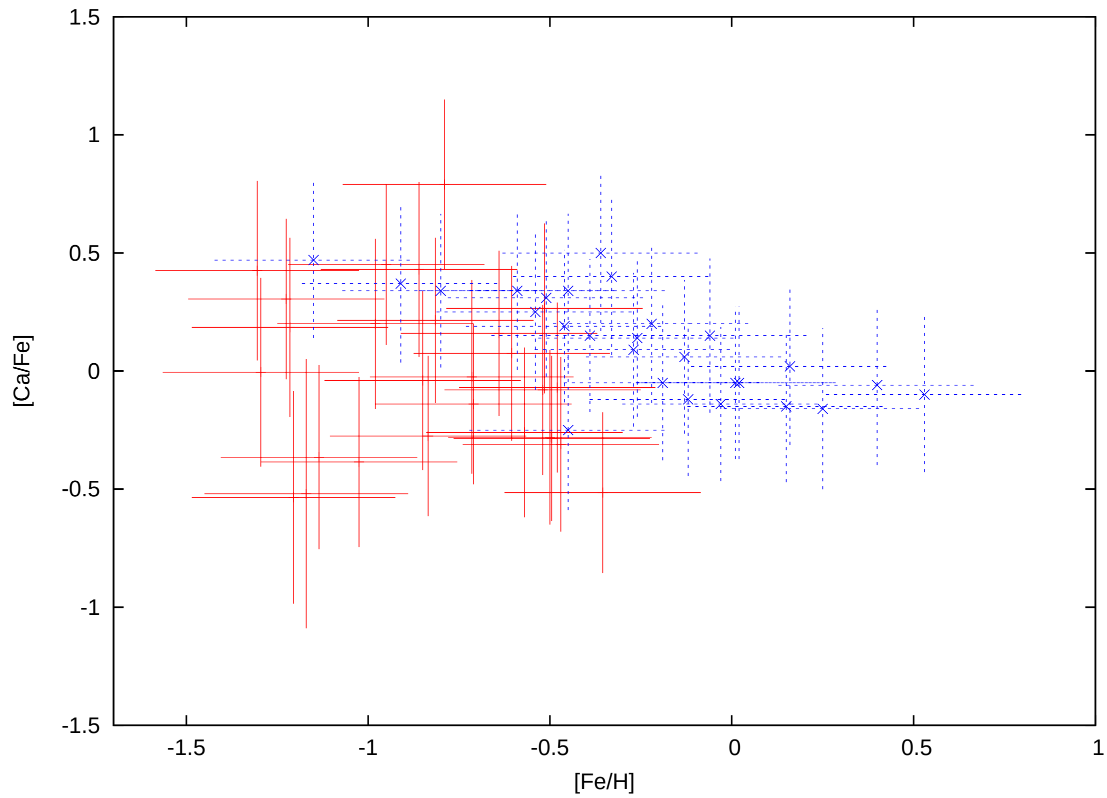

Figure 5.4: [Ca/Fe] versus [Fe/H] for the Sgr dSph (red crosses) and Bulge (blue crosses) stars.

5.3.2 [Si/Fe] versus [Fe/H] trends

Figure 5.5 shows plots [Si/Fe] vs [Fe/H] for the Bulge and Sgr dSph. In this project, a mean [Si/H] for the Sgr dSph was 0.23 dex and –0.17 dex for the Bulge. The [Si/Fe] for the Sgr dSph shows a declining trend with [Fe/H] and the position of the knee is approximately, [Fe/H] = –0.80 dex. In the Bulge there is no obvious break point and there are Si-poor stars at [Fe/H] = –0.4 dex, which is where the position of the knee is probably located. In both sets of data there is scatter which results from the limited number lines that could measured (see tables 4.3 and 3.3). Gonzalez et al. (2011) found the mean [Si/Fe] = +0.13 dex (this was for 650 K-giants in four Bulge fields), which is larger than the results found in this project. Smecker-Hane & McWilliam (1999) found a mean [Si/Fe]= +0.10 dex which is in line with the results found for the Sgr dSph stars in this project. The difference is due to the selection criteria used when selecting the Bulge and Sgr dSph stars (only metal-poor stars have been analysed in both the Bulge and Sgr dSph).

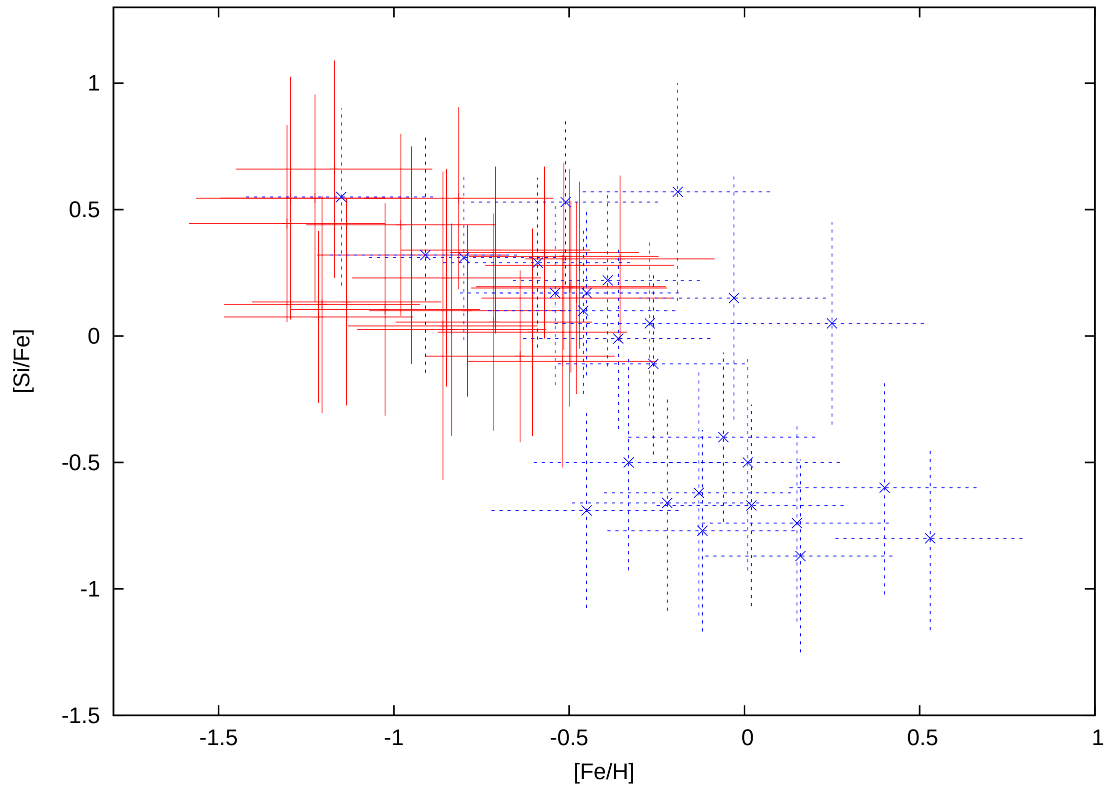

Figure 5.5: [Si/Fe] versus [Fe/H] for the Sgr dSph (red crosses) and Bulge (blue crosses) stars.

5.3.3 [Ti/Fe] versus [Fe/H] trends

Figure 5.6 shows the [Ti/Fe] vs [Fe/H] for the Bulge and Sgr dSph. A mean of [Ti/Fe]= 0.38 dex for the Sgr dSph and [Ti/Fe] = 0.22 dex for Bulge were found in this project. The [Ti/Fe] for the Sgr dSph does show a systematic trend but it is harder to see due the the scatter and the same is true for Bulge. The amount of scatter in both galaxies is due to the small number of measured lines (table 4.3 and 3.3). Monaco et al. (2005) found a mean [Ti/Fe] = 0.02 dex for the Sgr dSph and this compares to mean of [Ti/Fe] = 0.38 dex found in this project and Gonzalez et al. (2011) found a mean of [Ti/Fe] = 0.26 dex for the Bulge and this is in agreement with the result found in this project. The main reason why the Bulge and Sgr dSph results are lower than published works is that in both cases the selection criteria used in this project are biased towards the metal-poor stars.

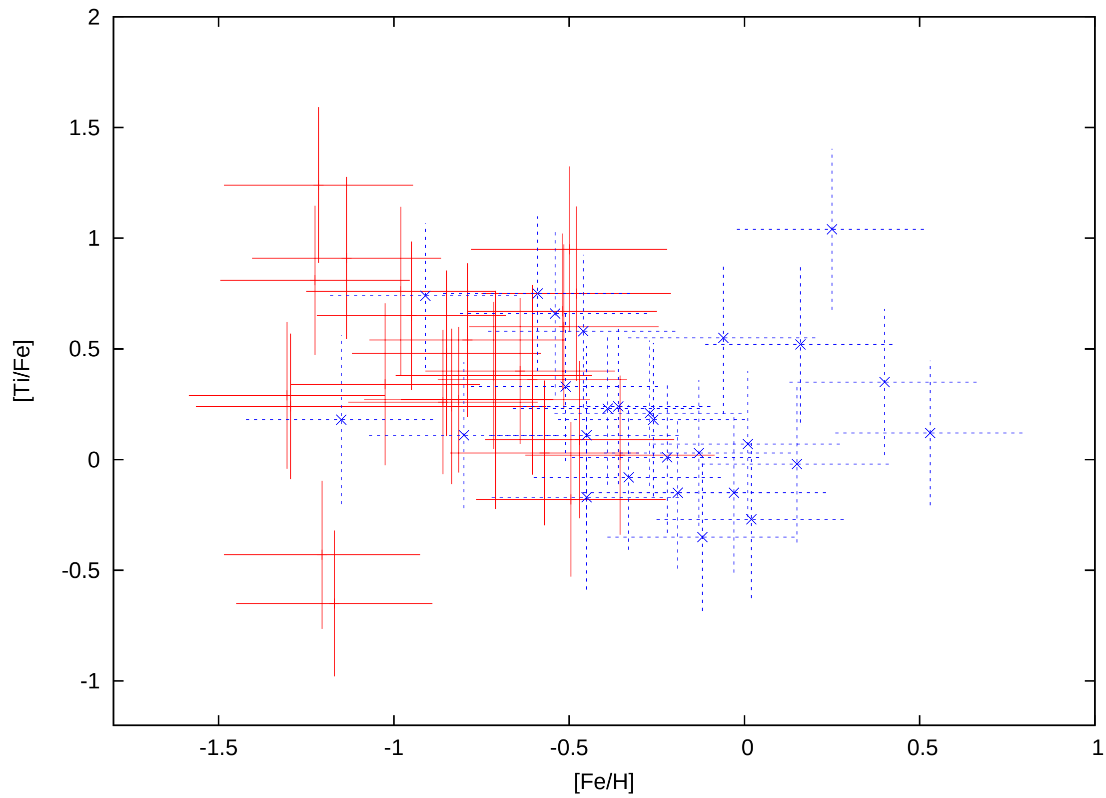

Figure 5.6: [Ti/Fe] versus [Fe/H] for the Sgr dSph (red crosses) and Bulge (blue crosses) Stars

5.3.4 [α/Fe] versus [Fe/H] Knee

The mean value for [α/Fe] for the Sgr dSph is 0.20 dex and this is close to the nascent [α/Fe] of $\sim$ 0.3 dex. In the case of the Bulge the mean [α/Fe] = 0.06 dex is closer to the solar value. Gonzalez et al. (2011) found [α/Fe] = 0.19 dex, for 650 K -giants in the the Milky Way Bulge, which is larger than the result found in this project for the Bulge. This difference in results can be in part be explained by the selection criteria used in this project which is biased towards metal-poor stars. The [α/Fe] ratio observed in the the Sgr dSph can understood by looking at the model proposed by Tinsley (1979)(also Wheeler, Sneden & Truran (1989); McWilliam (1997)). In the model suggested by Tinsley the low metallicity (-1$\leq$[Fe/H]$\leq$0) halo stars have high [α/Fe], which is a feature of ejecta from core-collapse Type II SN. The observed [α/Fe] in the Sgr dSph are consistent with yields of low-mass ($\lesssim$ 20 $M_{\odot}$) core-collapse (Kobayashi et al. 2006). The contribution of low mass supernova can be dominant in regions with very low SFRs.

Figure 5.7 shows the [α/Fe] ratio for Sgr dSph and Bulge. This result can be compared with previous work published by McWilliam & Rich (1994) and McWilliam, Wallerstein & Mottini (2013), as the trend shown in figure 1.11 compares with figure 5.7. Siegel et al. (2007) found for the Sgr dSph [α/Fe] = 0.20 dex which is identical to the results found in this project for the Sgr dSph. Figure 5.7 provides an indication that the [α/Fe] extends below solar for the highest metallicity stars for some of the stars in the Bulge. The metallicities which are shown in figure 5.7, support the idea of a slow or bursting star-formation rate (Ballesteros-Paredes & Hartmann 2007; Bonifacio et al. 2004). The knee in figure 5.7 for the Bulge is at [Fe/H] = –0.5 and this consistent with McWilliam & Rich (1994); see figure 1.14. The results found by McWilliam & Rich (1994) are consistent with the values found for each of the individual found in this project. However the position knee for the Sgr dSph is harder define due to the scatter in the data however the plot is consistent with the work by McWilliam, Wallerstein & Mottini (2013); see figure 1.13. The position of the knee is expected to be different for dSphs since they have varied star formation histories (Tolstoy, Hill & Tosi 2009).

The [α/Fe] results achieved in table 5.1 compare with the published results (section 1.5.2) however the difference in results is due to the following reasons:

1. The selection criteria used, limited the analysis to the warmer stars which biased the analysis towards metal poor-stars (section 2.4.1 and section 5.2.3, hence also α-rich stars).

2. S/N issues in the Sgr dSph made calculating EW and abundances very challenging (section 2.4.2). As incorrectly setting the continuum leads to either over/under estimating the abundances.

3. The number of lines which could be measured for some of the elements was limited (table 3.3 and 4.3).

5.3.5 The chemical enrichment history of the Sgr dSph

Since the Type II SN progenitors only last for short period, they are first to eject their material back into the ISM. Type Ia supernova enrichment occurs from $\sim$ 200Myr up to the present day. Since the Type Ia SN produce few α-element nuclei, this results in the composition of the stars which are formed from their ejecta having lower [α/Fe] ratios.

In this scenario the [Fe/H] value at which the [α/Fe] begins to reduce from the SN II ratio(the [α/Fe], knee) depends upon the star formation rate in the oldest populations. In the case of slowly evolving systems it is expected that [α/Fe] will decline at lower [Fe/H] owing to the fact that they do not reach as high [Fe/H] before the time when Type Ia SN begin to contribute considerably to the ISM composition (McWilliam & Smecker-Hane 2005). Hence the results of [α/Fe] in this project indicate that the Sgr dSph initially had a lower star-formation rate than the solar neighbourhood and the Galactic Bulge experienced.

Since the knee marks the time of the first SN Ia, then the formation time scale of a galaxy can be estimated by determining the quantity of stars with [Fe/H] which are below the knee (Tinsley 1979; McWilliam 1997). Figure 5.7 shows that most of the metal poor-stars in the Sgr dSph exhibit the enhanced [α/Fe] ratio which is seen in the Galactic halo, near +0.3 dex, but above [Fe/H] ~ -1 the α elements become progressively more deficient compared to the solar neighbourhood at any given [Fe/H] value. A possible explanation of this result (McWilliam 1997; Wheeler, Sneden & Truran 1989) is that ratio of type Ia/type II SNe material in the Sgr dSph is larger than the solar neighbourhood above [Fe/H] $= -1$ and this is probably due to a slower star formation rate in the Sgr dSph compared to the Bulge. These variations of α elements have long been predicted for low mass systems (Matteucci & Brocato 1990; Gilmore & Wyse 1991).

The metal-poor stars in the Sgr dSph have [α/Fe] ratios which are similar to those of the Galactic halo stars and this is basically equal to the yield of type II SN. This

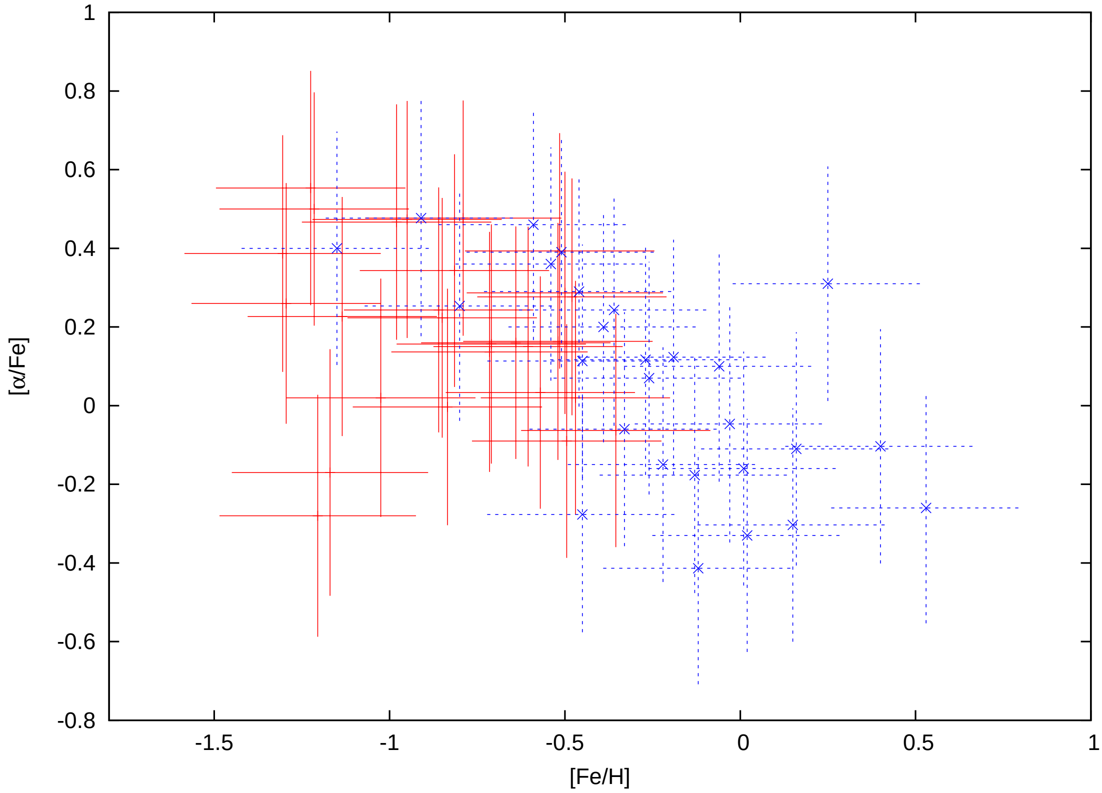

Figure 5.7: [α/Fe] versus [Fe/H] for the Sgr dSph (red crosses) and Bulge (blue crosses Stars

means that the upper mass end of the IMF in the dSphs is not significantly different from the Galaxy (Smecker-Hane & McWilliam 2002).

5.4 Radial dependences

Radial dependences are seen in galaxies of different sizes, such as globular clusters like M31 and in the Small Magellanic Cloud (Bekki 2008). Figures 5.8 - 5.12 show [X/Fe] versus radial distance for the Sgr dSph stars. In all of the plots there is no obvious overall trend due to the amounts of scatter in the data and the lack of a trend shows that there is no variation with radial distance. These plots do show that the elements are homogeneous throughout the Sgr dSph stars analysed in this project. Table 5.2 shows the mean abundance for radii $<0.6^0$ and radii $>0.6^0$ for Sgr dSph and the results confirm that there no radial dependence which is significant. The analysis of the data is complicated by the large scatter in the data (section 2.4.1).

In dwarf galaxies radial abundances gradients are expected and the reason why radial dependences are not seen in plots 5.8 - 5.12 is most likely due to the tidal stripping which is occurring in the Sgr dSph (Lokas et al. 2012). The effects of tidal stripping result in significant mass loss occurring during the evolution of the Sgr dSph. This will have resulted in a truncated chemical enrichment before complete conversion of the gas into stars occurred (McWilliam 1997) (section 1.5.2)

Table 5.2: The mean abundances of radii $<0.6^0$ and radii $>0.6^0$ for Sgr dSph Stars.

Element	radii $<0.6^0$	radii $>0.6^0$
[α/Fe]	0.17±0.06	0.24±0.05
[Ti/Fe]	0.29±0.12	0.57±0.09
[Ca/Fe]	–0.06±0.08	0.00±0.12
[Si/Fe]	0.27±0.05	0.15±0.06
[Fe/H]	–0.84±0.08	–0.73±0.09

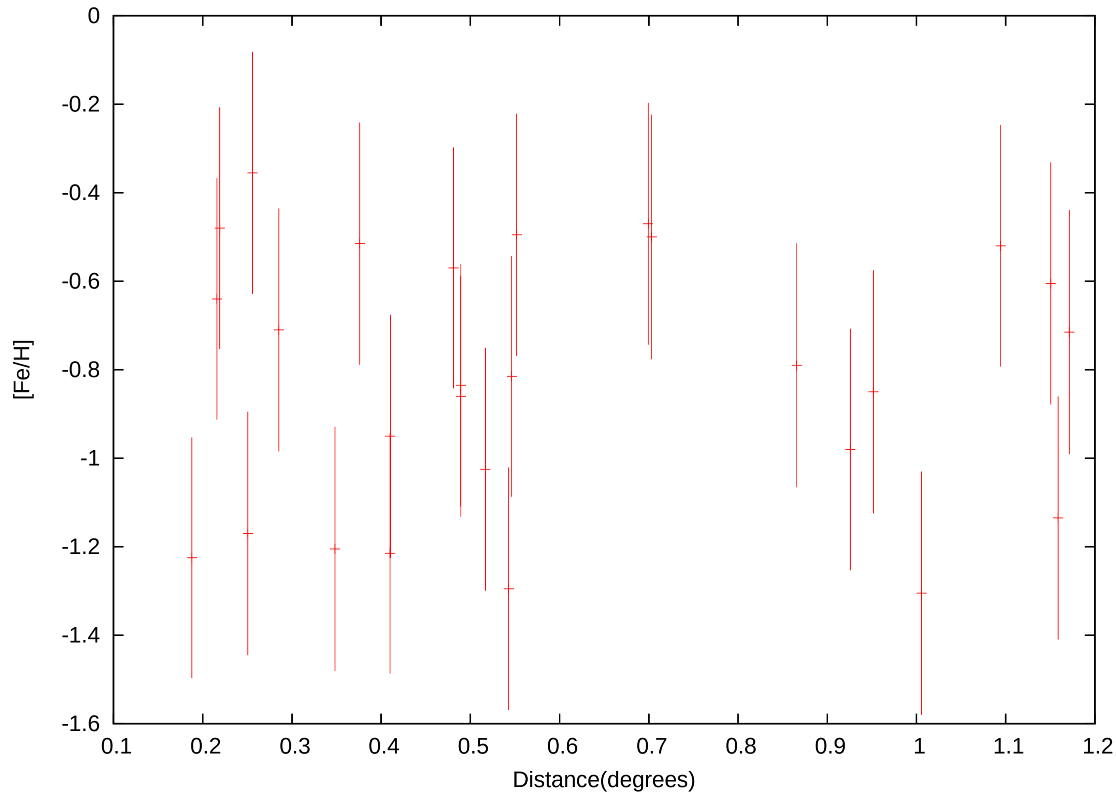

Figure 5.8: [Fe/H] versus Distance (from the galactic centre M54) for the Sgr dSph Stars.

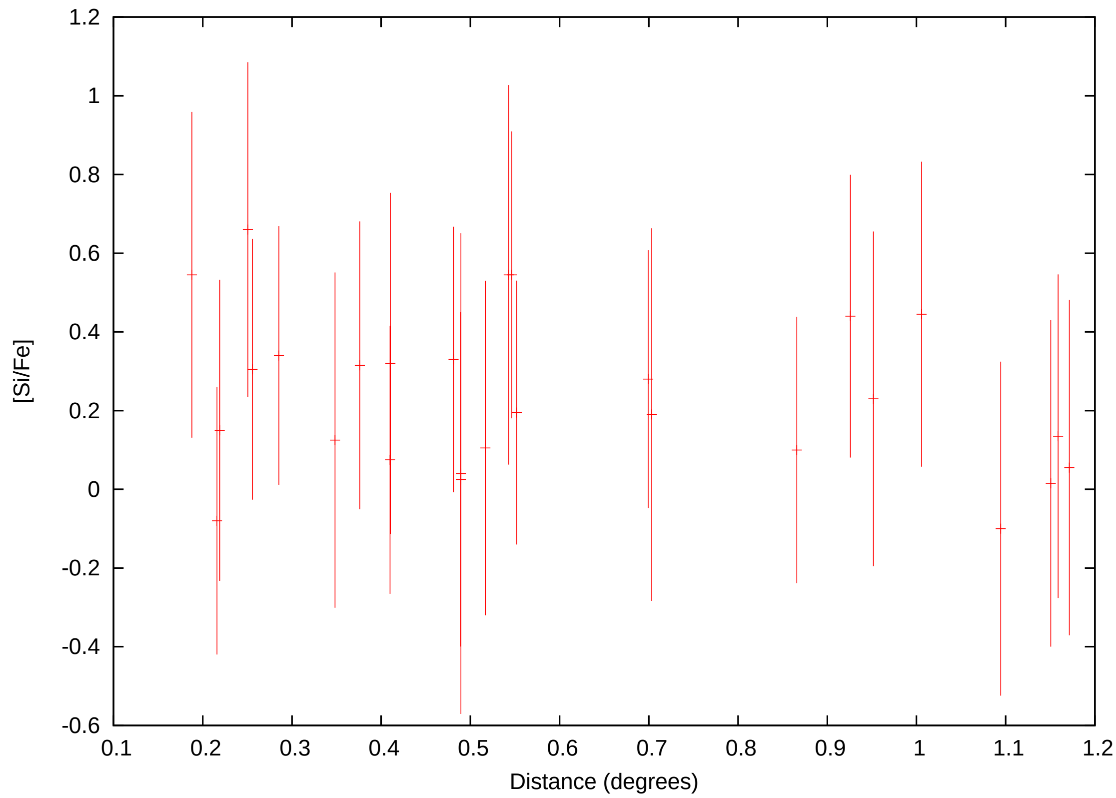

Figure 5.9: [Si/Fe] versus Distance (from M54) for the Sgr dSph stars.

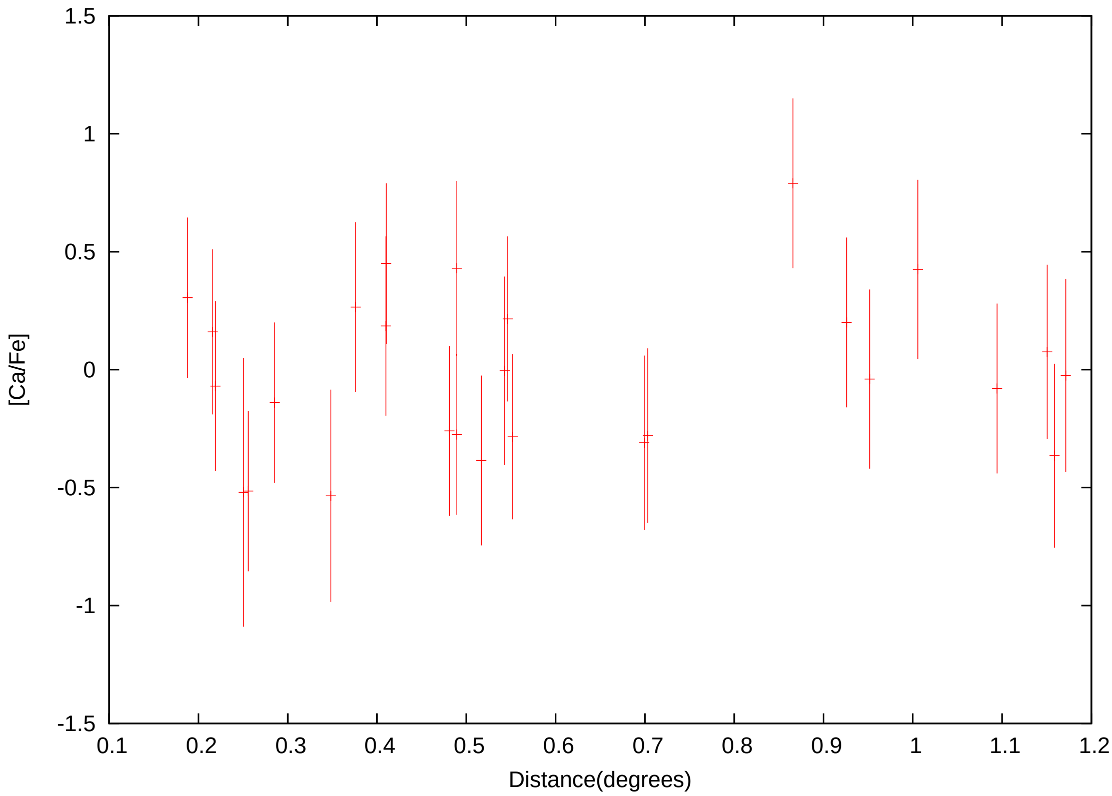

Figure 5.10: [Ca/Fe] versus Distance (from M54) for the Sgr dSph stars.

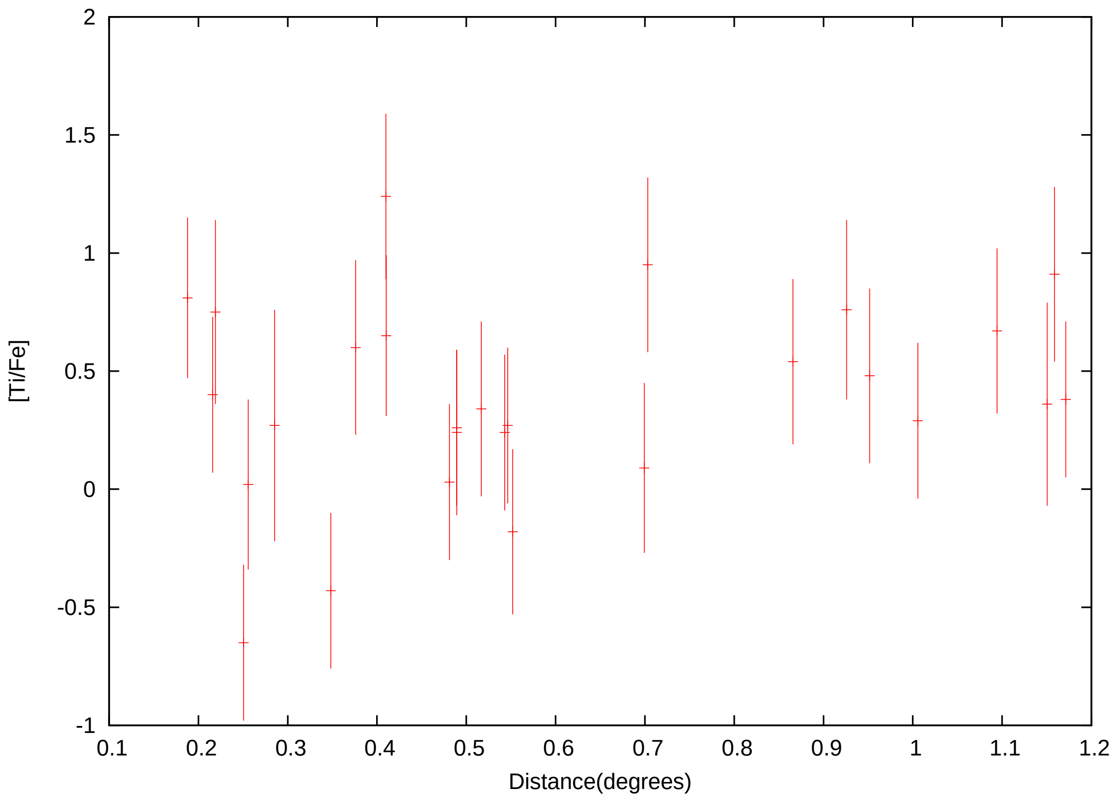

Figure 5.11: [Ti/Fe] versus Distance (from M54) for the Sgr dSph stars.

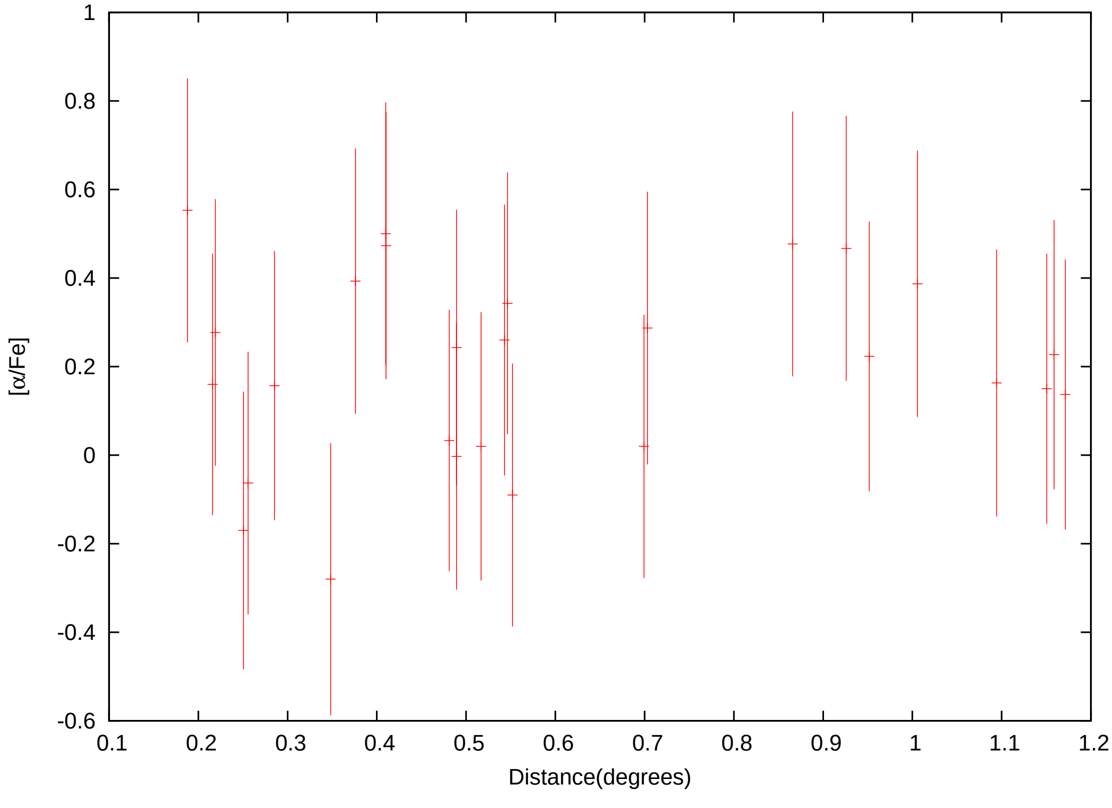

Figure 5.12: [α/Fe] versus Distance (from M54) for the Sgr dSph stars.

Chapter 6

Conclusion

In this project, the abundances of Fe I, Fe II, Ca, Si and Ti were derived for 27 stars in the Sgr dSph galaxy, and a control sample of 27 stars in the Galactic Bulge. The effective temperature, surface gravity and microturbulence were also calculated for each star. The ratios of each element to iron and hydrogen for both sets of stars were also calculated. In summary, the findings and main results from this project are:

1. The chemical composition of Sgr dSph stars is different from the Galactic Bulge stars. Many elements (Ca, Si, Ti, Fe) in the Sgr dSph show an under-abundance when compared to the Bulge stars.

2. The sample of Sgr dSph stars have mean metallicity of [Fe/H] = –0.82 dex with range of –1.31 to –0.35 dex, [α/Fe] = 0.20 dex with range of –0.28 to 0.55 dex. The mean metallicity found in the project is below those found by Siegel et al. (2007) and this is due the selection criteria used in this project, which favoured the selection of metal-poor stars. The metallicity distribution of the Sgr dSph is similar to that seen in other dwarf galaxies in the Local Group (Monaco et al. 2003).

3. The mean metallicity for the bulge sample is, [Fe/H] = –0.25 dex with a range of –1.15 to 0.53 dex. This is considerably higher than the results for the Sgr

dSph.

4. For the Sgr dSph the [α/Fe] ratio declines with [Fe/H] from 0.4 to –0.1 dex and the [α/Fe] knee is at approximately –0.8 dex. For the Bulge the [α/Fe] ratio declines with [Fe/H] from 0.4 dex to –0.3 dex and the [α/Fe] knee is at approximately –0.6 dex. The difference in the positions of knees support the fact the enrichment occurred faster in the Bulge stars. The extent to which the Sgr dSph has changed by the interaction with the MW is currently difficult to assess. Additionally the low [α/Fe] ratios imply that type Ia SN contribute to the composition of the younger, metal rich SGR population.

5. The lack of radial abundance variations in section 5.4 shows that the population is homogeneous and all the populations are seen at all radii. This is different to other dwarf galaxies and is likely a result of tidal stripping that's going on in the Sgr dSph.

Appendix A

Abundances of the Sun

The abundances of the elements can be given in two forms, the bracket notation and the log ϵ notation. In the bracket notation, [Fe/H] = –1 means that the star has a tenth of the iron-to-hydrogen ratio of the Sun. While in the log ϵ notation the abundances are expressed relative to 10^{12} hydrogen atoms, log ϵ (H) = 12. For every H atom, there are $10^{-4.5}$ iron atoms in the Sun, so logϵ (Fe) = 7.5. The following abundances were used in the calculation of [X/H] and [X/Fe] (Gonzalez et al. 2011).

Table A.1: Abundances of the Sun.

	Ca	Mg	Ti	Si	Fe
Sun	6.39	7.60	4.95	7.51	7.52

References

Aller L. H., Greenstein J. L., 1960, ApJS, 5, 139

Ballesteros-Paredes J., Hartmann L., 2007, , 43, 123

Barbuy B. et al., 2008, Physica Scripta Volume T, 133, 014032

Bartunov O. S., Tsvetkov D. I., 1986, Ap&SS, 122, 343

Bekki K., 2008, Evolution of the Small Magellanic Cloud, Koribalski B. S., Jerjen H., eds., p. 247

Bellazzini M., Correnti M., Ferraro F. R., Monaco L., Montegriffo P., 2006, A&A, 446, L1

Bellazzini M., Ferraro F. R., Buonanno R., 1999a, MNRAS, 304, 633

Bellazzini M., Ferraro F. R., Buonanno R., 1999b, A&A, 307, 619

Bensby T. et al., 2011, A&A, 533, A134

Bensby T. et al., 2010, A&A, 512, A41

Bensby T. et al., 2013, A&A, 549, A147

Blöcker T., Driebe T., Herwig F., 1999, in Astronomische Gesellschaft Meeting Abstracts, Vol. 15, Astronomische Gesellschaft Meeting Abstracts, Schielicke R. E., ed., p. 25

Bonačić Marinović A., Izzard R. G., Lugaro M., Pols O. R., 2007, A&A, 469, 1013

Bonifacio P., Hill V., Molaro P., Pasquini L., Di Marcantonio P., Santin P., 2000, A&A, 359, 663

Bonifacio P., Sbordone L., Marconi G., Pasquini L., Hill V., 2004, A&A, 414, 503

Bradel C., Ostile D., 2007, A An introudction to modern astrophysics. Addison-Wesley Publishing., Connecticut, USA

Caimmi R., 2011, Serbian Astronomical Journal, 183, 37

Carlberg J. K., 2014, AJ, 147, 138

Carraro G., Ng Y. K., Portinari L., 1998, MNRAS, 296, 1045

Carretta E. et al., 2010, A&A, 520, A95

Castelli F., Kurucz R. L., 2004, Proceedings of the IAU Symp. No 210; Modelling of Stellar Atmospheres, eds. N. Piskunov et al., poster A20

Cayrel R. et al., 2004, A&A, 416, 1117

Chiosi C., Matteucci F., 1983, in Primordial Helium, Shaver P. A., Kunth D., Kjar K., eds., pp. 77–88

Chou M.-Y. et al., 2007, ApJ, 670, 346

Cole A. A., 2001, ApJ, 559, L17

Cutri R. M. et al., 2003, 2MASS All Sky Catalog of point sources.

Dray L. M., Tout C. A., 2003, MNRAS, 341, 299

Epstein C. R., Johnson J. A., Dong S., Udalski A., Gould A., Becker G., 2010, ApJ, 709, 447

Foley R. J., Mandel K., 2013, ApJ, 778, 167

Fulbright J. P., Rich R. M., McWilliam A., 2006, Abundance Ratios in the Galactic Bulge, Randich S., Pasquini L., eds., p. 93

Gehrz R., 1989, in IAU Symposium, Vol. 135, Interstellar Dust, Allamandola L. J., Tielens A. G. G. M., eds., p. 445

Gesicki K., Zijlstra A. A., Hajduk M., Szyszka C., 2014, A&A, 566, A48

Gilmore G., Wyse R. F. G., 1991, ApJ, 367, L55

Giuffrida G., Sbordone L., Zaggia S., Marconi G., Bonifacio P., Izzo C., Szeifert T., Buonanno R., 2010, A&A, 513, A62

Gonzalez O. A. et al., 2011, A&A, 530, A54

Graham A. W., 2007, MNRAS, 379, 711

Gratton R., Sneden C., Carretta E., 2004, ARA&A, 42, 385

Hamadache C. et al., 2006, A&A, 454, 185

Hartwick F. D. A., 1976, ApJ, 209, 418

Hernandez X., Valls-Gabaud D., Gilmore G., 1999, MNRAS, 304, 705

Hinkle K., Wallace L., Valenti J., Harmer D., 2000, Visible and Near Infrared Atlas of the Arcturus Spectrum 3727-9300 A. Astronomical Society of the Pacific Monograph Publications

Ibata R. A., Gilmore G., Irwin M. J., 1994, Nature, 370, 194

Iben, Jr. I., Renzini A., 1983, ARA&A, 21, 271

Iben, Jr. I., Truran J. W., 1978, ApJ, 220, 980

Izzard R. G., Tout C. A., 2003, PASA, 20, 345

Johnson C. I., Pilachowski C. A., 2010, ApJ, 722, 1373

Johnson C. I., Pilachowski C. A., Simmerer J., Schwenk D., 2008, ApJ, 681, 1505

Johnson C. I., Rich R. M., Fulbright J. P., Valenti E., McWilliam A., 2011, ApJ, 732, 108

Johnson C. I., Rich R. M., Kobayashi C., Kunder A., Koch A., 2014, published, [arXiv:1407.2282]

Johnson C. I., Rich R. M., Kobayashi C., Kunder A., Pilachowski C. A., Koch A., de Propris R., 2013, ApJ, 765, 157

Karakas A. I., 2011, in Astronomical Society of the Pacific Conference Series, Vol. 445, Why Galaxies Care about AGB Stars II: Shining Examples and Common Inhabitants, Kerschbaum F., Lebzelter T., Wing R. F., eds., p. 3

Karakas A. I., Lattanzio J. C., Pols O. R., 2002, PASA, 19, 515

Kent S. M., Dame T. M., Fazio G., 1991, ApJ, 378, 131

Kippenhahn R., Weigert A., 2007, A Stellar Structure and Evolution. SpringerLink., Newyork, USA

Kobayashi C., Umeda H., Nomoto K., Tominaga N., Ohkubo T., 2006, ApJ, 653, 1145

Kontizas E., Dapergolas A., Kontizas M., Nordström B., Andersen J., Prantzos N., Kaltcheva N., 2001, Astrophysics and Space Science Supplement, 277, 333

Koposov S. E. et al., 2012, ApJ, 750, 80

Lagadec E. et al., 2009, MNRAS, 396, 598

Lanfranchi G. A., Matteucci F., Cescutti G., 2006, A&A, 453, 67

Layden A. C., Sarajedini A., 2000, AJ, 119, 1760

Letarte B., Hill V., Tolstoy E., 2007, in EAS Publications Series, Vol. 24, EAS Publications Series, Emsellem E., Wozniak H., Massacrier G., Gonzalez J.-F., Devriendt J., Champavert N., eds., pp. 33–38

Lokas E. L., Kazantzidis S., Majewski S. R., Law D. R., Mayer L., Frinchaboy P. M., 2012, The Sagittarius Dwarf Galaxy as a Product of Tidal Stirring, p. 113

Lugaro M., Herwig F., Lattanzio J. C., Gallino R., Straniero O., 2003, ApJ, 586, 1305

Marcolini A., D'Ercole A., Brighenti F., Recchi S., 2006, MNRAS, 371, 643

Marconi G., Matteucci F., Tosi M., 1994, MNRAS, 270, 35

Marigo P., Bressan A., Chiosi C., 1996, A&A, 313, 545

Martin N. F., Ibata R. A., Bellazzini M., Irwin M. J., Lewis G. F., Dehnen W., 2004, MNRAS, 348, 12

Marzke R. O., da Costa L. N., 1997, AJ, 113, 185

Matteucci F., Brocato E., 1990, ApJ, 365, 539

McDonald I., White J. R., Zijlstra A. A., Guzman Ramirez L., Szyszka C., van Loon J. T., Lagadec E., Jones O. C., 2012, MNRAS, 427, 2647

McDonald I. et al., 2013, MNRAS, 436, 413

McWilliam A., 1997, ARA&A, 35, 503

McWilliam A., Preston G. W., Sneden C., Searle L., 1995, AJ, 109, 2757

McWilliam A., Rich R. M., 1994, ApJS, 91, 749

McWilliam A., Smecker-Hane T. A., 2005, in Astronomical Society of the Pacific Conference Series, Vol. 336, Cosmic Abundances as Records of Stellar Evolution and Nucleosynthesis, Barnes III T. G., Bash F. N., eds., p. 221

McWilliam A., Wallerstein G., Mottini M., 2013, ApJ, 778, 149

Mighell K. J., Rich R. M., 1996, AJ, 111, 777

Minkowski R., 1941, PASP, 53, 224

Monaco L., Bellazzini M., Bonifacio P., Buzzoni A., Ferraro F. R., Marconi G., Sbordone L., Zaggia S., 2007, A&A, 464, 201

Monaco L., Bellazzini M., Ferraro F. R., Pancino E., 2003, ApJ, 597, L25

Monaco L., Bellazzini M., Ferraro F. R., Pancino E., 2005, MNRAS, 356, 1396

Neyskens P., van Eck S., Plez B., Goriely S., Siess L., Jorissen A., 2011, in Astronomical Society of the Pacific Conference Series, Vol. 445, Why Galaxies Care about AGB Stars II: Shining Examples and Common Inhabitants, Kerschbaum F., Lebzelter T., Wing R. F., eds., p. 77

Norris J. E. et al., 2013, ApJ, 762, 28

Philips A., 2004, The Physics of Stars. Wiley-Blackwell, Connecticut, USA

Popesso P., Biviano A., Böhringer H., Romaniello M., 2006, A&A, 445, 29

Popowski P. et al., 2005, ApJ, 631, 879

Recchi S., Calura F., Gibson B. K., Kroupa P., 2014, MNRAS, 437, 994

Reddy B. E., Lambert D. L., Allende Prieto C., 2006, MNRAS, 367, 1329

Ryde N. et al., 2010, A&A, 509, A20

Sarajedini A., Layden A. C., 1995, AJ, 109, 1086

Sbordone L., Bonifacio P., Buonanno R., Marconi G., Monaco L., Zaggia S., 2007, A&A, 465, 815

Searle L., Sargent W. L. W., 1972, ApJ, 173, 25

Siegel M. H. et al., 2007, ApJ, 667, L57

Smecker-Hane T., McWilliam A., 1999, in Astronomical Society of the Pacific Conference Series, Vol. 192, Spectrophotometric Dating of Stars and Galaxies, Hubeny I., Heap S., Cornett R., eds., p. 150

Smecker-Hane T. A., 1997, in American Institute of Physics Conference Series, Vol. 393, American Institute of Physics Conference Series, Holt S. S., Mundy L. G., eds., pp. 571–581

Smecker-Hane T. A., McWilliam A., 2002, unpublished, [arXiv:astro-ph/0205411]

Sneden C., 1973, ApJ, 184, 839

Tinsley B. M., 1979, ApJ, 229, 1046

Tolstoy E., Hill V., Tosi M., 2009, ARA&A, 47, 371

Tsujimoto T., Bekki K., 2012, ApJ, 747, 125

Vakarchuk I. O., Rykalyuk R. E., Yankiv-Vitkovska L. M., 1998, Journal of Physical Studies, 2, 16

Vanhollebeke E., Groenewegen M. A. T., Girardi L., 2009, A&A, 498, 95

Wallerstein G., 1962, ApJS, 6, 407

Wheeler J. C., Sneden C., Truran, Jr. J. W., 1989, ARA&A, 27, 279

White J. R., 2012, Master's thesis, The University of Manchester

Wood P. R., 2010, Mem. R. Astr. Soc., 81, 883

Woosley S. E., Weaver T. A., 1995, ApJS, 101, 181

Zhukovska S., Gail H.-P., Trieloff M., 2008, A&A, 479, 453

Zoccali M., Minniti D., 2009, in Revista Mexicana de Astronomia y Astrofisica, vol. 27, Vol. 35, Revista Mexicana de Astronomia y Astrofisica Conference Series, pp. 85–90

Zoccali M. et al., 2003, A&A, 399, 931